New constraints for paleogeographic reconstructions at ca. 1.88 Ga from geochronology and paleomagnetism of the Carajás dyke swarm (eastern Amazonia)

P.Y.J. Antonio, M.S. d'Agrella-Filho, Anne Nedelec, Marc Poujol, C. Sanchez, Et Al.

New constraints for paleogeographic reconstructions at *ca*. 1.88 Ga from geochronology and paleomagnetism of the Carajás dyke swarm (eastern Amazonia)

Antonio, P.Y.J.[1,2,], D'Agrella-Filho, M.S.[1], Nédélec, A.[2], Poujol, M.[3], Sanchez, C.[4], Dantas, E.L.[5], Dall'Agnol, R.[6,7], Teixeira, M. F. B.[8], Proietti, A.[9], Martínez Dopico, C.I.[10], Oliveira, D.C.[6], Silva, F.F.[6], Marangoanha, B.[6], Trindade, R.I.F.[1]*

1 Instituto de Astronomia, Geofísica e Ciências Atmosféricas (IAG), Universidade de São Paulo (USP), Rua do Matão, 1226, 05508-090, São Paulo, SP, Brazil (*: paulantonio0931@gmail.com)
2 Géosciences Environnement Toulouse (GET), Université de Toulouse, UPS, CNRS, IRD, CNES, 14 avenue E. Belin, 31400 Toulouse, France
3 Géosciences Rennes UMR CNRS 6118, Université Rennes 1, 35042 Rennes Cedex, France
4 GEOPS, Université Paris-Sud, CNRS, Université Paris-Saclay, Rue du Belvédère, Bât. 504, 91405Orsay, France.
5 Instituto de Geociências - Universidade de Brasília. ICC-Centro, Campus Universitário Darcy Ribeiro Asa Norte 70910-900, Brasilia, DF, Brazil
6 Instituto de Geociências (IG), Universidade Federal do Pará (UFPA). CEP-66075-900, Belém, Pará, Brazil
7 Instituto Tecnologico Vale, Belém, Pará, Brazil
8 Universidade Federal do Oeste do Pará, Santarém, Pará, Brazil
9 Centre de Microcaractérisation Raimond Castaing, 3 Rue Caroline Aigle, 31400 Toulouse – France
10 Institute of Geochronology and Isotope Geology (INGEIS, CONICET), University of Buenos Aires, Argentina

ABSTRACT

The Uatumã event is a silicic large igneous province (SLIP) covering an area of 1.500.000 km^2 of the Amazonia craton at *ca*. 1890 – 1850 Ma. New paleomagnetic data and U-Pb apatite ages for coeval microgranitic, andesitic, and basaltic dykes in the Carajás Province (southeastern Amazonia craton) are presented. Two primary characteristic remanent magnetizations (ChRMs) were isolated for the Carajás dykes which were combined with published results for coeval rocks in the São Felix do Xingu area, producing two grand mean poles: (1) "CA1", dated at 1880 Ma on zircon and apatite, whose mean site directions cluster around the mean D_m= 132.8°, I_m= 76° (N=26, α_{95}=5°, k= 32.7), yielding the paleomagnetic pole at 328.7°E, 23.3°S, (A_{95}= 8.7° K=11.7), and (2) "CA2" from well-dated microgranitic dykes of the Velho Guilherme Suite (1855 Ma U-Pb on zircon and apatite). Site mean directions group around the mean D_m= 240.3°, I_m= 11.8° (N= 18, α_{95}=10.8°, k= 11.1), which yielded the paleomagnetic pole at 221.3°E, 30.2°S, (A_{95}= 8.8°, K=16.2). The remanent magnetization of the Velho Guilherme microgranitic dykes is carried by pseudo-single

domain (PSD) magnetite. Its primary origin is supported by a positive baked contact test. Two younger secondary components were also isolated in the Carajás dyke swarm: one probably associated to the Mesozoic Central Atlantic magmatic province (CD3), and another component (CD4) with yet undefined age. A new configuration for the Amazonia and West Africa during the Paleoproterozoic, which aligns the Sassandra shear zone (in Africa) and the North Guiana Through and other shear zones (in Guiana Shield), is supported by geological and paleomagnetic data. The large angular distance between the 1880 Ma CA1 and 1855 Ma CA2 (Q~6) poles that are relatively close in age implies in a high plate velocity for the Amazonia craton, which is not consistent with modern plate tectonics. A similar large discrepancy between 1880 and 1860 Ma poles was also observed at least as many as six cratons. Although other hypotheses can be invoked, such as non-uniformitarian magnetic fields, the occurrence of large-scale true polar wander at this time may be the most parsimonious explanation of the widespread discrepancies.

KEYWORDS: Amazonia; West Africa; paleogeography; paleomagnetism; Uatumã, Carajás.

INTRODUCTION

Geodynamics during Proterozoic times in relation to the Earth's thermal evolution and convection remains a challenging task to elucidate (Ernst, 2017). After the probable onset for plate tectonics during the Archean at *ca.* 3200 Ma (Shirey and Richardson, 2011), the Paleoproterozoic eon is marked by a transitional period between the Archean stagnant-lid tectonics and the mobile-lid tectonics (Brown et al., 2020; Liu et al., 2019). In that sense, paleogeographic reconstructions are keystone to understand the Earth's geodynamics. The relative positions of cratons are mostly based mainly on correlations of geological records (orogenic sutures, dyke swarms, similarities between lithologies, *etc*.) and can only be properly constrained with the acquisition of high-quality paleomagnetic poles for each craton,

in order to precisely provide their apparent polar wander paths (APWPs) (Buchan, 2013). In addition, since the beginning of the Paleoproterozoic, Earth history was punctuated by quasi-periodic supercontinental cycles where larger landmasses or supercontinents were formed in specific time intervals (Condie, 1998, 2002; Condie and Aster, 2013; Murphy, 2013; Nance et al., 1988; Nance and Murphy, 2013; Nance et al., 2014; Worsley et al., 1984). A large consensus exists for the best-defined supercontinents: such as Pangea at *ca.* 350 – 200 Ma (Domeier et al., 2012; Stampfli et al., 2013) and Rodinia at *ca.* 1100 – 750 Ma (Li et al., 2013; Merdith et al., 2017). The first Proterozoic supercontinent in Earth's history (at *ca.* 1800 – 1600 Ma), hereafter called Columbia (a.k.a. Nuna) according to Meert (2012), is the subject of debates regarding its configuration during the Paleo-Mesoproterozoic times (D'Agrella-Filho et al., 2016; Evans and Mitchell, 2011; Evans, 2013; Evans et al., 2016; Johansson, 2009; Meert and Santosh, 2017; Pehrsson et al., 2016; Pisarevsky et al., 2014; Zhang et al., 2012). The main geological evidence for the existence of Columbia is the presence of 2100 to 1800 Ma orogeneses that have been described in most cratons, suggesting growth of large landmasses (Zhao et al., 2002; Zhao et al., 2004). This period of amalgamation was considered as a "turmoil" by Antonio et al. (2017), and preceded one interval between 1800 and 800 Ma, the so-called "boring billion", where no changes are observed in the atmosphere and ocean compositions (Roberts, 2013). It is widely accepted that Laurentia was not completely assembled at *ca*. ~1900 Ma , and large distances existed between its cratons (Slave, Rae, Hearne, Nain, Wyoming and Superior) (Kilian et al., 2016). Final suturing for Baltica resulted from the collision between Fennoscandia and the Volgo-Sarmatia block at *ca*. 1750 Ma, along the Svecofennian orogeny, which implies these cratonic blocks were separated at *ca*. 1880 Ma (Bogdanova et al., 2013; Bogdanova et al., 2016; Lubnina et al., 2016).

87 The present study addresses the reconstruction of the Amazonia craton during the
88 Paleoproterozoic, one of the major pieces of the Columbia jigsaw. The Amazonia craton is
89 considered to have been linked to West Africa at *ca*. 1960 Ma after the ~2000 Ma Trans-
90 Amazonian/Eburnean Orogeny (Bispo-Santos et al., 2014a; D'Agrella-Filho et al., 2016;
91 Nomade et al., 2003; Onstott and Hargraves, 1981; Onstott et al., 1984b; Théveniaut et al.,
92 2006). A geological link with Baltica was supported by paleomagnetic data including the
93 Amazonia craton in the core of Columbia connection at latest Paleoproterozoic, at *ca*. 1790
94 Ma (Bispo-Santos et al., 2014b). The Amazonia and West Africa cratons were also considered
95 as an isolated large landmasses drifting separated from Columbia (Pisarevsky et al., 2014).

96 Anomalous paleomagnetic data were reported for cratons during the Columbia
97 supercontinent assembly (2000 – 1800 Ma) which was interpreted as the consequence of
98 either rapid plate motions, absence of a stable dipolar field, tectonic problems, or true polar
99 wander (TPW) events (Hanson et al., 2004; Hanson et al., 2011; McGlynn and Irving, 1978;
100 Mitchell et al., 2010; Mitchell, 2014). A comprehensive compilation of available
101 paleomagnetic data at *ca*. 1890 – 1860 Ma supports the existence of a TPW event linked to
102 the reorganization of whole mantle convection (Antonio et al. (2017). This TPW event was
103 coeval with the widespread occurrence of large igneous provinces (LIPs) in most cratons
104 worldwide (Isley and Abbott, 1999). Emplacement of LIPs implies the existence of large
105 plumbing systems with layered intrusions, sills provinces and giant dyke swarms providing
106 possibilities to reconstruct older cratonic associations using the LIP records from different
107 cratons (Bleeker, 2003; Ernst et al., 2010; Ernst et al., 2013; Söderlund et al., 2016).

108 Preliminary paleomagnetic investigations in the Carajás Province was performed by
109 Renne et al. (1988) on nine specimens (2 sites in Figure 1). Here we present new
110 paleomagnetic and geochronological results for the Tucumã and Rio Maria dyke swarms in
111 Pará state, southern Amazonia craton. Compared with paleomagnetic data obtained on

112 associated volcanic rocks of the ~1890 – 1860 Ma Uatumã SLIP (silicic large igneous
113 province) by Antonio et al. (2017), these new key poles have large implications for
114 Precambrian geodynamics.

115 ## 1. GEOLOGICAL SETTING AND LITHOLOGY

116 ### 1.1. The Uatumã SLIP

117 The Amazonia craton is one of the largest cratons of the world with ~4.400.000 km^2
118 (Almeida et al., 1981). It consists of the Guiana Shield in the north and the Central-Brazil (or
119 Guaporé) Shield in the south, separated by the Amazon sedimentary basin (Santos et al.,
120 2000; Schobbenhaus et al., 1984) (Figure 1-A). In the Guiana Shield, two major Archean
121 nuclei have been recognized, the Imataca Block in northern part and the Amapá Block in the
122 eastern part (Rosa-Costa et al., 2006; Tassinari et al., 2004). In the Central-Brazil Shield, the
123 Archean portion is composed of the Carajás Province and the Bacajá Block (Vasquez et al.,
124 2008). Except for the Carajás Province, these Archean nuclei were reworked during the
125 Transamazonian/Eburnean orogeny, which main area of influence is largely coincident with
126 the geochronological Maroni-Itacaiunas Province (2260 – 1950 Ma) (Cordani and Teixeira,
127 2007). The Carajás Province is the oldest crustal portion of the stable Archean-
128 Paleoproterozoic core of the Amazonia craton, the Central Amazonian Province (Tassinari
129 and Macambira, 2004; Teixeira et al., 2019b). During the Paleoproterozoic times,
130 accretionary belts occurred along the southwestern margin of this cratonized landmass with
131 the development among others of the Ventuari – Tapajós Province (2000 – 1800 Ma)
132 (Bettencourt et al., 2016; Valério et al., 2018).

133 The Carajás Province comprises the Carajás (north) and Rio Maria (south) tectonic
134 domains, and is delimited to the east by the Araguaia Belt (~550 Ma) (Figure 1-B) (Santos,
135 2003; Silva et al., 1974; Vasquez et al., 2008). These domains were intruded by the ~1900-
136 1850 Ma rocks of the Uatumã event (Amaral, 1974), which form a silicic large igneous

137 province (SLIP) (Figure 1-A-B) (Dall'Agnol et al., 2005; Dall'Agnol and Oliveira, 2007;
138 Giovanardi et al., 2019; Rivalenti et al., 1998; Silva Jr et al., 1999; Teixeira et al., 2018;
139 Teixeira et al., 2019b). This SLIP is considered as one of the largest continental magmatic
140 event of the Earth's history (>1.500.000 km^2) (Ernst, 2014). In the studied area, it is
141 composed of Paleoproterozoic anorogenic granites (Jamon, Serra dos Carajás and Velho
142 Guilherme suites and similar related granites) with associated dykes in the Rio Maria and
143 Tucumã areas, and by felsic to intermediate volcanic and plutonic rocks (São Felix do Xingu
144 area) (Figure 1), which were dated between 1890 and 1860 Ma (Antonio et al., 2017; Teixeira
145 et al., 2019b). These Paleoproterozoic units are well-preserved without deformation and no
146 younger orogenic event is recorded into the Carajás Province.

147 The origin of the Uatumã SLIP involves mafic underplating and the emplacement of giant
148 dyke swarms associated with crustal extension (Dall'Agnol et al., 1994; Giovanardi et al.,
149 2019; Silva et al., 2016). Thermal perturbations in association with a plume activity were also
150 related to a true polar wander event induced by geoidal perturbations (Antonio et al., 2017).
151 An alternative origin of this magmatism considers that the south-western side of the Central
152 Amazonian Province was affected by a flat-subduction period followed by a slab break-off in
153 an arc-related environment (Cassini et al., 2020; Fernandes et al., 2011; Juliani and
154 Fernandes, 2010; Roverato et al., 2019).

155 **FIGURE 1**

156 ### 1.2. Carajás dyke swarm

157 In this study, we sampled mafic and felsic dykes (Carajás dyke swarm) crosscutting the
158 Archean basement of the Carajás Province, to the east of the coeval volcanic units (São Felix
159 do Xingu, SFX) previously studied by Antonio et al. (2017) (Figure 1-B). Two areas with
160 dyke intrusions in the Rio Maria domain were the targets of this paleomagnetic study, the
161 Tucumã (Figure 2-A) and the Rio Maria (Figure 2-B) areas. Near to Tucumã city, the NW-

trending dyke swarm is located to the west of the ~1860 Ma A-type Velho Guilherme granite and intrudes the Archean Rio Maria granodiorite dated at 2872 ± 5 Ma by U-Pb on zircon (Pimentel and Machado, 1994) and the Tucumã greenstone belt dated at 2868 ± 8 Ma by Pb-Pb evaporation on zircon (Avelar et al., 1999) (Figure 2-A). Near to Rio Maria city, the dykes are associated to the ~1880 Ma Jamon suite and intrude a complex Mesoarchean juvenile crust composed by sequences of greenstone belts, TTG series and sanukitoid- rocks (3000 – 2860 Ma) (Figure 2-B). The Jamon suite and related granites are well-dated by U-Pb (TIMS) on zircons with ages between 1880 and 1857 Ma (Teixeira et al., 2018), and their magmas derived essentially by crustal anatexis of Archean protoliths (Teixeira et al., 2019a). According to the U-Pb ages of felsic and mafic dykes, three generations of dykes are recognized in the Carajás Province: (1) The *ca.* 1880 Ma Carajás dykes (*i.e.*, the Uatumã SLIP), (2) the *ca.* 535 Ma Parauapebas dykes, and (3) the Mesozoic dykes associated to the Central Atlantic Magmatic Province (CAMP) (Antonio et al., 2017; Silva et al., 2016; Teixeira et al., 2019b).

FIGURE 2

1.2.1. The 1880 Ma Carajás dykes

The *ca.* 1880 Ma Carajás dykes include (i) NW- trending microgranitic (or rhyolitic) dykes which likely represent the subvolcanic equivalent of the A-type granites in the Carajás Province, (ii) NW- trending andesitic dykes, and (iii) NW- and NE-trending basaltic dykes.

The NW- trending **microgranitic dykes** are subvertical, *ca.* 15 m in width and a few hundred meters in length in average (Figure 3-A). They are made of A-type subsolvus microgranite characterized by subhedral phenocrysts of quartz, alkali feldspar and plagioclase in a quartz-feldspar matrix with granophyric texture. The most frequently observed primary accessory minerals are zircon, titanite and magnetite. In the Tucumã are, two of these microgranitic dykes were dated by SHRIMP U-Pb on zircon, which revealed ages of 1882 ± 4

187 Ma and 1881 ± 3 Ma (Silva et al., 2016). Pb-Pb evaporation ages for these microgranitic
188 dykes in the Rio Maria area indicate an emplacement between 1890 and 1870 Ma (Oliveira,
189 2006; Rodrigues et al., 2015). U-Pb ages of 1895 ± 11 Ma and 1854 ± 6 Ma for microgranitic
190 dykes in the western part (São Felix do Xingu area) of the Carajás Province show that this
191 NW-trending dyke swarm extends for ~300 km in length between Rio Maria and São Felix do
192 Xingu (Antonio et al., 2017).

193 The NW- trending **andesitic dykes** are observed mainly in the Rio Maria area (Figure
194 3-B) and rarely in the northern Carajás and Tucumã areas (Rivalenti et al., 1998). They have a
195 porphyritic texture with plagioclase phenocrysts. Groundmass is constituted by quartz,
196 plagioclase, altered clinopyroxene, and Fe-Ti oxides. Andesitic dykes have a high-K calc-
197 alkaline character (Rivalenti et al., 1998). A Rb-Sr isochron for andesites defines a poorly
198 constrained age of 1874 ± 110 Ma (Rivalenti et al., 1998), which suggests that these andesitic
199 dykes could be coeval with the ~1880 Ma microgranitic dykes.

200 The NW- and NE- trending **basaltic dykes** are tholeiitic in composition with ophitic
201 texture (Figure 3-C). A baddeleyite U-Pb age of 1880 ± 1.5 Ma was recently published for a
202 NW- basaltic dyke from the Rio Maria area (Teixeira et al., 2019b). Another baddeleyite U-
203 Pb age of 1884.6 ± 1.6 Ma obtained for a NE- trending dyke supports the idea that these
204 basaltic dyke are coeval with the microgranitic and andesitic dykes (Teixeira et al., 2019b).
205 The occurrence of composite NW-trending basaltic and microgranitic dykes and showing
206 basaltic enclave in the microgranitic dyke and dropped K-feldspar megacrysts in the basaltic
207 rocks (site 34) are substantial field evidences to indicate a coeval emplacement of these dykes
208 (Figure 3-E). Similar features were also observed in site 15 (Figure 2-B) near the northeastern
209 border of the Musa pluton cutting the Rio Maria granodiorite (Dall'Agnol et al., 2006).

210 **1.2.2. Younger generations of dykes in Carajás**

211 Two younger events of basaltic dykes were recognized in the Carajás Province. Near to
212 Parauapebas (Figure 1-B), a new baddeleyite U-Pb age of 531 ± 1 Ma for a NS- trending
213 basaltic dyke demonstrate the existence of Neoproterozoic dykes in the region (Teixeira et al.,
214 2012b; Teixeira et al., 2019b). These Parauapebas dykes may represent a post-collisional
215 extension at the southeastern margin of the craton in response to the Neoproterozoic Araguaia
216 Belt (Teixeira et al., 2019b). A baddeleyite U-Pb age of 199± 0.3 Ma for a basaltic dyke in
217 northern Carajás indicates the presence of Mesozoic dykes in the region (Teixeira et al.,
218 2012a; Teixeira et al., 2019b). These dykes can be related to the ~200 Ma Central Atlantic
219 Magmatic Province (CAMP) in Brazil (De Min et al., 2003). Mesozoic dykes are also
220 observed in Tucumã where a gabbroic dyke crosscuts the microgranite and basaltic dykes of
221 the Uatumã SLIP (Figure 3-D).

222 **FIGURE 3**

223 ## 2. SAMPLING AND LABORATORY PROCEDURES

224 ### 2.1. Sampling

225 The Paleoproterozoic dyke swarm of the Uatumã SLIP was sampled for a
226 paleomagnetic study in the Tucumã and Rio Maria areas (GPS location in Supplementary data
227 1). In the Tucumã area we sampled 28 sites thus distributed: (i) 16 NW- trending
228 microgranitic dykes from the well-dated ~1880 Ma swarm (sites 33, 34, 36, 37, 39, 40, 41, 43,
229 45, 46, 47, 48, 51, 52, 53 and 54), (ii) 7 NW- trending basaltic dykes with evidence for
230 mingling with the microgranitic dykes (sites 35, 38, 40, 42, 44, 49 and 50), (iii) 2 sites for one
231 NS- trending gabbroic dyke which is considered to be Mesozoic in age (sites 38 and 41) given
232 its freshness and crosscutting relations, and (iv) 3 sites of Archean basement for a baked
233 contact test, and to test regional consistency (sites 36, 38 and 46) (Figure 2-A;). In the Rio
234 Maria area we sampled 25 sites thus distributed: (i) 2 NW- trending microgranitic dykes dated
235 at ~1880 Ma (sites 12 and 22) and a felsic part of a composite dyke (site 15), (ii) 5 NW-

236 trending andesitic dykes of ~1880 Ma (sites 17, 18, 20, 21 and 24), (iii) 8 NW- trending
237 basaltic dykes, one of which (site 19) is well-dated (U-Pb on baddeleyite) at ~1880 Ma (sites
238 13, 19, 15, 16, 23, 25, 27 and 31), (iv) 6 NE- trending basaltic dykes that we assume to be
239 Mesozoic in age (sites 14, 26, 28, 29, 30 and 32), and (v) 4 sites of Archean basement rocks
240 for a baked contact test (Sites 14, 16, 17 and 22) (Figure 2-B). A total of 304 cylindrical cores
241 (~2.54 cm in diameter) and 15 oriented block samples were collected in both areas and
242 oriented with a magnetic compass, and in most cases, also using a solar compass.

243 As rocks are often poorly exposed in these areas, most dykes were sampled on isolated
244 blocks, without certainty of their *in-situ* position (Figure 3). However, consistent
245 paleomagnetic results were obtained intra and inter-sites (see below), which confirm that the
246 sampled blocks suffered very small movements. Furthermore, it was difficult to observe the
247 direct lithological contacts in these challenging outcrops (weathering, mature soils).
248 Nevertheless, in the Tucumã area we attempted a contact test between the Mesozoic gabbroic
249 dyke and a NW- microgranitic dyke (Figure 9-A). In the Rio Maria area, direct contacts with
250 the country rock are not visible, and dykes generally crop out as isolated blocks, so that, no
251 adequate baked contact test could be realized. Whenever possible, however, we collected 'in
252 situ' Archean rocks trying to isolate the magnetic direction carried by the country rocks. We
253 sampled Archean rocks close to a NW- microgranitic dyke (site 22), close to a NW- andesitic
254 dyke (site 17), close to a NW- basaltic dyke (site 16) and close to a NE- basaltic dyke (site
255 14). We sampled also the basaltic-felsic composite dyke dated at ~1880 Ma (Oliveira, 2006)
256 (site 15). Trying to best support the paleomagnetic data, selected rocks were prepared for U-
257 Pb analysis on apatite and zircon grains.

258

259 **2.2. Geochronology**

The sample preparation for the apatite and zircon separation was performed in the Geosciences Environnement Toulouse laboratory (GET, Toulouse, France). The freshest part of the rock cylinders as well as hand samples were crushed and sieved to collect the mineral fraction below 400 µm. The ultra-fine sized mineral fractions (as the clay) and the low-density minerals were removed with a Wilfley table. Heavy minerals were then isolated using heavy liquids (tetrabromoethane and diiodomethane, with respective densities of 2.967 and 3.325). Magnetic minerals were consequently removed with a Franz magnetic separator. Then, the apatite and zircon grains were handpicked with a binocular microscope before being mounted in epoxy puck and polished (see Figure 4-F).

Five samples were analyzed by U-Pb geochronology on apatite (PY36, PY44-46, PY71, PY72 and PY73 see location Figure 2-A and GPS in supplementary data 1). The U/Pb apatite geochronology was conducted at the GeOHeLiS analytical platform (Géosciences Rennes laboratory, France). Nine to thirty-nine minerals were analyzed depending on the sample, by in-situ laser ablation inductively coupled plasma-mass spectrometry (LA-ICP-MS) using a ESI NWR193UC Excimer laser coupled to a quadripole Agilent 7700x ICP-MS equipped with a dual pumping to enhance sensitivity (Paquette et al., 2014). For more instrumental setting details see Pochon et al. (2016) and supplementary data 2. During ablation, 50 µm-wide ablation spots were performed. The data obtained were corrected for mass bias and U-Pb fractionation by standard bracketing with repeated measurements of the Madagascar apatite standard (Thomson et al., 2012), while the Durango (31.44 ± 0.18 Ma; (McDowell et al., 2005)) and McClure (523.51 ± 2.09 Ma; (Schoene and Bowring, 2006)) apatite standards were analyzed in the same conditions to control the precision and accuracy of the analyses. Data reduction was carried out with the Iolite software (Paton et al., 2011) and the data reduction scheme VizualAge_UcomPbine (Chew et al., 2014). During the analyses, the McClure and Durango apatite standards yielded ^{207}Pb corrected ages of 526.0 ± 6.6 Ma

285 (MSWD = 1.06; probability = 0.39) and 32.3 ± 0.56 Ma (MSWD = 0.38; probability = 0.997)
286 respectively, see Supplementary data 2.

287 In two samples (PY44-46 and PY73), some zircons were handpicked. These samples
288 were selected for U-Pb geochronology on zircon. These analyses were carried out by LA-SF-
289 ICP-MS at the Isotopic Geology Laboratory of the Geosciences Institute – UNICAMP
290 (Brazil). Isotope data were acquired using a Thermo Element-XR mass spectrometer coupled
291 to an Excite 193 laser ablation system (Photon Machines). The acquisition protocol includes a
292 spot size of 25 µm with a 10 Hz laser frequency and a 40s ablation time according the
293 procedures of Navarro et al. (2015). The reference material 91500 zircon was used as primary
294 standard (Wiedenbeck et al., 1995), and data reduction was performed using Iolite software
295 (Paton et al., 2011). During the course of analyses, the Peixe zircon (age ID-TIMS of 564 ± 4
296 Ma; (Dickinson and Gehrels, 2003)) was used as a secondary reference mineral and gives an
297 age of 568.6 ± 3.6 Ma (MSWD= 1.4) during our analyses (see supplementary data 3).

298 **2.3. Paleomagnetism**

299 Preparation and analysis of samples were performed in the Paleomagnetic Laboratory
300 of the Instituto de Astronomia e Geofisica of the University of São Paulo (USPMag, Brazil),
301 where cylindrical cores and blocks were prepared in 2.2 cm high standards specimens (1223
302 in total). In order to isolate a characteristic remanent magnetization (ChRM), conventional
303 stepwise Alternating Field (AF) and thermal demagnetization were performed in a
304 magnetically shielded room with ambient field <1000 nT. A pre-treatment with low
305 temperature demagnetization (LTD- 5 N_2 baths) was applied on selected specimens to reduce
306 the multidomain (MD) influence before AF and thermal procedures (Borradaile, 1994;
307 Borradaile et al., 2004; Dunlop and Argyle, 1991; Warnock et al., 2000). AF demagnetization
308 was done using a tumbler Molspin AF demagnetizer with steps of 2.5 mT (up to 15 mT) and 5
309 mT (15-100 mT) and a JR-6A spinner magnetometer (AGICO, Czech Republic) was used to

measure the remanence. We also used an automated three-axis AF demagnetizer coupled to a horizontal 2G-Enterprises™ DC-SQUID magnetometer, and an AF demagnetization coils coupled to a vertical 2G-Enterprises™ DC-SQUID magnetometer with an automatic sample changer (Kirschvink et al., 2008). Stepwise thermal demagnetization of 50°C (until 500°C) and 20°C (until 700°C) were carried out using a TD-48 furnace device. Principal component analysis (PCA) (Kirschvink, 1980) or intersecting great circle technique (Halls, 1978) was used to determine the remanence directions using orthogonal vectors diagrams (Zijderveld, 1967) and/or stereographic projections. Only vectors with mean angular deviation (MAD) smaller than 8° was considered. Mean remanence directions and paleomagnetic poles were calculated using Fisher (1953) statistics. Paleomagnetic data processing and calculations was carried out using PALEOMAC package (Cogné, 2003). GPlates were used for paleogeographic reconstructions (Boyden et al., 2011). In addition, magnetic mineralogy of each site was investigated to determine the carriers of magnetic remanence. Hysteresis loops, isothermal remanent magnetization (IRM) and first order reverse curves (FORC) for selected samples were performed to determine magnetic carriers and domain states, using a MicroMag-VSM, Model 3900 (Princeton Measurements Corporation). Thermomagnetic experiments (susceptibility versus temperature) were conducted in an argon atmosphere in low- and high-temperature conditions using a CS-4 apparatus coupled to the KLY-4S Kappabridge instrument (AGICO, Brno, Czech. Republic). Thin and polished sections were analyzed under transmitted and reflected light microscopy. In addition, Scanning Electron Microscopy (SEM) analysis using a Jeol JSM-6360LV instrument (Géosciences Environnement Toulouse, France) was used to constrain the nature and textures associated with the magnetic carriers.

3. U/PB GEOCHRONOLOGICAL RESULTS

3.1. Apatite dating

All the apatite isotopic ratios data are reported in Table 1 and are plotted in Tera-Wasserburg diagrams (Figure 4) realized using Isoplot/Ex (Ludwig, 2009). All errors are listed at 2 sigmas. For the calculation of the ^{207}Pb corrected ages (Table 1), the initial common ^{207}Pb/^{206}Pb value of 0.990 was calculated following the terrestrial Pb evolution model of Stacey and Kramers (1975).

The isotopic data obtained for the PY73 sample (microgranitic dyke) display variable proportions of common Pb with ^{207}Pb/^{206}Pb values varying between 0.17 and 0.35. The unforced lower intercept date for this sample is 2007 ± 140 Ma with a MSWD of 1.09. If the Discordia is forced to a ^{207}Pb/^{206}Pb value of 0.990 (Figure 4-A), the resulting lower intercept date is 1885 ± 30 Ma (MSWD = 1.4). The weighted average ^{207}Pb-corrected date is equivalent to the intercept age with a date of 1861 ± 28 Ma (MSWD = 0.28) (see Figure 4-A).

Data obtained for samples PY36 and PY4446 (andesitic dykes) display variable proportions of common Pb (^{207}Pb/^{206}Pb values between 0.52-0.70 and 0.33-0.62, respectively). The data for the PY36 sample define an unforced lower intercept date of 1861 ± 140 with a MSWD of 0.48. If the Discordia is forced to a ^{207}Pb/^{206}Pb value of 0.990 (Figure 4-B), the resulting lower intercept date is equivalent within error at 1853 ± 44 Ma. For sample PY44-46, the unforced lower intercept date is 1873 ± 41 with a MSWD of 1.00. If the Discordia is forced to a ^{207}Pb/^{206}Pb value of 0.990 (Figure 4-C), the resulting lower intercept date is equivalent within error at 1868 ± 18 Ma. The weighted average ^{207}Pb-corrected dates are equivalents, within the error, to 1874 ± 64 Ma (MSWD = 0.05, PY36) and 1882 ± 20 Ma (MSWD = 0.52, PY44-46) (see Figures 4-B and 4-C).

Data obtained for the samples PY71 and PY72 (basaltic dykes) display variable proportions of common Pb as indicated by their ^{207}Pb/^{206}Pb values between 0.31-0.46 and 0.17-0.41, respectively. For sample PY71, the data yield an unforced lower intercept date of 1949 ± 190 (MSWD = 1.06) within error similar to the date of 1898 ± 39 Ma (MSWD= 0.97)

obtained when the $^{207}Pb/^{206}Pb$ value is forced to 0.990 (Figure 4-D). For sample PY72, the lower unforced intercept yields a date of 1885 ± 48 Ma (MSWD = 0.69). If the Discordia is forced to a $^{207}Pb/^{206}Pb$ value of 0.990, we obtain a similar date of 1890 ± 34 Ma (MSWD = 0.62). The weighted average ^{207}Pb-corrected dates are equivalents, within the error, for both samples at 1912 ± 55 Ma (MSWD = 0.53, PY71) and 1895 ± 40 Ma (MSWD = 0.52, PY72) (see Figure 4-D and 4-E).

FIGURE 4

TABLE 1

3.2. Zircon dating

For the microgranitic dyke PY73, 6 zircon spots yield a Concordia age of 1903 ± 13 Ma (2σ, MSWD = 0.28) (Table 2; Figure 5-A). The weighted mean age $^{207}Pb/^{206}Pb$ of 1909 ± 8.5 (MSWD = 2) is equivalent within error limits. The andesitic dyke PY44-46 show a Concordia age of 1909 ± 19 Ma (MSWD = 1.14) (Table 2; Figure 5-B). This age is equivalent within error limits to an upper intercept age of 1911 ± 21 Ma (MSWD = 0.24) and a weighted mean age $^{207}Pb/^{206}Pb$ of 1927 ± 42 Ma (MSWD = 4.9).

FIGURE 5

TABLE 2

4. PALEOMAGNETIC RESULTS

4.1. Magnetic components

Paleomagnetic results of the Tucumã and Rio Maria dyke swarms record a complex history where primary component is partially or wholly overprinted by secondary natural remanent magnetizations (NRMs). To resolve and isolate the magnetic components AF treatment was generally more efficient than thermal demagnetization which reveal for some samples a characteristic “tail”, typical feature of multidomain (MD) grains (Dunlop and

384 Özdemir, 2000; Shcherbakova et al., 2000) (Figure 6-A). After removal of randomly oriented
385 secondary components, most of sites reveal a stable characteristic remanent magnetization
386 (ChRM) with a steep inclination for these Carajás Dykes (CD1 component). Samples of the
387 ~1880 Ma andesitic (PY36C2, Figure 6-A) and basaltic (PY72A1, Figure 6-B) dykes show a
388 north/northeastern, steep upward inclination direction with unblocking temperature ranging
389 between 300 and 580°C and high coercivities (> 25mT). Occurrence of reverse polarity
390 appears in the ~1880 Ma microgranitic dykes (Figure 6-C, E) and some basaltic dykes (Figure
391 6-D). No stable components with unblocking temperatures higher than 600°C were found in
392 these samples, even in those from microgranitic dykes.

393 A second southwestern (northeastern), low inclination direction (component CD2) was
394 revealed in some microgranitic dykes and even in the granodioritic host rocks (~2870 Ma)
395 cropping out in the studied area. This component was observed in the microgranitic dyke of
396 the Velho Guilherme suite (~1855 Ma) after LTD treatment (~60% of remanence was
397 removed) followed by thermal demagnetization, and associated with unblocking temperatures
398 between 400°C and 600°C (Figure 6-F).

399 A third northern, low upward inclination component (CD3) was isolated for younger
400 basaltic dykes, after removing secondary directions with coercivities lower than 12 mT
401 (Figure 6-G). One of these NS gabbroic dykes cuts Paleoproterozoic dykes and a baked
402 contact test was performed for it (see below). Similar directions were also observed on nine
403 Paleoproterozoic dykes and Archean basement rocks as secondary components.

404 A fourth component (CD4) is characterized by northern, low downward inclination
405 directions (Figure 6-H) and was found in 11 collected basaltic dykes. On fresh basaltic dykes
406 this component is carried by magnetite with high unblocking temperatures (520-580°C)
407 suggesting a primary character for it. Some ~1880 Ma microgranitic dykes showed also the
408 same component and should represent a younger remagnetization.

409 **FIGURE 6**

410 **4.2. Site mean directions and paleomagnetic poles**

411 Normal (6 dykes) and reverse (10 dykes) polarities were found for the CD1 component.
412 This stable component was isolated for microgranitic, andesitic and basaltic dykes well-dated
413 at ~1880 Ma in this study. A mean direction was calculated for the CD1 component using
414 both normal and reverse site mean directions: Dm= 125.9°, Im= 73.8° (α_{95}=5.9°, k= 40.4),
415 and the respective CD1 paleomagnetic pole is located at 334.3°E, 23°S (A_{95}= 9.8° K=15.2)
416 (Table 3; Figure 7-A). CD1 component is similar to the SF1 component calculated for the
417 volcanic rocks of the ~1880 Ma Santa Rosa Formation, located ~300 km to the west of
418 Tucumã, and interpreted as a primary magnetization acquired during rock intrusion (Antonio
419 et al., 2017). The SF1 component obtained in the rhyolitic rocks of São Felix do Xingu is
420 carried by hematite with high unblocking temperatures (620°C-700°C) (Antonio et al., 2017).
421 The SF1 and CD1 components exhibited both polarities.

422 In view of the similarity in the directions of both SF1 and CD1 components (Figure 7-B),
423 we can use this dataset to calculate a grand mean pole for the Uatumã SLIP, *i.e.*, a mean pole
424 calculated from multiple distinct but broadly coeval cooling units of a large igneous province
425 (*e.g.*, the Umkondo LIP; (Swanson-Hysell et al., 2015)). The grand mean direction (named
426 CA1 - Carajás component) was calculated for the Carajás magmatic event: Dm= 132.8°, Im=
427 76° (N=26, α_{95}=5°, k= 32.7). The respective CA1 paleomagnetic pole is located at 328.7°E,
428 23.3°S (A_{95}= 8.7° K=11.7) (Table 4; Figure 7-B). Nine among the twenty-six sites of the CA1
429 pole were precisely dated by U-Pb method (zircon and baddeleyite) (Antonio et al., 2017;
430 Oliveira, 2006; Pinho et al., 2006; Silva et al., 2016; Teixeira et al., 2019b), Pb-Pb
431 evaporation on zircon (Oliveira, 2006; Pinho et al., 2006) and U-Pb on apatite at 1880 Ma
432 (Table 2; Figure 4). CA1 grand mean pole pass the reversal test (McFadden and McElhinny,

1990). The critical gamma of 10.6° is greater than the angle between the normal and reversed axes (1.9°), and the test is classified as "C". So, it can be considered as positive using the 26 sites.

The CD2 component observed in 6 sites in the Tucumã-Rio Maria area is composed of magnetic directions with both polarities. The CD2 site mean directions cluster around the mean: Dm= 239.3°, Im= 19.6° (N=6, α_{95}=21.4°, k= 10.7) and the CD2 paleomagnetic pole is located at 227°E, 30.4°S (A_{95}= 18.4° K=14.6) (Table 3; Figure 7-C). This CD2 component is also carried by three sites of the Archean rocks sampled far from each other, and not close to the contact of any dyke. This could imply a regional remagnetization. However, the CD2 component is similar to the SF2 component of the São Felix do Xingu volcanic rocks, for which a positive baked contact test attests to the primary nature of the SF2 magnetization acquired at ~1855 Ma (Antonio et al., 2017). Therefore, a combined mean including both CD2 and SF2 site mean directions was calculated and named as the CA2 component: Dm= 240.3°, Im= 11.8° (N= 18, α_{95}=10.8°, k= 11.1), with a corresponding paleomagnetic pole located at 221.3°E, 30.2°S (A_{95}= 8.8° K=16.2) (Table 4; Figure 7-D). The means of reverse and normal polarity site mean directions form a similar cluster with k1=k2 at 99% of confidence according to McElhinny (1964) and similar directions with a difference of 10.0° in declination (Table 4), but the reversal test is undetermined (McFadden and McElhinny, 1990).

The CD3 component was firstly calculated only for the basaltic dykes where field evidence suggests they are Mesozoic (at baked contact tests or cross-cutting older dykes). For these dykes, the site mean directions group around Dm= 357.3°, Im= -25.7° (N=8, α_{95}=11.9°, k= 22.7), which yielded the paleomagnetic pole located at 352.6°E, 82.3°S (A_{95}= 9.5° K=35) (Table 3; Figure 8-A). Only one polarity was found on these dykes. The CD3 component was also disclosed for some ~1880 Ma microgranitic dykes and even for host rocks close to these basaltic dykes suggesting a regional remagnetization during this magmatic event (Figure 8-B).

458 These site mean directions cluster around the mean Dm= 351.4°, Im= -24.6° (N=9, α_{95}=17.7°,
459 k= 9.0). This mean direction is close to the CD3 component calculated for the Mesozoic
460 dykes (see above).

461 The CD4 component is characterized by remanent magnetizations northerly directed and
462 with low downward inclinations. Their site mean directions group around Dm= 352.7°, Im=
463 33.3° (N=11, α_{95}=10.7°, k= 19) and the CD4 paleomagnetic pole is located at 113.7°E, 63.4°S
464 (A_{95}= 10.8° K=18.7) (Table 3; Figure 8-C). This magnetic component was disclosed for
465 basaltic dykes, whose magnetic carriers are characterized by high unblocking temperatures,
466 suggesting a primary origin, but it was also found on ~1880 Ma microgranitic dykes.
467 Unfortunately, no radiometric age on these basaltic dykes is presently available to determine
468 the age of the CD4 component.

469 **FIGURE 8**

470 **TABLE 3**

471 **TABLE 4**

472 ## 5. BAKED CONTACT TEST

473 Figure 9-A is a schematic sketch showing a younger NS gabbroic dyke cross-cutting a
474 NW microgranitic dyke in the Tucumã area. Despite the difficulty to find blocks in situ, it was
475 possible to perform a reverse baked contact test between a small ramification of this younger
476 NS gabbroic dyke and the ~1880 Ma microgranitic dyke where the contact was visible.
477 According to the mean direction, the gabbroic dyke (PY62) is associated to the Jurassic
478 CAMP event (Dm= 357.7°, Im= -19.3°, α_{95}=3.7°) (Table 3; Figure 9-B). At contact (<10 cm),
479 the microgranitic samples show a similar direction (Dm= 20.4°, Im= -5°, α_{95}=12.2°) (Table
480 3). In contrast, samples collected far away from the contact (>3 m) show a different direction

(Dm= 111.8°, Im= 60.3°, α_{95}=4.6°) (Table 3; Figure 9-B). This reverse contact test confirms that these microgranitic samples near to the contact were baked during the intrusion of the dyke at ~200 Ma. The different remanent magnetization direction, with unblocking temperatures greater than 450°C, isolated for samples far away of the dyke contact indicates that this direction is older than 200 Ma. No hybrid direction was found in the collected samples (Figure 9-B).

FORC experiments were conducted on samples of the gabbroic dyke and for samples of the microgranitic dyke at the contact and far away it (Figure 9-C). The FORC diagram for a sample from the younger Mesozoic dyke (PY62A1) shows that magnetic mineralogy is controlled by a mixture of MD and mainly PSD magnetite (Roberts et al., 2014). For a sample of the microgranite at the contact (PY62G1, 3 cm), the FORC diagram shows only the PSD magnetite behavior like the younger Mesozoic dyke. This behavior contrasts with that of sample PY62Q1 at 8 m away of the contact where SD behavior prevails, that is, higher coercivities are dominant. This suggests that the younger Mesozoic dyke affected the magnetic mineralogy close to the contact remagnetizing the rock. Modification of the magnetic mineralogy in the host rock according the distance at contact during the dyke's intrusion was already documented (Hyodo and Dunlop, 1993). These results also suggest that FORC diagrams can be a powerful tool to detect magnetic changes within a baked contact test.

FIGURE 9

6. MAGNETIC MINERALOGY

6.1. Petrography

The iron oxides were examined using a Scanning Electron Microscope (SEM) to explore their primary character. Accessory minerals in microgranitic and andesitic dykes are zircon,

505 magnetite and titanite (*cf.* also (Dall'Agnol et al., 1997)). Magnetite (Fe_3O_4) is the primary
506 main iron oxide and is present in all studied rocks. For example, iron oxide inclusion within
507 an albite crystal is observed in sample PY65, suggesting a primary origin (Figure 10-A). The
508 EDS spectrum shows that the mineral is iron oxide (without Ti), which may be magnetite or
509 hematite, since we cannot see the difference between Fe^{2+} and Fe^{3+} using SEM technique
510 (Figure 10-A). Although, magnetite grains exhibit a very small size (~5-10 μm), it was
511 possible to detect the primary character of octahedral magnetite within a quartz phenocryst
512 (Figure 10-B). The EDS spectrum confirmed that this mineral is an iron oxide (Figure 10-B).
513 Hematite (αFe_2O_3) crystallized after a process of alteration and is responsible for the
514 characteristic red color of the rocks (Boone, 1969; Nédélec and Bouchez, 2015; Nédélec et
515 al., 2015). The presence of hematite is difficult to be directly observed with the microscope
516 because the grains are very small. Ilmenite ($FeTiO_3$) in association with titanium oxide (TiO_2)
517 and a large magnetite grain with exsolution of ilmenite were observed in an andesitic dyke
518 (PY32 - Fig. 10-C). Magnetite grains showing exsolution of ilmenite are also present in the
519 basaltic dykes in association with primary minerals as apatite or baddeleyite, and different
520 types of sulfides (sphalerite, pyrrhotite) (Figure 10-D).

521 **FIGURE 10**

522 **6.2. Day's plot and hysteresis curves**

523 Magnetic mineralogy study of most of dykes indicates that magnetization is carried by
524 PSD magnetite (or more precisely in a vortex state (Roberts et al., 2017)) according to the
525 Day's diagram (Figure 11-A). For microgranite dykes, PSD magnetite is formed during the
526 magmatic stage, so it is primary. Hematite is formed by hydrothermal alteration of the
527 magnetite in subsolidus condition. Presence of hematite in these dykes is confirmed by
528 hysteresis curves showing a wasp-waisted behavior and IRM curves, which do not reach
529 saturation at fields up to 3 T (Figure 11-B). We can observe dominance of the magnetic

contribution in hematite for some microgranite dykes using the Kruiver's analysis (Kruiver et al., 2001) with ~65% of the hematite component versus 35% of the magnetite component (rich-hem) (Figure 11-B). Magnetic mineralogy for most of microgranitic and andesitic dykes, however, is dominated by presence of magnetite rather than hematite (Figure 11-C). Magnetic mineralogy for the NW-basaltic dykes shows that magnetization is carried by PSD magnetite (Figure 11-D). The NS-gabbroic dyke of CAMP has also PSD magnetite as can be seen in the Day's plot (Figure 11-A) and in the FORC diagram (Fig. 9-C). The *ca.* 2872 Ma Rio Maria granodiorite is the main basement rock in the Tucumã region (Avelar et al., 1999), and magnetic mineralogy shows large magnetite grains associated with recrystallization (Santos and Oliveira, 2016). According to the Day's plot, samples of granodiorite are mainly multi-domain grains (MD) with Hcr/Hc ratios greater than 5 (see supplementary data 4 for Day plot values). So, it is very suspicious that these Archean rocks could retain a primary magnetization.

FIGURE 11

6.3. Thermal susceptibility

The thermomagnetic curve for a microgranite dyke (PY59A) shows the presence of a well-pronounced Hopkinson peak, Curie temperature around 580°C, and the Verwey transition at low temperatures, which are characteristics of SD/PSD magnetite (Dunlop and Özdemir, 1997) as the main magnetic carrier in this rock (Figure 12-A). Rich-hematite sample in the Day's diagram shows a curve with irreversible behavior characterized by different trajectories during heating and cooling and small fall around 600° C indicating the presence of magnetite in small quantity (Figure 12-B). The presence of hematite, well-characterized in the previous topics, is not visible on the thermomagnetic curves, which is normal due of its low magnetic susceptibility, compared to that of magnetite. Also, during heating, a new magnetically strong mineral (probably magnetite) is being formed, possibly by alteration of

555 other Fe-rich minerals. The NW basaltic dyke (PY71) does not show the Verwey transition
556 but a fall at *ca.* 580°C indicates the presence of magnetite (Figure 12-C). The Jurassic dyke
557 PY60L shows a reversible behavior with a well-pronounced Hopkinson peak, Curie
558 temperature at about 580°C, as well as the Verwey transition at low temperatures, which are
559 characteristics of SD/PSD magnetite (Figure 12-D).

560 **FIGURE 12**

561 ## 7. DISCUSSION

562 ### 7.1. Reliability of paleomagnetic poles

563 #### 7.1.1. CA1 paleomagnetic pole

564 The CA1 grand mean pole was calculated using 26 sites having ChRM directions with
565 steep upward and downward inclinations. Among these 26 sites, 16 sites are basaltic,
566 andesitic and microgranitic dykes of the Carajás Province (this study) and 10 sites are from
567 the coeval volcanic rocks of the São Felix do Xingu area (Antonio et al., 2017). CA1
568 component is carried by stable hematite in the rhyolitic rocks of São Felix do Xingu area and
569 PSD magnetite in basaltic dykes of Tucumã and Rio Maria areas. The CA1 pole (328.7°E,
570 23.3°S, A_{95}= 8.7°) satisfies 6 (Q=6) out of the 6 quality criteria proposed by Van der Voo
571 (1990), if we discard his seventh criterion as suggested in the Paleomagia database for
572 Precambrian rocks (Pivarunas et al., 2018; Veikkolainen et al., 2017b): (1) the four U-Pb
573 dating on apatite and one U-Pb age on zircon from andesitic and basaltic dykes (this study)
574 yielded consistent ages around 1880 Ma, and paleomagnetic analysis on the same dykes
575 revealed similar ChRM directions. These ages are concordant with two U-Pb baddeleyite ages
576 (1880±2 Ma, 1885±2 Ma) determined on two other basaltic dykes in the Rio Maria area
577 (Teixeira et al., 2019b), and two zircon U-Pb ages (1882±4 Ma, 1881±3 Ma) obtained for two
578 microgranitic dykes (Silva et al., 2016). The weighted average age of ten well-dated
579 paleomagnetic sites used in the CA1 grand mean pole (see Figure 7-B) is 1881.4 ± 2.5 Ma

580 (MSWD = 3.9), which constrain the age of the CA1 component. The multi-method
581 radiometric dating (U-Pb baddeleyite, zircon and apatite) show that the magnetic age is
582 clearly close to the crystallization age of these rocks. Also, the blocking temperatures (300 –
583 500°C) associated with the apatite isotopic system demonstrate that no later high thermal (>
584 300°C) perturbation occurred in the CA1 dykes. (2) The CA1 pole was calculated with 26
585 sites and 248 specimens and show good Fisher's statistical parameters (A_{95} = 8.7°, K = 11.7)
586 (Table 4). (3) Remanence vectors were well-isolated using stepwise AF treatments, and
587 thermal demagnetizations. They were calculated by the principal component analysis
588 (Kirschvink, 1980) through the visualization of magnetic directions plotted in the Zijderveld
589 diagrams and stereographic projections. (4) A positive inverse baked contact test obtained for
590 a Jurassic dyke cutting a 1880 Ma microgranitic dyke in the Tucumã area (Figure 9), shows
591 that the CA1 remanent magnetization is older than ~199 Ma. Another positive inverse baked
592 contact obtained in São Felix do Xingu for a ~1855 Ma microgranitic dyke cutting the
593 andesitic rock from the 1880 Ma Sobreiro Formation demonstrates that CA1 component is
594 older than 1855 Ma, and most probably it was acquired at the time rock was formed at 1880
595 Ma (Antonio et al., 2017). (5) The fact that the same paleomagnetic results were disclosed for
596 volcanic rocks of the São Felix do Xingu area and the Carajás dyke swarm in Tucumã and Rio
597 Maria areas, some 300 km apart implies that no tilting affected these rocks after their
598 emplacement, at least between the studied areas. Moreover, these two areas must belong to
599 the same geological province and a separation into different geological domains as proposed
600 by Vasquez et al. (2008) is no longer sustainable. (6) The CA1 component pass a reversal test,
601 which implies the secular variation was averaged out. (7) Even if we discard this criterion, the
602 CA1 pole is different from poles calculated for younger units in the Amazonia craton
603 according to the compiled Precambrian Paleomagnetic database for Amazonia by D'Agrella-
604 Filho et al. (2016) (see also Antonio et al. (2017). The southeastern part of the Amazonia

craton, was cut by the ~535 Ma mafic dykes coeval to the Araguaia Belt and the ~200 Ma Central Atlantic Magmatic Province (CAMP) (Teixeira et al., 2019b). No paleomagnetic study is presently available for the ~535 Ma dykes but the CA1 direction is different from the Puga B pole (Q= 2), whose age is estimated to be ~520 Ma (Trindade et al., 2003) and from the CAMP paleomagnetic poles (Moreira, 2019). So, the 1880 Ma CA1 paleomagnetic pole can be considered as a key pole.

7.1.2. **CA2 paleomagnetic pole**

Only 3 out of the 18 sites used to calculate the CA2 grand mean pole are from this work. This component is better represented at the São Felix do Xingu (15 sites) than at Tucumã or Rio Maria areas. The three sites of Archean host rocks that have the same magnetization are not considered in the CA2 grand mean pole calculation. These sites suggest that an important geological regional event affected these rocks imprinting this component in these Archean rocks. We suggest that it is represented by the last pulse of the Uatumã magmatic event (the Velho Guilherme Suite intrusions) occurred at ~1855 Ma as indicated by a positive baked contact test made for a microgranitic dyke from the Velho Guilherme Suite (dated at 1855 Ma) cutting the andesitic rock from the 1880 Ma Sobreiro Formation in the São Felix do Xingu area (Antonio et al., 2017). As for the CA1 component described above, the grand mean pole CA2 satisfies also 6 of the first 6 quality criteria of Van der Voo (1990): (1) The Velho Guilherme dykes are well-dated at 1853.7±6.2 Ma by LA-ICP-MS U-Pb zircon (Antonio et al., 2017), and 1857±8 Ma by SHRIMP U-Pb zircon (Roverato, 2016) which well-constrain the age of CA2 component. One age of 1903 ± 13 Ma by U-Pb zircon and one age of 1885 ± 30 by U-Pb apatite were obtained in this study for one microgranitic dyke. The U-Pb apatite age could be considered more reliable for the magnetic age, within error similar to the ~1860 Ma age of the Velho Guilherme suite (2) The CA2 paleomagnetic pole was calculated using 18 sites and 132 specimens and have good statistical parameters (A_{95}=8.8°,

630 K=16.2). (3) As for component CA1, stepwise AF and thermal demagnetizations were used to
631 separate components, which were calculated by the principal component analysis (Kirschvink,
632 1980). (4) No baked contact test in the Rio Maria and Tucumã areas was performed but a
633 positive baked contact test was described in the São Felix do Xingu area for a 1855 Ma
634 microgranitic dyke of the Velho Guilherme suite at the contact with the Sobreiro Formation
635 (Antonio et al., 2017). (5) No deformation or metamorphism was observed in microgranitic
636 and basaltic dykes. Unless some dyke intrusions at *ca.* 535 Ma, related to the marginal
637 Brasiliano Araguaia belt development, and at *ca.* 200 Ma, related to the CAMP event, the
638 Carajás Domain maintained its tectonic integrity since 1850 Ma. Although the 2870 Ma host
639 rocks revealed also the same component, this is interpreted to be due to a regional
640 remagnetization during the last pulse of the Uatumã event at ~1855 Ma. With an extension
641 >1.500.000 km^2, the Uatumã SLIP and its thermal footprint have the potential to induce a
642 regional remagnetization. (6) Two polarities were observed, which implies that secular
643 variation was average out. (7) Although the seventh criterion of Van der Voo (1990) may be
644 disregarded for Precambrian rocks (see above), it is obeyed by this component, since it
645 doesn't have any similarity with younger paleomagnetic data available for the Amazonia
646 craton. So, the CA2 grand mean pole can be considered as key (Q= 6) with an age of ~1855
647 Ma.

648 7.1.3. **CD3 and CD4 paleomagnetic poles**

649 Other two components (CD3 and CD4) were isolated in the investigated rocks. The
650 CD3 single normal polarity component was disclosed for 8 well-known Jurassic dykes dated
651 at 199.3±0.3 Ma (Moreira, 2019; Nomade et al., 2000). A positive baked contact test for one
652 of these dykes supports a primary magnetization for it (Figure 9). The CD3 pole (Q= 5)
653 calculated for the CAMP dykes in Carajás is located at 82.3°S, 325.6°E (A_{95}= 9.5°, K= 35).
654 Although more scattered, the CD3 secondary directions disclosed for the older rocks (Figure

655 8-B) yielded a paleomagnetic pole (79.8°S, 359.4°E; A_{95}= 14.6°, K= 13.3) very similar to the
656 CAMP CD3 pole. These poles statistically agree with another pole determined for the CAMP
657 dolerite dykes, in French Guana, and dated at 198 Ma (Figure 13; (Nomade et al., 2000)). It is
658 also similar to a recent paleomagnetic pole obtained for the ~201 Ma Penatecaua sills (76.5°S,
659 279.5°E, A_{95}= 3.8°) sampled *ca.* 700 km far from Carajás (Moreira, 2019).

660 The CD4 paleomagnetic pole was calculated for 11 basaltic and microgranitic dykes in
661 Carajás and is located at 63.4°S, 113.7°E (A_{95}= 10.8°, K= 18.7). No age is presently available
662 for these dykes, or field tests to constrain the age of the CD4 pole. We suggest it represents a
663 younger regional remagnetization for the following reasons: (1) this component is observed
664 on five 1880 Ma microgranitic dykes – the primary component of the 1880 Ma magmatic
665 event is probably represented by pole CA1 as discussed above; (2) this component looks like
666 the SF3 component (40.7°S, 128.8°E, A_{95}= 15.6°) observed in the ~1880 Ma volcanic rocks
667 in SFX (Antonio, 2017). This component is carried by large magnetite in coarse-grained
668 microgranite, and goethite in rhyolite as secondary component (Tb <200°C) (Antonio et al.
669 (2017). (3) The CD4 pole is close to the Neoproterozoic/Cambrian Amazonian paleomagnetic
670 poles (see Figure 13): the Planalto da Serra Alkaline Complex (49.7°S, 133.4°E, A95= 10.8°)
671 (Garcia et al., 2013) whose age is established by several Ar-Ar ages on phlogopite at *ca.* 610
672 Ma (D'Agrella Filho et al., 2018; De Min et al., 2013) and the secondary Puga B pole
673 (33.6°S, 146.9°E, A95= 8.4°) (Trindade et al., 2003) for which the authors attributed an age
674 of ~520 Ma.

675 **FIGURE 12**

676 **7.2. Geological model and Paleoproterozoic APW path for Amazonia and West**
677 **Africa**

678 Geological data suggest a connection between Amazonia (Am) and West Africa (WA)
679 cratons after the "Transamazonian/Eburnean" collisional events at *ca.* 2100–2000 Ma (Caen-
680 Vachette, 1988; Ledru et al., 1994; Vanderhaeghe et al., 1998). First paleomagnetic data for
681 West Africa and Amazonia highlighted the reassessment of the Pangea fit which would not be
682 valid before the Neoproterozoic (Onstott and Hargraves, 1981). These reconstructions
683 suggested a rotation of about 30° of the Amazonia in relation to West Africa to align the Guri
684 (Am) and Sassandra (WA) shear zones (Caen-Vachette, 1988; Cohen and Gibbs, 1989;
685 Feybesse and Milési, 1994; Ledru et al., 1994). More recently, new paleomagnetic data seem
686 to support these reconstructions (Figure 14-A, option A) (Bispo-Santos et al., 2014a; Nomade
687 et al., 2003). However, a recent revision of structures and kinematics of the Transamazonian-
688 Eburnean orogen by Chardon et al. (2020) allow to re-align the Eburnean strain pattern in
689 West Africa with large Transamazonian shear corridors in the Guiana Shield, which avoids
690 inconsistencies in structural patterns in previous models (Bispo-Santos et al., 2014a;
691 Grenholm, 2019; Nomade et al., 2003). In this new model (Figure 14-B, option B), the
692 Sassandra shear zone is no longer connected to the Guri shear zone, but with the North
693 Guiana Through (Ledru et al., 1991). These West African and Amazonian shear zones, named
694 as the Burghana-Transamazonian mega shear zone by Chardon et al. (2020), are connected to
695 the Pisco-Juruá shear zone which is the most rectilinear corridor in Guiana Shield (Chardon et
696 al., 2020).

697 Here, we re-evaluate the paleomagnetic data and APW paths for Amazonia and West
698 Africa according to these models (Table 5; Figure 14). According to Klein and Moura (2008),
699 the São Luis craton in Brazil was part of the West African craton during the Paleoproterozoic
700 and it was not considered by Bispo-Santos et al. (2014a) in their reconstruction. Based on the
701 new structural pattern for the Transamazonian-Eburnean orogen proposed by Chardon et al.
702 (2020), the new alternative model (Option B) is compatible with the available paleomagnetic

703 data between ~2100–1960 Ma (Figure 14-B). Obviously, the option A cannot be rejected on
704 paleomagnetic grounds due to the quality of the APW paths. Note that using the new
705 configuration (Figure 14-B), the ~1790 Ma Avanavero pole for Amazonia (Bispo-Santos et
706 al., 2014b) overlaps the ~1740 Ma PGV obtained for the Iguarda dykes of West Africa (Neres
707 et al., 2016) which can give a suggestive support for option B. It should be noted that this
708 result could also be a coincidence because the age match is ~50 Ma different. Excursion of the
709 APW path at *ca*. 1860 Ma and return to broadly the same place at *ca*. 1820 Ma is consistent
710 with a TPW oscillation (Creveling et al., 2012).This new configuration seems to support the
711 viability of a long-lived paleomagnetic connection between these two units.

712 The option A configuration is close to the hypothesized position of Amazonia and
713 West Africa in the (South-America-Baltica) SAMBA connection (Johansson, 2009). If option
714 B indeed proves more viable, then the SAMBA connection of these two cratons relative to
715 Baltica needs to be revised in the paleogeographic models.

716 **FIGURE 14**

717 **TABLE 5**

718 **7.3. Geophysical anomalies: Weak dipolar field or True Polar Wander event?**

719 According to our results, two paleomagnetic poles are considered as primary for the
720 Amazonia craton: the CA1 pole dated at 1880 Ma and the CA2 pole dated at 1860 Ma. These
721 almost coeval, but very discordant paleomagnetic poles (Figure 14), supposedly of primary
722 origins, would imply in a great drift for proto-Amazonian craton which is unrealistic for the
723 current plate tectonics. So, some alternative interpretations are discussed here that could
724 explain such inconsistence:

725 (1) *Possibility of local vertical-rotation axis due to shear zones and deformation along*
726 *orogens can provide discordant coeval paleomagnetic poles.* For the Slave craton, Mitchell et

al. (2010) suggested that the oscillations in almost coeval paleomagnetic poles (1960–1870 Ma) that define the Coronation APWP loop can be explained by true polar wander (TPW) events. Recently, however, Gong et al., (2018) revised the inconsistent paleomagnetic data obtained for the Pearson Formation (~1870 Ma) for small blocks in the Great Slave Basin, and suggested that it can be explained by a rotation of *ca.* 60° along local vertical-rotation axis in the area, originating by fault displacements (Gong et al., 2018). These authors suggest that some other broadly coeval paleomagnetic poles in the Great Slave Supergroup could have been also affected by local rotations, *e.g.*, the aberrant poles of the Stark and Tochatwi Formations (Bingham and Evans, 1976; Evans and Bingham, 1976), although no geological evidence is yet available to confirm this hypothesis. Concerning the Carajás area in this study, CA1 (1880 Ma) and CA2 (1860 Ma) ChRM directions were obtained both, for volcanic rocks from the São Felix do Xingu area and from dykes in the Rio Maria and Tucumã areas, distant up to 300 km apart. Therefore, most probably, no deformation or shear zones affected these rocks after the 1880 Ma and 1860 Ma rock intrusions. Also, as already stressed, the volcanic rocks of São Felix do Xingu is part of the Carajás Province and not a different domain as suggested by Santos (2003).

(2) *Regional remagnetization can disturb the paleomagnetic record to give discordant poles.* For Baltica, similar 1900–1750 Ma paleomagnetic poles fall into the Permian segment of the Phanerozoic APWP traced for this cratonic block, which could explain why they are tightly clustered (Bazhenov et al., 2016). It should be stressed, however, that there is a highest probability for Paleoproterozoic poles to coincide with a younger APW path for a same continent and the argument of coincidence with younger poles to justify a remagnetization is not conclusive (Pivarunas et al., 2018). In the case of the Carajás area, as stressed above, the CA1 and CA2 poles do not coincide with other younger poles from the Amazonia craton, and

751 the positive baked contact test performed for the CA1 component prove that both CA1 and
752 CA2 components are of primary origins.

753 (3) *Another explanation for discordant paleomagnetic poles could be the presence of a Weak*
754 *dipolar field during Proterozoic* (Biggin et al., 2009; Biggin et al., 2015). Recently, values
755 ranging between 1.22 to 2.15 10^{22} Am^2 was proposed for the intensity of the geomagnetic
756 field at ~1860 Ma based on paleointensity studies on rocks from Baltica (Veselovskiy et al.,
757 2019). These low values seem continue until ~1790 Ma with low paleointensity data obtained
758 for the ~1790 Ma Avanavero sills in Amazonia (Di Chiara et al., 2017) or for the ~1790 Ma
759 Hoting gabbro in Baltica (Donadini et al., 2011). These data seem to support a weak dipolar
760 field at least for sometimes in the interval ~1900–1700 Ma, which could be at the origin of
761 these paleomagnetic discrepancies. So, test the validity of the Geocentric Axial Dipole (GAD)
762 is important before using paleomagnetic data for paleogeographic reconstructions
763 (Veikkolainen et al., 2017a). Analysis of a global compilation of paleointensity data showed
764 the Precambrian field seems to be dominated by an axial dipole component associated to an
765 octupolar component (Veikkolainen et al., 2017a). Global compilations for Precambrian
766 reversal tests, including our paleomagnetic reversal test at ~1880 Ma, also agree with a
767 dominant dipolar component for the geomagnetic field during Proterozoic (Veikkolainen et
768 al., 2014). Thus, these results exclude the low Paleoproterozoic geomagnetic field as the
769 reason for the CA1 and CA2 poles discrepancy.

770 (4) *If discordant paleomagnetic poles are primary, another explanation is to suppose the*
771 *motion of the entire solid earth (mantle+crust) in respect to the spin axis of the Earth, the true*
772 *polar wander (TPW) hypothesis* (Raub et al., 2007). The two TPW events, before and after *ca.*
773 1860 Ma comprising the full oscillation is close to ~90° in amplitude (Figure 14), *i.e.*, inertial
774 interchange true polar wander (IITPW) (Goldreich and Toomre, 1969; Kirschvink et al., 1997;
775 Rose and Buffett, 2017). The 1900-1800 Ma time interval is associated with worldwide Large

776 Igneous Provinces (LIPs) emplaced in all cratons, and paleomagnetic studies were carried out
777 for many of these LIPs. A compilation of the almost coeval, but discordant paleomagnetic
778 poles was performed by Antonio et al. (2017). Some geological and paleomagnetic
779 associations of this model is well-established like the connection between India and Australia
780 (Liu et al., 2018; Stark et al., 2019). Despite the small amount and quality of paleomagnetic
781 data, Antonio et al. (2017) conclude that the hypothesis of a True Polar Wander event at
782 ~1880-1850 Ma is the best explanation for these discordant paleomagnetic poles.

783 **CONCLUSION**

784 The first U-Pb apatite ages for andesitic, basaltic, and microgranitic dykes were obtained for
785 the Carajás Province (Amazonia craton). These new U-Pb apatite ages of ~1890–1850 Ma
786 agree from previous zircon and baddeleyite ages for the Carajás dyke swarm which belong to
787 the Uatumã event (Antonio et al., 2017; Teixeira et al., 2019b). Two key paleopoles, CA1
788 (~1880 Ma; 23.3°S, 328.7°E, A_{95}= 8.7°) and CA2 (~1855 Ma; 30.2°S, 221.3°E, A_{95}= 8.8°),
789 were calculated for the Carajás volcanic rocks and dyke swarms. They are proven to be
790 primary by a positive baked contact test for a ~1855 Ma granodioritic dyke (component CA2)
791 in contact with the andesitic rock (CA1 component) from the 1880 Ma Sobreiro Formation,
792 reinforced by the U-Pb multi-method radiometric dating (zircon, baddeleyite, apatite) which
793 indicates that no high thermal events (> 300 °C) affected the rocks after their intrusion. Two
794 younger paleomagnetic poles (CD3 and CD4) were also obtained: a *ca.* 200 Ma pole (CD3
795 pole) for Jurassic dykes from Carajás is located at 82.3°S, 325.6°E (A_{95}= 9.5°); the CD4 pole
796 (63.4°S, 113.7°E, A_{95}= 10.8°) was obtained for some of the dykes and basement rocks whose
797 age is yet undefined. A revision of the Paleoproterozoic APW paths for Amazonia and West
798 Africa supports a new geological configuration between these two cratons (Chardon et al.,
799 2020) which allows to restore the Sassandra shear zone in West Africa with the North Guiana
800 Through and other shear zones in Guiana Shield. The discrepancy in the ~1890-1850 Ma

Paleomagnetic poles observed in several cratons in the world could be better explained by a true polar wander event. However, new good-quality paleomagnetic data is necessary to resolve this issue.

ACKNOWLEDGEMENTS

We thank the Prof. W. Teixeira, the careful contribution of R. Mitchell, and one anonymous reviewer for constructive comments on the manuscript. We thank the Universidade Federal do Pará (UFPA) for the field trip logistical support and FAPESP (grants 2012/20335-4, 2013/22957-5, 2016/13689-5, 2017/18840-6) for financial support. RD acknowledge support from Conselho Nacional de Desenvolvimento Científico e Tecnológico (CNPq; Proc. 306108/2014-3 and 304648/2019-1) and the Instituto Nacional de Ciência e Tecnologia de Geociências da Amazônia/Geociam (CNPq-FAPESPA-CAPES-PETROBRAS, Proc. 573733/2008-2).

FIGURE CAPTIONS

Figure 1: **A:** Inset of the ~1880 – 1860 Ma volcano-plutonic Uatumã SLIP (silicic large igneous province) and the main tectonic provinces of the Amazonia craton (adapted from Cordani and Teixeira (2007)). *Abbreviations*: Archean blocks are represented in grey: *CP* = Carajás Province, BD = Bacajá domain, IB = Imataca Block, AM = Amapá Block; CA = Central Amazonian Province MI = Maroni-Itacaiunas Province; VT = Ventuari-Tapájos Province; RNJ = Rio Negro-Juruena Province; RO = Rondonian-San Ignácio Province; SS = Sunsás province,. **B:** The 1.88 Ga Uatumã SLIP in the Carajás Province. The geological maps of the Tucumã and Rio Maria areas represented in Figure 2 are indicated. These areas belong to the Rio Maria tectonic domain (southern) which is separated of the Carajás tectonic domain by the dashed line. Localization of paleomagnetic sites of this study, sites published in

825 Antonio et al. (2017) (SFX area), and sites of Renne et al. (1988) are indicated. U-Pb and Pb-
826 Pb dating for dykes are referred to Teixeira et al. (2019b).

827 **Figure 2:** Geological maps of Tucumã (**2-A**) and Rio Maria (**2-B**) areas with localization of
828 sampling sites, modified from Vasquez et al. (2008). See Figure 1 for areas localities in the
829 Carajás Province and supplementary data 1 for the GPS coordinates of dykes. Selected sites
830 for U-Pb geochronology in this study are indicated with a surrounding frame.

831 **Figure 3:** Outcrops photos of the Carajás dyke swarm. **A:** 1880 Ma microgranitic dyke, ~6 m
832 in width (Site 54), intruding the Archean greenstone belt (in green). **B:** Cross-sectional view
833 for a ~1880 Ma andesitic dyke (Site 24). White line is the boundary of the dyke and people
834 give the scale, ~25 m in width. **C:** ~1880 Ma NW- trending basaltic dyke with typical isolated
835 blocks, ~5 m in width (Site PY49). **D:** Field relationship where a NS- Mesozoic dyke
836 crosscuts NW- trending microgranitic and basaltic dykes. Archean granodiorite Rio Maria is
837 visible (Site 38). **E:** Field evidences of mingling (mafic enclave in microgranitic dyke) and
838 xenocrysts (K-feldspar in basaltic dyke) (Site 34).

839 **Figure 4:** Tera-Wasserburg Concordia diagram of apatite analyses with the corresponding
840 ^{207}Pb corrected age for one microgranitic dyke (**A**), two andesitic dykes (**B-C**), two basaltic
841 dykes (**D-E**) from the Carajás dyke swarm. **F**: Photomicrograph of apatite crystals in
842 binocular microscopy. $^{207}Pb/^{206}Pb$ value of 0.990 was calculated following the Pb evolution
843 model of Stacey and Kramers (1975).

844 **Figure 5:** U-Pb concordia diagram of zircon analyses from the PY73 microgranitic dyke (**A**)
845 and from the PY44-46 andesitic dyke (**B**).

846 **Figure 6:** Examples of AF (alternating field) and thermal demagnetization for Andesitic (**A-**
847 **B**), basaltic (**C-D**) and microgranitic (**E-F**) dykes from the Carajás dyke swarm. **G** and **H** are
848 examples for younger dykes in the area. Demagnetization results are presented with

849 stereographic projections, orthogonal projections (Zijderveld plot) and normalized
850 magnetization intensity curves.

851 **Figure 7:** Stereographic projections of site mean directions (and their confidence circles, α_{95})
852 for the Carajás Province. **A**: Site mean directions for the CD1 component of Carajás Dykes,
853 and **B**: the Grand mean sites CA1 calculated with the combined results of the volcanic units
854 from the São Felix do Xingu area (Antonio et al., 2017). **C:** represents the site mean
855 directions for the CD2 component for the Carajás dykes, and **D:** the Grand mean pole CA2
856 calculated combined with the volcanic units. Red star in each stereogram represents the mean
857 (and its confidence circle, α_{95}) of the site mean directions. PDF – Present Dipolar Field; PGF
858 – Present Geomagnetic Field.

859 **Figure 8:** **A**: Stereographic projections of site mean directions for the primary Mesozoic
860 dykes (~199 Ma). **B**: Site mean direction for the Archean/Paleoproterozoic sites re-
861 magnetized during this Jurassic event. **C:** Site mean directions for the CD4 component
862 (undetermined age). Blue (or red) star in each stereogram represents the mean (and its
863 confidence circle, α_{95}) of the site mean directions. PDF – Present Dipolar Field; PGF –
864 Present Geomagnetic Field.

865 **Figure 9:** Inverse baked contact test (i-BCT), showing in **A**: a Schematic sketch of a
866 microgranitic dyke intersected by a NS Mesozoic gabbroic dyke, in **B**: FORC diagrams for
867 samples of the Mesozoic dyke and for the microgranitic dyke at contact and far away from the
868 contact, and in **C**: Stereographic projections, orthogonal projections, and normalized
869 magnetization intensity curves for a sample of the Mesozoic dyke, and samples close to
870 contact and far away.

871 **Figure 10:** Petrography of paleomagnetic samples. **A**: SEM-BSE micrograph of plagioclase
872 for a microgranitic dyke (PY65) showing inclusion of primary Fe-Ti oxides and EDS spectra

associated. **B**: SEM-BSE micrograph of primary magnetite in inclusion in a quartz crystal for a microgranitic dyke (PY79) with EDS spectra associated. **C**: SEM-BSE micrographs for an andesitic dyke and **D** for a basaltic dyke. *Mineral abbreviations*: Ab (albite), Ap (apatite), Bdy (baddeleyite), Cpx (clinopyroxene), Ep (epidote), Ilm (ilmenite), Mag (magnetite), Pl (plagioclase), Qtz (quartz), Sp (spharelite), Ttn (titanite), Zrn (zircon), from Whitney and Evans (2010).

Figure 11: **A**: Day plot (Day et al., 1977) of the hysteresis ratios Mrs/Ms and Hcr/Hc for samples analyzed in this study. **B**: Hysteresis curve for a hematite-rich microgranite with IRM decomposition (PY70B). **C**: Hysteresis curve for a magnetite-rich microgranitic sample (PY59F). The strong magnetite component is well-observed in the IRM decomposition. D: Hysteresis curve of a typical sample of a basaltic dyke (PY30B) where the magnetic carrier falls in the Pseudo Single Domain of the Day's diagram (magnetite).

Figure 12: **A**: Example of thermomagnetic curves for a microgranitic dyke with a strong component of magnetite (PY59A). **B**: Example of thermomagnetic curve for a microgranitic dyke where hematite is dominant in magnetic mineralogy (PY61B). **C**: Thermomagnetic curve for a NW basaltic dyke dated at ~1880 Ma in this study. **D**: Typical thermomagnetic curve for the Mesozoic dykes.

Figure 13: **A**: Comparison of the primary CD3 and re-magnetized paleopoles (this study) with reference paleomagnetic poles obtained for rocks from the ~200 Ma Central Atlantic Magmatic Province (CAMP) - Amazonia (Nomade et al., 2000). Comparison of the CD4 paleopole with previous Neoproterozoic data (~610–520 Ma) (Garcia et al., 2013; Trindade et al., 2003).

Figure 14: **A**: Option A for the Amazonia-West Africa connection, using a geological connection between the Guri (Amazonia, AM) and Sassandra (West Africa, WA) shear zones

(Bispo-Santos et al., 2014a; Nomade et al., 2003). The apparent polar wander paths (APWPs) for Amazonia and West Africa between ~2100 and 1960 Ma and between ~1960 and 1790 Ma are illustrated for option A in the two orthographic projections. SL is the São Luis craton associated to West Africa. Euler pole for option A (fixed West Africa): lat: 61.09°; long: -19.63°; angle: 57.5°. **B:** Option B for the Amazonia-West Africa connection, connecting the North Guiana Trough with the Sassandra shear zone as suggested by Chardon et al. (2020). The apparent polar wander paths (APWPs) for Amazonia and West Africa between ~2100 and 1960 Ma and between ~1960 and 1790 Ma are illustrated for option B in the two orthographic projections. Euler pole for option B (fixed West Africa): lat: 33.98°; long: -28.42°; angle: 73.96°. TPW at ~1880–1850 Ma is indicated in red by discordance between CA1 and CA2. Paleomagnetic poles used are listed in Table 5.

TABLE CAPTIONS

Table 1: Apatite U–Pb data obtained by in situ laser ablation ICP-MS.

Table 2: Zircon U-Pb data obtained by LA-ICP-MS.

Table 3: Results of paleomagnetic data. n/N – number of analyzed samples/number of samples used in the mean; Dec (°) – declination; Inc (°) – inclination; α_{95}, r is the resultant vector, k – Fisher's confidence cone and precision parameter (Fisher, 1953); *G.C* –Great circles analysis. VGP – Virtual Geomagnetic Pole; P. Long – Paleolongitude; P. Lat – Paleolatitude. Values in bold are for the mean directions (N, Dec, Inc, R, K and A_{95} – P. Lat, P. Long). *: Sites discarded with higher α_{95} or not in situ (PY25-26).

Table 4: Grand mean poles calculated in this study. Combined paleomagnetic pole CA1 using the Carajás dykes (CD1) and associated volcanic rocks of São Felix do Xingu area (SF1) (Antonio et al., 2017). Combined paleomagnetic pole CA2 using the Carajás dykes (CD2) and associated volcanic rocks of São Felix do Xingu area (SF2) (Antonio et al., 2017). N –

number of sites (single geographic locality), Dec (°) – declination; Inc (°) – inclination; α_{95}, k – Fisher's confidence cone and precision parameter (Fisher, 1953). Paleomagnetic pole; P. Long – Paleolongitude; P. Lat – Paleolatitude, R is the resultant vector, K is precision parameter, S is the angular dispersion, and A95 is radius of the circle of 95% confidence of the paleomagnetic pole.

Table 5: Paleomagnetic poles compilation for West Africa and Amazonia and West Africa used in Figure 14. Nominal age is the magnetic age associated to the paleomagnetic pole. Confidence column indicate the geochronological method (strat: stratigraphic correlation, Pb-Pb method, APWP: correlation using APW path, Rb-Sr isochron, U-z: U-Pb zircon, U-b: U-Pb baddeleyite, U-a: U-Pb apatite, A-h: Ar-Ar amphibole, A-bi: Ar-Ar biotite) and possible field test (i-BCT: inverse baked contact test, BCT: baked contact test). *References*: (1) (Nomade et al., 2003), (2) (Piper and Lomax, 1973), (3) (Sabaté and Lomax, 1975), (4) (Peucat et al., 2005), (5) (Onstott et al., 1984b), (6) (Onstott and Dorbor, 1987), (7) (Neres et al., 2016), (8) (D'Agrella-Filho et al., 2011), (9) (Nomade et al., 2001), (10) (Théveniaut et al., 2006), (11) (Bispo-Santos et al., 2014a), (12) (Onstott et al., 1984a), (13) (Bispo-Santos et al., 2014b).

SUPPLEMENTARY DATA

Supplementary data 1: Paleomagnetic sampling for the Carajás dyke swarm, Carajás Province; *: Site sampled for the baked contact test (BCT) - distances from the contact are indicated.

Supplementary data 2: Values for U-Pb standards in apatite and analytical protocol (Geosciences Rennes, France).

Supplementary data 3: Results for the secondary material of reference (Peixe zircon) used in the University of Campinas (Brazil).

Supplementary data 4: Values for Mrs/Ms and Hcr/Hc ratio using in the Day plot diagram.

REFERENCES

Almeida, F.F.M., Hasui, Y., Neves, B.B.D., Fuck, R.A., 1981. Brazilian Structural Provinces: An Introduction. Earth-Science Reviews 17, 1-29.

Amaral, G., 1974. Geologia Pré-Cambriana da região amazônica. Universidade de São Paulo.

Antonio, P.Y.J., 2017. Paleomagnetism and petrogenesis of Paleoproterozoic units from the Uatumã event in the northern Amazonian Craton, Tese de Doutorado, Instituto de Astronomia, Geofísica e Ciências Atmosféricas (IAG) and Geosciences et Environnement Toulouse (GET). Universidade de São Paulo and Universite Toulouse 3 Paul Sabatier (UT3 Paul Sabatier), São Paulo and Toulouse, p. 320.

Antonio, P.Y.J., D'Agrella-Filho, M.S., Trindade, R.I.F., Nédélec, A., de Oliveira, D.C., da Silva, F.F., Roverato, M., Lana, C., 2017. Turmoil before the boring billion: Paleomagnetism of the 1880–1860Ma Uatumã event in the Amazonian craton. Gondwana Research 49, 106-129.

Avelar, V.G., Lafon, J.-M., Correia JR, F.C., Macambira, E.M.B., 1999. O Magmatismo arqueano da região de Tucumã-Província Mineral de Carajás: novos resultados geocronológicos. Brazilian Journal of Geology 29, 453-460.

Bazhenov, M.L., Levashova, N.M., Meert, J.G., 2016. How well do Precambrian paleomagnetic data agree with the Phanerozoic apparent polar wander path? A Baltica case study. Precambrian Research 285, 80-90.

Bettencourt, J.S., Juliani, C., Xavier, R.P., Monteiro, L.V.S., Bastos Neto, A.C., Klein, E.L., Assis, R.R., Leite, W.B., Moreto, C.P.N., Fernandes, C.M.D., Pereira, V.P., 2016. Metallogenetic systems associated with granitoid magmatism in the Amazonian Craton: An overview of the present level of understanding and exploration significance. Journal of South American Earth Sciences 68, 22-49.

Biggin, A.J., Strik, G.H., Langereis, C.G., 2009. The intensity of the geomagnetic field in the late-Archaean: new measurements and an analysis of the updated IAGA palaeointensity database. Earth Planet Sp 61, 9-22.

Biggin, A.J., Piispa, E.J., Pesonen, L.J., Holme, R., Paterson, G.A., Veikkolainen, T., Tauxe, L., 2015. Palaeomagnetic field intensity variations suggest Mesoproterozoic inner-core nucleation. Nature 526, 245-248.

Bingham, D.K., Evans, M.E., 1976. Paleomagnetism of the Great Slave Supergroup, Northwest Territories, Canada: the Stark Formation. Canadian Journal of Earth Sciences 13, 563-578.

Bispo-Santos, F., D'Agrella-Filho, M.S., Janikian, L., Reis, N.J., Trindade, R.I.F., Reis, M.A.A.A., 2014a. Towards Columbia: Paleomagnetism of 1980–1960 Ma Surumu volcanic rocks, Northern Amazonian Craton. Precambrian Research 244, 123-138.

Bispo-Santos, F., D'Agrella-Filho, M.S., Trindade, R.I.F., Janikian, L., Reis, N.J., 2014b. Was there SAMBA in Columbia? Paleomagnetic evidence from 1790 Ma Avanavero mafic sills (northern Amazonian Craton). Precambrian Research 244, 139-155.

Bleeker, W., 2003. The late Archean record: a puzzle in ca. 35 pieces. Lithos 71, 99-134.

Bogdanova, S.V., Gintov, O.B., Kurlovich, D.M., Lubnina, N.V., Nilsson, M.K.M., Orlyuk, M.I., Pashkevich, I.K., Shumlyanskyy, L.V., Starostenko, V.I., 2013. Late Palaeoproterozoic mafic dyking in the Ukrainian Shield of Volgo-Sarmatia caused by rotation during the assembly of supercontinent Columbia (Nuna). Lithos 174, 196-216.

Bogdanova, S.V., Gorbatschev, R., Garetsky, R.G., 2016. EUROPE|East European Craton☆, Reference Module in Earth Systems and Environmental Sciences. Elsevier, pp. 34-49.

Boone, G.M., 1969. Origin of clouded red feldspars; petrologic contrasts in a granitic porphyry intrusion. American Journal of Science 267, 633-668.
Borradaile, G.J., 1994. Low-temperature demagnetization and ice-pressure demagnetization in magnetite and haematite. Geophysical Journal International 116, 571-584.
Borradaile, G.J., Lucas, K., Middleton, R.S., 2004. Low-temperature demagnetization isolates stable magnetic vector components in magnetite-bearing diabase. Geophysical Journal International 157, 526-536.
Boyden, J.A., Müller, R.D., Gurnis, M., Torsvik, T.H., Clark, J.A., Turner, M., Ivey-Law, H., Watson, R.J., Cannon, J.S., 2011. Next-generation plate-tectonic reconstructions using GPlates. Geoinformatics: cyberinfrastructure for the solid earth sciences, 95-114.
Brown, M., Johnson, T., Gardiner, N.J., 2020. Plate Tectonics and the Archean Earth. Annual Review of Earth and Planetary Sciences 48, p.12.11-12.30.
Buchan, K.L., 2013. Key paleomagnetic poles and their use in Proterozoic continent and supercontinent reconstructions: A review. Precambrian Research 238, 93-110.
Caen-Vachette, M., 1988. The West African connection: Evolution of the central atlantic ocean and its Continental Margins Le craton ouest-africain et le bouclier guyanais: un seul craton au Protérozoïque inférieur? Journal of African Earth Sciences (and the Middle East) 7, 479-488.
Cassini, L.V., Moyen, J.-F., Juliani, C., 2020. Orosirian magmatism in the Tapajós Mineral Province (Amazonian Craton): The missing link to understand the onset of Paleoproterozoic tectonics. Lithos 356-357, 105350.
Chardon, D., Bamba, O., Traoré, K., 2020. Eburnean deformation pattern of Burkina Faso and the tectonic significance of shear zones in the West African craton. Bulletin de la Société Géologique de France 191.
Chew, D.M., Petrus, J.A., Kamber, B.S., 2014. U–Pb LA–ICPMS dating using accessory mineral standards with variable common Pb. Chemical Geology 363, 185-199.
Cogné, J.P., 2003. PaleoMac: A Macintosh™ application for treating paleomagnetic data and making plate reconstructions. Geochemistry, Geophysics, Geosystems 4, 1007.
Cohen, H.A., Gibbs, A.K., 1989. Is the equatorial atlantic discordant? Precambrian Research 42, 353-369.
Condie, K.C., 1998. Episodic continental growth and supercontinents: a mantle avalanche connection? Earth and Planetary Science Letters 163, 97-108.
Condie, K.C., 2002. The supercontinent cycle: are there two patterns of cyclicity? Journal of African Earth Sciences 35, 179-183.
Condie, K.C., Aster, R.C., 2013. Refinement of the supercontinent cycle with Hf, Nd and Sr isotopes. Geoscience Frontiers 4, 669-680.
Cordani, U.G., Teixeira, W., 2007. Proterozoic accretionary belts in the Amazonian Craton. Geological Society of America Memoirs 200, 297-320.
Creveling, J.R., Mitrovica, J.X., Chan, N.H., Latychev, K., Matsuyama, I., 2012. Mechanisms for oscillatory true polar wander. Nature 491, 244-248.
D'Agrella Filho, M.S., Trindade, R.I.F., Garcia, M.S.R., Ruiz, A.S., Bispo-Santos, F., Hollanda, M.H., 2018. The Planalto da Serra Alkaline-rock Complex: new 40Ar/39Ar ages and paleomagnetic results, and implications for the Gondwana formation, South American Symposium on Isotope Geology, 11th SSAGI, Cochabamba, Bolivia, p.71.
D'Agrella-Filho, M.S., Trindade, R.I.F., Tohver, E., Janikian, L., Teixeira, W., Hall, C., 2011. Paleomagnetism and 40Ar/39Ar geochronology of the high-grade metamorphic rocks of the Jequié block, São Francisco Craton: Atlantica, Ur and beyond. Precambrian Research 185, 183-201.

D'Agrella-Filho, M.S., Bispo-Santos, F., Trindade, R.I.F., Antonio, P.Y.J., 2016. Paleomagnetism of the Amazonian Craton and its role in paleocontinents. Brazilian Journal of Geology 46, 275-299.

Dall'Agnol, R., Lafon, J.M., Macambira, M.J.B., 1994. Proterozoic anorogenic magmatism in the Central Amazonian Province, amazonian araton: Geochronological, petrological and geochemical aspects. Mineralogy and Petrology 50, 113-138.

Dall'Agnol, R., Pichavant, M., Champenois, M., 1997. Iron-titanium oxide minerals of the Jamon Granite, eastern Amazonian region, Brazil: implications for the oxygen fugacity in Proterozoic, A-type granites. ANAIS-ACADEMIA BRASILEIRA DE CIENCIAS 69, 325-348.

Dall'Agnol, R., Teixeira, N.P., Rämö, O.T., Moura, C.A.V., Macambira, M.J.B., de Oliveira, D.C., 2005. Petrogenesis of the Paleoproterozoic rapakivi A-type granites of the Archean Carajás metallogenic province, Brazil. Lithos 80, 101-129.

Dall'Agnol, R., Oliveira, D.C., 2007. Oxidized, magnetite-series, rapakivi-type granites of Carajás, Brazil: Implications for classification and petrogenesis of A-type granites. Lithos 93, 215-233.

Dall'Agnol, R., Oliveira, M.d., Almeida, J.d., Althoff, F., Leite, A.d.S., Oliveira, D., Barros, C., 2006. Archean and paleoproterozoic granitoids of the Carajás Metallogenic Province, eastern Amazonian craton, Symposium on magmatism, crustal evolution and metallogenesis of the Amazoniam Craton, Belém, Excursion Guide, pp. 99-150.

Day, R., Fuller, M., Schmidt, V.A., 1977. Hysteresis properties of titanomagnetites: Grain-size and compositional dependence. Physics of the Earth and Planetary Interiors 13, 260-267.

De Min, A., Piccirillo, E.M., Marzoli, A., Bellieni, G., Renne, P.R., Ernesto, M., Marques, L.S., 2003. The Central Atlantic Magmatic Province (CAMP) in Brazil: petrology, geochemistry, 40Ar/39Ar ages, paleomagnetism and geodynamic implications. Geophysical Monograph Series 136, 91-128.

De Min, A., Hendriks, B., Slejko, F., Comin-Chiaramonti, P., Girardi, V., Ruberti, E., Gomes, C.B., Neder, R.D., Pinho, F.C., 2013. Age of ultramafic high-K rocks from Planalto da Serra (Mato Grosso, Brazil). Journal of South American Earth Sciences 41, 57-64.

Di Chiara, A., Muxworthy, A., Trindade, R., Bispo-Santos, F., 2017. Paleoproterozoic Geomagnetic Field Strength From the Avanavero Mafic Sills, Amazonian Craton, Brazil. Geochemistry, Geophysics, Geosystems 18, 3891-3903.

Dickinson, W.R., Gehrels, G.E., 2003. U–Pb ages of detrital zircons from Permian and Jurassic eolian sandstones of the Colorado Plateau, USA: paleogeographic implications. Sedimentary Geology 163, 29-66.

Domeier, M., Van der Voo, R., Torsvik, T.H., 2012. Paleomagnetism and Pangea: The road to reconciliation. Tectonophysics 514–517, 14-43.

Donadini, F., Elming, S.-Å., Tauxe, L., Hålenius, U., 2011. Paleointensity determination on a 1.786Ga old gabbro from Hoting, Central Sweden. Earth and Planetary Science Letters 309, 234-248.

Dunlop, D.J., Argyle, K.S., 1991. Separating multidomain and single-domain-like remanences in pseudo-single-domain magnetites (215–540 nm) by low-temperature demagnetization. Journal of Geophysical Research: Solid Earth 96, 2007-2017.

Dunlop, D.J., Özdemir, Ö., 2000. Effect of grain size and domain state on thermal demagnetization tails. Geophysical Research Letters 27, 1311-1314.

Ernst, R., Srivastava, R., Bleeker, W., Hamilton, M., 2010. Precambrian Large Igneous Provinces (LIPs) and their dyke swarms: New insights from high-precision geochronology integrated with paleomagnetism and geochemistry. Precambrian Research 183, vii-xi.

Ernst, R.E., Bleeker, W., Söderlund, U., Kerr, A.C., 2013. Large Igneous Provinces and supercontinents: Toward completing the plate tectonic revolution. Lithos 174, 1-14.
Ernst, R.E., 2014. Large igneous provinces. Cambridge University Press, p. 304.
Ernst, W.G., 2017. Earth's thermal evolution, mantle convection, and Hadean onset of plate tectonics. Journal of Asian Earth Sciences 145, 334-348.
Evans, D.A.D., Mitchell, R.N., 2011. Assembly and breakup of the core of Paleoproterozoic-Mesoproterozoic supercontinent Nuna. Geology 39, 443-446.
Evans, D.A.D., 2013. Reconstructing pre-Pangean supercontinents. Geological Society of America Bulletin 125, 1735-1751.
Evans, D.A.D., Li, Z.-X., Murphy, J.B., 2016. Four-dimensional context of Earth's supercontinents. Geological Society, London, Special Publications 424, 1-14.
Evans, M.E., Bingham, D.K., 1976. Paleomagnetism of the Great Slave Supergroup, Northwest Territories, Canada: the Tochatwi Formation. Canadian Journal of Earth Sciences 13, 555-562.
Fernandes, C.M.D., Juliani, C., Monteiro, L.V.S., Lagler, B., Echeverri Misas, C.M., 2011. High-K calc-alkaline to A-type fissure-controlled volcano-plutonism of the São Félix do Xingu region, Amazonian craton, Brazil: Exclusively crustal sources or only mixed Nd model ages? Journal of South American Earth Sciences 32, 351-368.
Feybesse, J.-L., Milési, J.-P., 1994. The Archaean/Proterozoic contact zone in West Africa: a mountain belt of décollement thrusting and folding on a continental margin related to 2.1 Ga convergence of Archaean cratons? Precambrian Research 69, 199-227.
Fisher, R., 1953. Dispersion on a Sphere. Proceedings of the Royal Society of London. Series A. Mathematical and Physical Sciences 217, 295-305.
Garcia, M.S., Trindade, R.I., Manoel, S., Pinho, F.E., 2013. Paleomagnetismo do complexo alcalino Planalto da Serra (Mato Grosso): Implicações para a formação do Gondwana, In: Letters, L. (Ed.), Latinmag Letters, Montevideo, pp. OB19, 11-18.
Giovanardi, T., Girardi, V.A.V., Teixeira, W., Mazzucchelli, M., 2019. Mafic dyke swarms at 1882, 535 and 200 Ma in the Carajás region, Amazonian Craton: SrNd isotopy, trace element geochemistry and inferences on their origin and geological settings. Journal of South American Earth Sciences 92, 197-208.
Goldreich, P., Toomre, A., 1969. Some remarks on polar wandering. Journal of Geophysical Research 74, 2555-2567.
Gong, Z., Xu, X., Evans, D.A.D., Hoffman, P.F., Mitchell, R.N., Bleeker, W., 2018. Paleomagnetism and rock magnetism of the ca. 1.87 Ga Pearson Formation, Northwest Territories, Canada: A test of vertical-axis rotation within the Great Slave basin. Precambrian Research 305, 295-309.
Grenholm, M., 2019. The global tectonic context of the ca. 2.27-1.96 Ga Birimian Orogen – Insights from comparative studies, with implications for supercontinent cycles. Earth-Science Reviews 193, 260-298.
Halls, H.C., 1978. The use of converging remagnetization circles in palaeomagnetism. Physics of the Earth and Planetary Interiors 16, 1-11.
Hanson, R.E., Gose, W.A., Crowley, J.L., Ramezani, J., Bowring, S.A., Bullen, D.S., Hall, R.P., Pancake, J.A., Mukwakwami, J., 2004. Paleoproterozoic intraplate magmatism and basin development on the Kaapvaal Craton: Age, paleomagnetism and geochemistry of ~1.93 to ~1.87 Ga post-Waterberg dolerites. South African Journal of Geology 107, 233-254.
Hanson, R.E., Rioux, M., Gose, W.A., Blackburn, T.J., Bowring, S.A., Mukwakwami, J., Jones, D.L., 2011. Paleomagnetic and geochronological evidence for large-scale post–1.88 Ga displacement between the Zimbabwe and Kaapvaal cratons along the Limpopo belt. Geology 39, 487-490.

Hyodo, H., Dunlop, D.J., 1993. Effect of anisotropy on the paleomagnetic contact test for a Grenville Dike. Journal of Geophysical Research: Solid Earth 98, 7997-8017.
Isley, A.E., Abbott, D.H., 1999. Plume-related mafic volcanism and the deposition of banded iron formation. Journal of Geophysical Research: Solid Earth 104, 15461-15477.
Johansson, Å., 2009. Baltica, Amazonia and the SAMBA connection—1000 million years of neighbourhood during the Proterozoic? Precambrian Research 175, 221-234.
Juliani, C., Fernandes, C.M.D., 2010. Well-preserved Late Paleoproterozoic volcanic centers in the São Félix do Xingu region, Amazonian Craton, Brazil. Journal of Volcanology and Geothermal Research 191, 167-179.
Kilian, T.M., Chamberlain, K.R., Evans, D.A.D., Bleeker, W., Cousens, B.L., 2016. Wyoming on the run—Toward final Paleoproterozoic assembly of Laurentia. Geology 44, 863-866.
Kirschvink, J.L., 1980. The least-squares line and plane and the analysis of palaeomagnetic data. Geophysical Journal International 62, 699-718.
Kirschvink, J.L., Ripperdan, R.L., Evans, D.A., 1997. Evidence for a Large-Scale Reorganization of Early Cambrian Continental Masses by Inertial Interchange True Polar Wander. Science 277, 541-545.
Kirschvink, J.L., Kopp, R.E., Raub, T.D., Baumgartner, C.T., Holt, J.W., 2008. Rapid, precise, and high-sensitivity acquisition of paleomagnetic and rock-magnetic data: Development of a low-noise automatic sample changing system for superconducting rock magnetometers. Geochemistry, Geophysics, Geosystems 9.
Klein, E.L., Moura, C.A.V., 2008. São Luís Craton and Gurupi Belt (Brazil): possible links with the West African Craton and surrounding Pan-African belts. Geological Society, London, Special Publications 294, 137-151.
Kruiver, P.P., Dekkers, M.J., Heslop, D., 2001. Quantification of magnetic coercivity components by the analysis of acquisition curves of isothermal remanent magnetisation. Earth and Planetary Science Letters 189, 269-276.
Ledru, P., Lasserre, J.-L., Manier, E., Mercier, D., 1991. Le Protérozoïque inférieur nord guyanais: révision de la lithologie, tectonique transcurrente et dynamique des bassins sédimentaires. Bull. Soc. Géol. France 162, 627-636.
Ledru, P., Johan, V., Milési, J.P., Tegyey, M., 1994. Markers of the last stages of the Palaeoproterozoic collision: evidence for a 2 Ga continent involving circum-South Atlantic provinces. Precambrian Research 69, 169-191.
Li, Z.-X., Evans, D.A.D., Halverson, G.P., 2013. Neoproterozoic glaciations in a revised global palaeogeography from the breakup of Rodinia to the assembly of Gondwanaland. Sedimentary Geology 294, 219-232.
Liu, H., Sun, W.-d., Zartman, R., Tang, M., 2019. Continuous plate subduction marked by the rise of alkali magmatism 2.1 billion years ago. Nature Communications 10, 3408.
Liu, Y., Li, Z.-X., Pisarevsky, S., Kirscher, U., Mitchell, R.N., Stark, J.C., 2018. Palaeomagnetism of the 1.89 Ga Boonadgin dykes of the Yilgarn Craton: Possible connection with India. Precambrian Research 329, 211-223.
Lubnina, N.V., Pasenko, A.M., Novikova, M.A., Bubnov, A.Y., 2016. The East European craton at the end of the Paleoproterozoic: A new paleomagnetic pole of 1.79–1.75 Ga. Moscow Univ. Geol. Bull. 71, 8-17.
Ludwig, K., 2009. Isoplot 4.1. A geochronological toolkit for Microsoft Excel. Berkeley Geochronology Center Special Publication 4, 76.
McDowell, F.W., McIntosh, W.C., Farley, K.A., 2005. A precise 40Ar–39Ar reference age for the Durango apatite (U–Th)/He and fission-track dating standard. Chemical Geology 214, 249-263.

McElhinny, M., 1964. Statistical significance of the fold test in palaeomagnetism. Geophysical Journal International 8, 338-340.
McFadden, P.L., McElhinny, M.W., 1990. Classification of the reversal test in palaeomagnetism. Geophysical Journal International 103, 725-729.
McGlynn, J.C., Irving, E., 1978. Multicomponent magnetization of the Pearson Formation (Great Slave Supergroup, N.W.T.) and the Coronation loop. Canadian Journal of Earth Sciences 15, 642-654.
Meert, J.G., 2012. What's in a name? The Columbia (Paleopangaea/Nuna) supercontinent. Gondwana Research 21, 987-993.
Meert, J.G., Santosh, M., 2017. The Columbia supercontinent revisited. Gondwana Research 50, 67-83.
Merdith, A.S., Collins, A.S., Williams, S.E., Pisarevsky, S., Foden, J.F., Archibald, D., Blades, M.L., Alessio, B.L., Armistead, S., Plavsa, D., Clark, C., Müller, R.D., 2017. A full-plate global reconstruction of the Neoproterozoic. Gondwana Research.
Mitchell, R.N., Hoffman, P.F., Evans, D.A.D., 2010. Coronation loop resurrected: Oscillatory apparent polar wander of Orosirian (2.05–1.8Ga) paleomagnetic poles from Slave craton. Precambrian Research 179, 121-134.
Mitchell, R.N., 2014. True polar wander and supercontinent cycles: Implications for lithospheric elasticity and the triaxial earth. American Journal of Science 314, 966-979.
Moreira, G., 2019. PALEOMAGNETISMO DA FORMAÇÃO PENATECAUA DA PROVÍNCIA MAGMÁTICA DO ATLÂNTICO CENTRAL NA BACIA AMAZÔNICA, BRASIL, Instituto de Astronomia, Geofísica e Ciências Atmosféricas - Departamento de Geofísica. University of São Paulo, p. p. 63.
Murphy, J.B., 2013. Whither the supercontinent cycle? Geology 41, 815-816.
Nance, D., Worsley, T.R., Moody, J.B., 1988. The supercontinent cycle. Scientific American 259, 72-79.
Nance, D., Murphy, J.B., 2013. Origins of the supercontinent cycle. Geoscience Frontiers 4, 439-448.
Nance, R.D., Murphy, J.B., Santosh, M., 2014. The supercontinent cycle: A retrospective essay. Gondwana Research 25, 4-29.
Navarro, M., Tonetto, E., Oliveira, E., 2015. LA-SF-ICP-MS U-Pb Zircon Dating at University of Campinas, Brazil. Geonalysis-2015, Wien, August.
Nédélec, A., Bouchez, J.-L., 2015. Granites: Petrology, Structure, Geological Setting, and Metallogeny. OUP Oxford.
Nédélec, A., Trindade, R., Peschler, A., Archanjo, C., Macouin, M., Poitrasson, F., Bouchez, J.-L., 2015. Hydrothermally-induced changes in mineralogy and magnetic properties of oxidized A-type granites. Lithos 212–215, 145-157.
Neres, M., Silva, P.F., Ikenne, M., Martins, S., Hafid, A., Mata, J., Almeida, F., Youbi, N., Boumehdi, M.A., 2016. Evidences for multiple remagnetization of Proterozoic dykes from Iguerda inlier (Anti-Atlas Belt, Southern Morocco). Stud Geophys Geod 60, 700-730.
Nomade, S., Théveniaut, H., Chen, Y., Pouclet, A., Rigollet, C., 2000. Paleomagnetic study of French Guyana Early Jurassic dolerites: hypothesis of a multistage magmatic event. Earth and Planetary Science Letters 184, 155-168.
Nomade, S., Chen, Y., Féraud, G., Pouclet, A., Théveniaut, H., 2001. First paleomagnetic and 40Ar/39Ar study of Paleoproterozoic rocks from the French Guyana (Camopi and Oyapok rivers), northeastern Guyana Shield. Precambrian Research 109, 239-256.
Nomade, S., Chen, Y., Pouclet, A., Féraud, G., Théveniaut, H., Daouda, B.Y., Vidal, M., Rigolet, C., 2003. The Guiana and the West African Shield Palaeoproterozoic

grouping: new palaeomagnetic data for French Guiana and the Ivory Coast. Geophysical Journal International 154, 677-694.
Oliveira, D.C., 2006. Modelos de evolução e colocação dos grantitos paleoproterozóicos da Suíte Jamon, SE do Cráton Amazônico. Tese de douturado. Universidade Federal do Pará, p.186.
Onstott, T., Hargraves, R.B., 1981. Proterozoic transcurrent tectonics: palaeomagnetic evidence from Venezuela and Africa. Nature 289, 131-136.
Onstott, T., Hargraves, R., York, D., 1984a. Dating of Precambrian diabase dikes of Venezuela using paleomagnetic and 40Ar/39Ar methods. Anais II do Simpósio Amazônico, Manaus, Brasil, DNPM 2, 513-518.
Onstott, T., Hargraves, R.B., York, D., Hall, C., 1984b. Constraints on the motions of South American and African Shields during the Proterozoic: I. 40Ar/39Ar and paleomagnetic correlations between Venezuela and Liberia. Geological Society of America Bulletin 95, 1045-1054.
Onstott, T.C., Dorbor, J., 1987. 40Ar/39Ar and paleomagnetic results from Liberia and the Precambrian APW data base for the West African Shield. Journal of African Earth Sciences (1983) 6, 537-552.
Paquette, J.-L., Piro, J.-L., Devidal, J.-L., Bosse, V., Didier, A., Sannac, S., Abdelnour, Y., 2014. Sensitivity enhancement in LA-ICP-MS by N2 addition to carrier gas: application to radiometric dating of U-Th-bearing minerals. Agilent ICP-MS Journal 58, 4-5.
Paton, C., Hellstrom, J., Paul, B., Woodhead, J., Hergt, J., 2011. Iolite: Freeware for the visualisation and processing of mass spectrometric data. Journal of Analytical Atomic Spectrometry 26, 2508-2518.
Pehrsson, S.J., Eglington, B.M., Evans, D.A.D., Huston, D., Reddy, S.M., 2016. Metallogeny and its link to orogenic style during the Nuna supercontinent cycle. Geological Society, London, Special Publications 424, 83-94.
Peucat, J.-J., Capdevila, R., Drareni, A., Mahdjoub, Y., Kahoui, M., 2005. The Eglab massif in the West African Craton (Algeria), an original segment of the Eburnean orogenic belt: petrology, geochemistry and geochronology. Precambrian Research 136, 309-352.
Pimentel, M., Machado, N., 1994. Geocronologia U-Pb dos terrenos granito-greenstone de Rio Maria, Pará, SBG, Congresso Brasileiro de Geologia, pp. 390-391.
Pinho, S., Fernandes, C., Teixeira, N., Paiva Jr, A., Cruz, V., Lamarão, C., Moura, C., 2006. O magmatismo paleoproterozóico da região de São Félix do Xingu, Província Estanífera do sul do Pará: Petrografia e Geocronologia. Revista Brasileira de Geociências 36, 724-732.
Piper, J.D.A., Lomax, K., 1973. Palaeomagnetism of Precambrian Birrimian and Tarkwaian Rocks of West Africa. Geophysical Journal International 34, 435-450.
Pisarevsky, S.A., Elming, S.-Å., Pesonen, L.J., Li, Z.-X., 2014. Mesoproterozoic paleogeography: Supercontinent and beyond. Precambrian Research 244, 207-225.
Pivarunas, A.F., Meert, J.G., Miller, S.R., 2018. Assessing the intersection/remagnetization puzzle with synthetic apparent polar wander paths. Geophysical Journal International 214, 1164-1172.
Pochon, A., Poujol, M., Gloaguen, E., Branquet, Y., Cagnard, F., Gumiaux, C., Gapais, D., 2016. U-Pb LA-ICP-MS dating of apatite in mafic rocks: Evidence for a major magmatic event at the Devonian-Carboniferous boundary in the Armorican Massif (France). American Mineralogist 101, 2430-2442.

Raub, T., Kirschvink, J., Evans, D., 2007. True polar wander: Linking deep and shallow geodynamics to hydro-and bio-spheric hypotheses. Treatise on Geophysics 5, 565-589.

Renne, P., Onstott, T., Jorge João, X., 1988. 40Ar/39Ar and paleomagnetic results from the Guaporé Shield: further implications for the nature of Middle-Late Proterozoic mobile belts of Gondwanaland. SBG, Congr. Lat.-Amer. Geol 7, 348-362.

Rivalenti, G., Williamson, A., Feyer, A.M., Mazzucchelli, M., Girardi, V.A.V., Cavazzini, G., Finatti, C., Barbieri, M.A., Teixeira, W., 1998. Petrogenesis of the Paleoproterozoic basalt-andesite-rhyolite dyke association in the Carajas region, Amazonian craton. Lithos 43, 235-265.

Roberts, A.P., Heslop, D., Zhao, X., Pike, C.R., 2014. Understanding fine magnetic particle systems through use of first-order reversal curve diagrams. Reviews of Geophysics 52, 557-602.

Roberts, A.P., Almeida, T.P., Church, N.S., Harrison, R.J., Heslop, D., Li, Y., Li, J., Muxworthy, A.R., Williams, W., Zhao, X., 2017. Resolving the Origin of Pseudo-Single Domain Magnetic Behavior. Journal of Geophysical Research: Solid Earth 122, 9534-9558.

Roberts, N.M.W., 2013. The boring billion? - Lid tectonics, continental growth and environmental change associated with the Columbia supercontinent. Geoscience Frontiers.

Rodrigues, P.R.S., Lamarão, C.N., da Costa, H.d.N.S., Oliveira, D.C., Galarza, M.A., Sotero, A.d.M., 2015. Petrografia, geoquímica e geocronologia de diques máficos a félsicos da região de Água Azul do Norte, sudeste do Pará, Província Carajás. Bol. Mus. Para. Emílio Goeldi. Cienc. Nat., Belém 10, p. 311-339.

Rosa-Costa, L.T., Lafon, J.M., Delor, C., 2006. Zircon geochronology and Sm–Nd isotopic study: Further constraints for the Archean and Paleoproterozoic geodynamical evolution of the southeastern Guiana Shield, north of Amazonian Craton, Brazil. Gondwana Research 10, 277-300.

Rose, I., Buffett, B., 2017. Scaling rates of true polar wander in convecting planets and moons. Physics of the Earth and Planetary Interiors 273, 1-10.

Roverato, M., 2016. The Montesbelos mass-flow (southern Amazonian craton, Brazil): a Paleoproterozoic volcanic debris avalanche deposit? Bulletin of Volcanology 78, 1-6.

Roverato, M., Giordano, D., Giovanardi, T., Juliani, C., Polo, L., 2019. The 2.0–1.88 Ga Paleoproterozoic evolution of the southern Amazonian Craton (Brazil): An interpretation inferred by lithofaciological, geochemical and geochronological data. Gondwana Research.

Sabaté, P., Lomax, K., 1975. Données stratigraphiques et paléomagnétiques de la région Yetti-Eglab (Sahara occidental algérien).

Santos, J.O.S., Hartmann, L.A., Gaudette, H.E., Groves, D.I., McNaughton, N.J., Fletcher, I.R., 2000. A New Understanding of the Provinces of the Amazon Craton Based on Integration of Field Mapping and U-Pb and Sm-Nd Geochronology. Gondwana Research 3, 453-488.

Santos, J.O.S., 2003. Geotectônica do Escudo das Guianas e Brasil-Central, Geologia, Tectônica e Recursos Minerais do Brasil. Texto, mapas & SIG: CPRM—Serviço Geológico do Brasil, pp. 169-226.

Santos, M.N.S.d., Oliveira, D.C., 2016. Rio Maria granodiorite and associated rocks of Ourilândia do Norte – Carajás province: Petrography, geochemistry and implications for sanukitoid petrogenesis. Journal of South American Earth Sciences 72, 279-301.

Schobbenhaus, C., Campos, D.A., Derze, G.R., Asmus, H.E., 1984. Geologia do Brasil: texto explicativo do mapa geológico do Brasil e da área oceânica adjacente incluindo

depósitos minerais, escala 1: 2 5000 000. Divisão de Geologia e Mineralogia, Departamento Nacional da Produção Mineral.
Schoene, B., Bowring, S.A., 2006. U–Pb systematics of the McClure Mountain syenite: thermochronological constraints on the age of the 40 Ar/39 Ar standard MMhb. Contrib Mineral Petrol 151, 615.
Shcherbakova, V.V., Shcherbakov, V.P., Heider, F., 2000. Properties of partial thermoremanent magnetization in pseudosingle domain and multidomain magnetite grains. Journal of Geophysical Research: Solid Earth 105, 767-781.
Shirey, S.B., Richardson, S.H., 2011. Start of the Wilson Cycle at 3 Ga Shown by Diamonds from Subcontinental Mantle. Science 333, 434-436.
Silva, C., Lima, M.d., Andrade, A.d., Isler, R., Guimarães, G., Leal, J., Basei, M., D'lagnol, R., Teixeira, J., Montalvão, R., 1974. Folha SB-22 (Araguaia) e parte da Folha SC-22 (Tocantins). Projeto RadamBrasil, 143.
Silva, F.F., de Oliveira, D.C., Antonio, P.Y.J., D'Agrella Filho, M.S., Lamarão, C.N., 2016. Bimodal magmatism of the Tucumã area, Carajás province: U-Pb geochronology, classification and processes. Journal of South American Earth Sciences 72, 95-114.
Silva Jr, R., Dall'Agnol, R., Oliveira, E., 1999. Geologia, petrografia e geoquímica dos diques proterozóicos da região de Rio Maria, sudeste do Pará. Geochimica Brasiliensis 13, 161-183.
Söderlund, U., Klausen, M.B., Ernst, R.E., Bleeker, W., 2016. New advances in using large igneous provinces (LIPs) to reconstruct ancient supercontinents. GFF 138, 1-5.
Stacey, J.S., Kramers, J.D., 1975. Approximation of terrestrial lead isotope evolution by a two-stage model. Earth and Planetary Science Letters 26, 207-221.
Stampfli, G.M., Hochard, C., Vérard, C., Wilhem, C., vonRaumer, J., 2013. The Formation of Pangea. Tectonophysics 593, 1-19.
Stark, J.C., Wang, X.-C., Denyszyn, S.W., Li, Z.-X., Rasmussen, B., Zi, J.-W., Sheppard, S., Liu, Y., 2019. Newly identified 1.89 Ga mafic dyke swarm in the Archean Yilgarn Craton, Western Australia suggests a connection with India. Precambrian Research 329, 156-169.
Swanson-Hysell, N.L., Kilian, T.M., Hanson, R.E., 2015. A new grand mean palaeomagnetic pole for the 1.11 Ga Umkondo large igneous province with implications for palaeogeography and the geomagnetic field. Geophysical Journal International 203, 2237-2247.
Tassinari, C.C., Munhá, J.M., Teixeira, W., Palácios, T., Nutman, A.P., Sosa, C., Santos, A.P., Calado, B.O., 2004. The Imataca Complex, NW Amazonian Craton, Venezuela: crustal evolution and integration of geochronological and petrological cooling histories. Episodes-Newsmagazine of the International Union of Geological Sciences 27(1), 3-12.
Tassinari, C.C.G., Macambira, M., 2004. A evolução tectonica do Craton Amazonico, In: (Org.), V.M.-N.A.B.C.D.R.C.B.B.d.B.N. (Ed.), Geologia do Continente Sul Americano: Evolução da obra de F.F.M. de Ameida. BECA, São Paulo, pp. p. 471-486.
Teixeira, M.F.B., Dall'Agnol, R., Schneider Santos, J.O., Carvalho de Oliveira, D., Lamarão, C.N., McNaughton, N.J., 2018. Crystallization ages of Paleoproterozoic A-type granites of Carajás province, Amazon craton: Constraints from U-Pb geochronology of zircon and titanite. Journal of South American Earth Sciences 88, 312-331.
Teixeira, M.F.B., Dall'Agnol, R., Santos, J.O.S., Kemp, A., Evans, N., 2019a. Petrogenesis of the Paleoproterozoic (Orosirian) A-type granites of Carajás Province, Amazon Craton, Brazil: Combined in situ HfO isotopes of zircon. Lithos 332-333, 1-22.

Teixeira, W., Hamilton, M.A., Ernst, R.E., Girardi, V.A.V., 2012a. 200 Ma dyke swarm in the Carajás province, Amazonian craton, South America: distal part of the CAMP event, Reconstruction of Supercontinents Back To 2.7 Ga Using The Large Igneous Province (LIP) Record: With Implications For Mineral Deposit Targeting, Hydrocarbon Resource Exploration, and Earth System Evolution.

Teixeira, W., Hamilton, M.A., Ernst, R.E., Girardi, V.A.V., Evans, D.A.D., 2012b. 535 Ma dyke swarm in the Carajás province, Amazonian craton, South America: potential part of a regional intraplate event, Reconstruction of Supercontinents Back To 2.7 Ga Using The Large Igneous Province (LIP) Record: With Implications For Mineral Deposit Targeting, Hydrocarbon Resource Exploration, and Earth System Evolution, pp. 1-11.

Teixeira, W., Hamilton, M., Girardi, V.A.V., Faleiros, F.M., Ernst, R.E., 2019b. U-Pb baddeleyite ages of key dyke swarms in the Amazonian Craton (Carajás/Rio Maria and Rio Apa areas): tectonic implications for events at 1880, 1110 Ma, 535 Ma and 200 Ma. Precambrian Research 329, 138-155.

Théveniaut, H., Delor, C., Lafon, J.M., Monié, P., Rossi, P., Lahondère, D., 2006. Paleoproterozoic (2155–1970 Ma) evolution of the Guiana Shield (Transamazonian event) in the light of new paleomagnetic data from French Guiana. Precambrian Research 150, 221-256.

Thomson, S.N., Gehrels, G.E., Ruiz, J., Buchwaldt, R., 2012. Routine low-damage apatite U-Pb dating using laser ablation–multicollector–ICPMS. Geochemistry, Geophysics, Geosystems 13.

Trindade, R.I.F., Font, E., D'Agrella-Filho, M.S., Nogueira, A.C.R., Riccomini, C., 2003. Low-latitude and multiple geomagnetic reversals in the Neoproterozoic Puga cap carbonate, Amazon craton. Terra Nova 15, 441-446.

Valério, C.d.S., Macambira, M.J.B., Souza, V.d.S., Dantas, E.L., Nardi, L.V.S., 2018. 1.88Ga São Gabriel AMCG association in the southernmost Uatumã-Anauá Domain: Petrological implications for post-collisional A-type magmatism in the Amazonian Craton. Lithos 300-301, 291-313.

Van der Voo, R., 1990. The reliability of paleomagnetic data. Tectonophysics 184, 1-9.

Vanderhaeghe, O., Ledru, P., Thiéblemont, D., Egal, E., Cocherie, A., Tegyey, M., Milési, J.-P., 1998. Contrasting mechanism of crustal growth: Geodynamic evolution of the Paleoproterozoic granite–greenstone belts of French Guiana. Precambrian Research 92, 165-193.

Vasquez, L., Rosa-Costa, L., Silva, C., Ricci, P., Barbosa, J., Klein, E., Lopes, E., Macambira, E., Chaves, C., Carvalho, J., 2008. Geologia e Recursos Minerais do Estado do Pará: Sistema de Informações Geográficas-SIG: texto explicativo dos mapas Geológico e Tectônico e de Recursos Minerais do Estado do Pará. Organizadores, Vasquez ML, Rosa-Costa LT Escala 1, 000.

Veikkolainen, T., Pesonen, L., Korhonen, K., 2014. An analysis of geomagnetic field reversals supports the validity of the Geocentric Axial Dipole (GAD) hypothesis in the Precambrian. Precambrian Research 244, 33-41.

Veikkolainen, T., Heimpel, M., Evans, M.E., Pesonen, L.J., Korhonen, K., 2017a. A paleointensity test of the geocentric axial dipole (GAD) hypothesis. Physics of the Earth and Planetary Interiors 265, 54-61.

Veikkolainen, T.H., Biggin, A.J., Pesonen, L.J., Evans, D.A., Jarboe, N.A., 2017b. Advancing Precambrian palaeomagnetism with the PALEOMAGIA and PINT((QPI)) databases. Scientific Data 4, 170068.

Veselovskiy, R.V., Samsonov, A.V., Stepanova, A.V., Salnikova, E.B., Larionova, Y.O., Travin, A.V., Arzamastsev, A.A., Egorova, S.V., Erofeeva, K.G., Stifeeva, M.V.,

Shcherbakova, V.V., Shcherbakov, V.P., Zhidkov, G.V., Zakharov, V.S., 2019. 1.86 Ga key paleomagnetic pole from the Murmansk craton intrusions – Eastern Murman Sill Province, NE Fennoscandia: Multidisciplinary approach and paleotectonic applications. Precambrian Research 324, 126-145.

Warnock, A.C., Kodama, K.P., Zeitler, P.K., 2000. Using thermochronometry and low-temperature demagnetization to accurately date Precambrian paleomagnetic poles. Journal of Geophysical Research: Solid Earth 105, 19435-19453.

Whitney, D.L., Evans, B.W., 2010. Abbreviations for names of rock-forming minerals. American Mineralogist 95, 185-187.

Wiedenbeck, M., Alle, P., Corfu, F., Griffin, W., Meier, M., Oberli, F.v., Quadt, A.v., Roddick, J., Spiegel, W., 1995. Three natural zircon standards for U-Th-Pb, Lu-Hf, trace element and REE analyses. Geostandards newsletter 19, 1-23.

Worsley, T.R., Nance, D., Moody, J.B., 1984. Global tectonics and eustasy for the past 2 billion years. Marine Geology 58, 373-400.

Zhang, S., Li, Z.-X., Evans, D.A.D., Wu, H., Li, H., Dong, J., 2012. Pre-Rodinia supercontinent Nuna shaping up: A global synthesis with new paleomagnetic results from North China. Earth and Planetary Science Letters 353–354, 145-155.

Zhao, G., Sun, M., Wilde, S.A., 2002. Did South America and West Africa Marry and Divorce or Was it a Long-lasting Relationship? Gondwana Research 5, 591-596.

Zhao, G., Sun, M., Wilde, S.A., Li, S., 2004. A Paleo-Mesoproterozoic supercontinent: assembly, growth and breakup. Earth-Science Reviews 67, 91-123.

Zijderveld, J., 1967. AC demagnetization of rocks: analysis of results. Methods in paleomagnetism 3, 254.

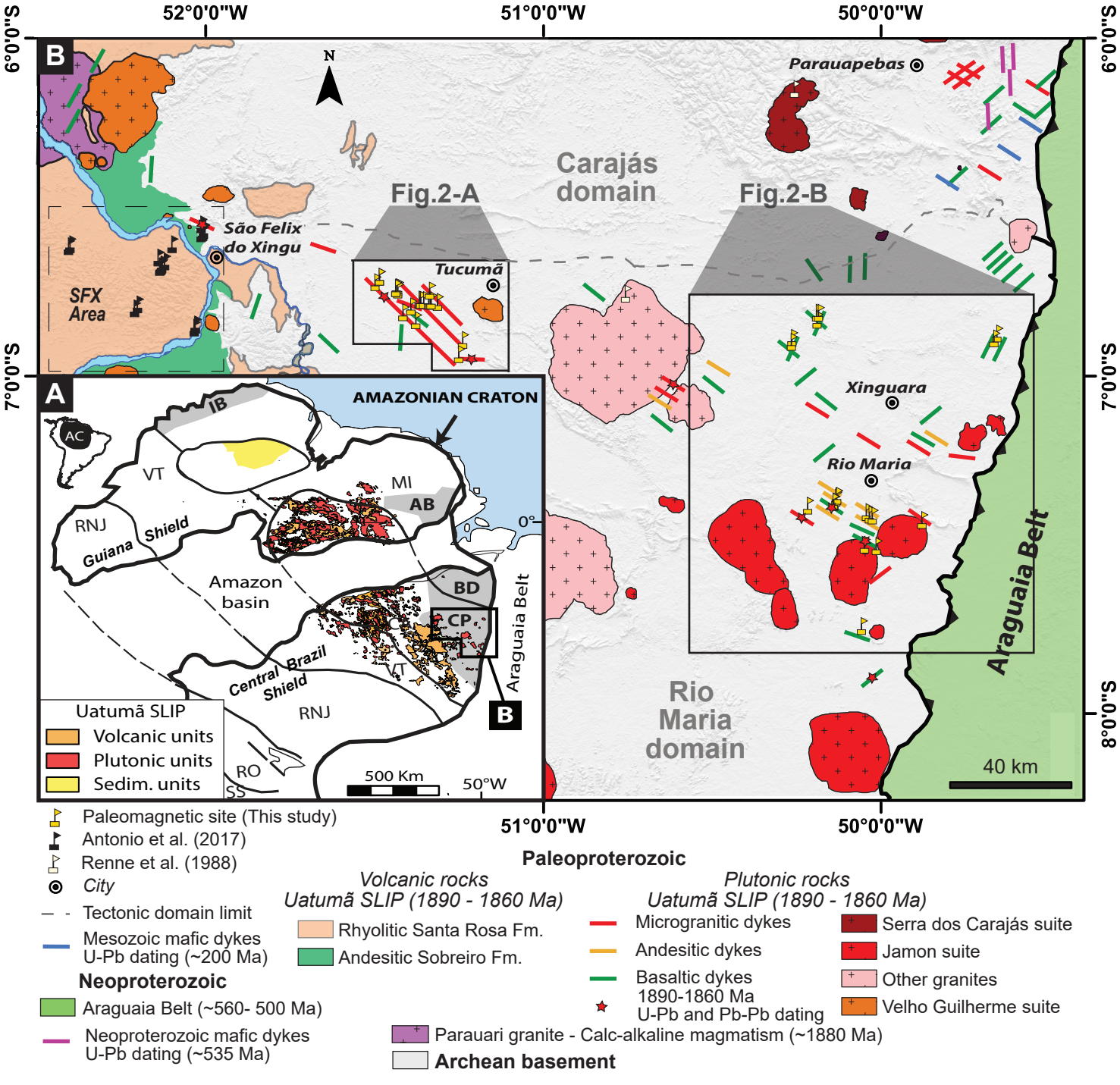
52°0'0"W
51°0'0"W
50°0'0"W
6°0'0"S
7°0'0"S
8°0'0"S
B
N
Parauapebas
Carajás domain
Fig.2-A
Fig.2-B
São Felix do Xingu
SFX Area
Tucumã
Xinguara
Rio Maria
Araguaia Belt
Rio Maria domain
40 km
A
AMAZONIAN CRATON
IB
AC
VT
MI
AB
RNJ
Guiana Shield
Amazon basin
BD
CP
Central Brazil Shield
RO
SS
0°
500 Km
50°W
Uatumã SLIP
Volcanic units
Plutonic units
Sedim. units
Paleomagnetic site (This study)
Antonio et al. (2017)
Renne et al. (1988)
City
Tectonic domain limit
Mesozoic mafic dykes U-Pb dating (~200 Ma)
Neoproterozoic
Araguaia Belt (~560- 500 Ma)
Neoproterozoic mafic dykes U-Pb dating (~535 Ma)
Paleoproterozoic
Volcanic rocks Uatumã SLIP (1890 - 1860 Ma)
Rhyolitic Santa Rosa Fm.
Andesitic Sobreiro Fm.
Plutonic rocks Uatumã SLIP (1890 - 1860 Ma)
Microgranitic dykes
Andesitic dykes
Basaltic dykes
1890-1860 Ma U-Pb and Pb-Pb dating
Serra dos Carajás suite
Jamon suite
Other granites
Velho Guilherme suite
Parauari granite - Calc-alkaline magmatism (~1880 Ma)
Archean basement

Figure1

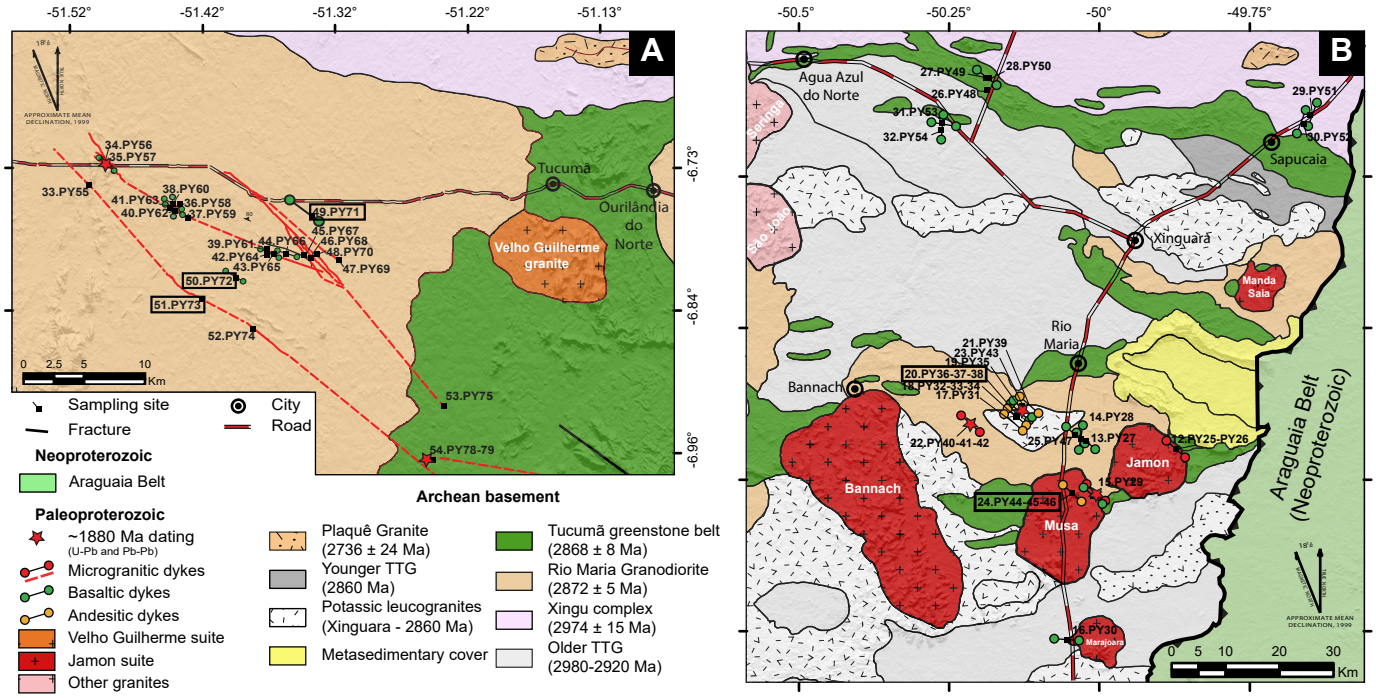
A
B
-51.52°
-51.42°
-51.32°
-51.22°
-51.13°
-6.73°
-6.84°
-6.96°
-50.5°
-50.25°
-50°
-49.75°
-7°
-7.25°
-7.5°
-7.75°
Tucumã
Ourilândia do Norte
Velho Guilherme granite
Agua Azul do Norte
Sapucaia
Xinguara
Rio Maria
Bannach
Jamon
Musa
Manda Saia
Araguaia Belt (Neoproterozoic)
Marajoara
Km
Sampling site
Fracture
City
Road
Neoproterozoic
Araguaia Belt
Paleoproterozoic
~1880 Ma dating
(U-Pb and Pb-Pb)
Microgranitic dykes
Basaltic dykes
Andesitic dykes
Velho Guilherme suite
Jamon suite
Other granites
Archean basement
Plaquê Granite
(2736 ± 24 Ma)
Younger TTG
(2860 Ma)
Potassic leucogranites
(Xinguara - 2860 Ma)
Metasedimentary cover
Tucumã greenstone belt
(2868 ± 8 Ma)
Rio Maria Granodiorite
(2872 ± 5 Ma)
Xingu complex
(2974 ± 15 Ma)
Older TTG
(2980-2920 Ma)

Figure 2

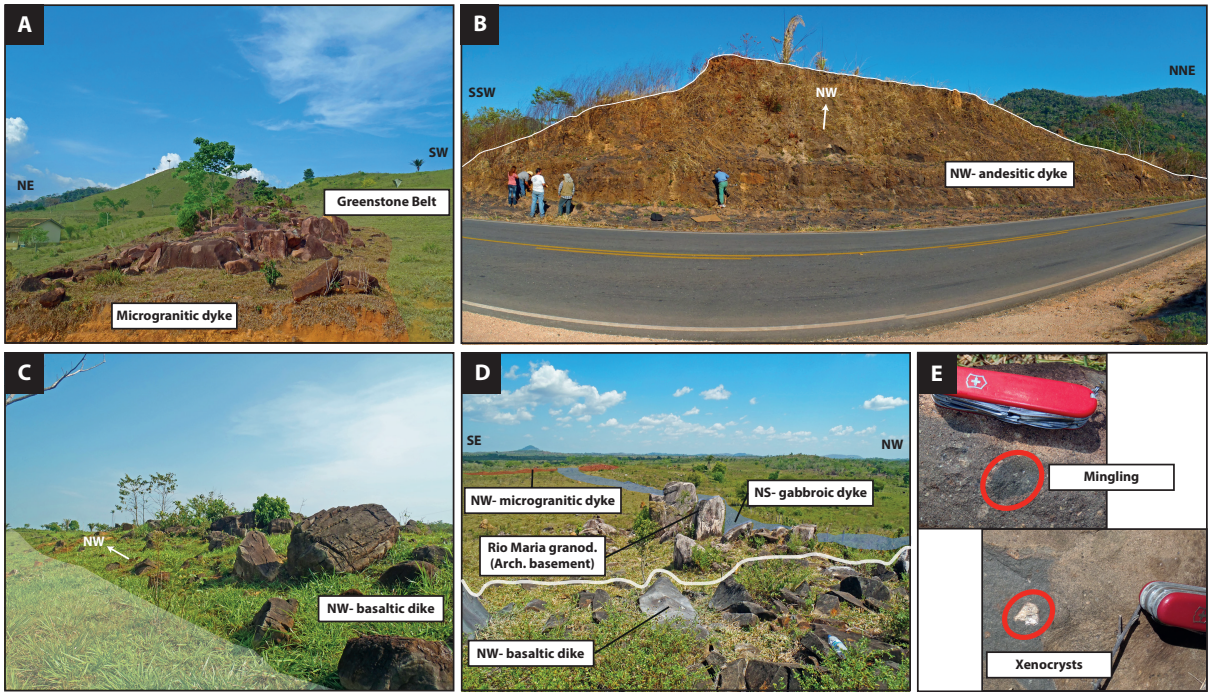
A
NE
SW
Greenstone Belt
Microgranitic dyke
B
SSW
NW
NNE
NW- andesitic dyke
C
NW
NW- basaltic dike
D
SE
NW
NW- microgranitic dyke
NS- gabbroic dyke
Rio Maria granod.
(Arch. basement)
NW- basaltic dike
E
Mingling
Xenocrysts

Figure 3

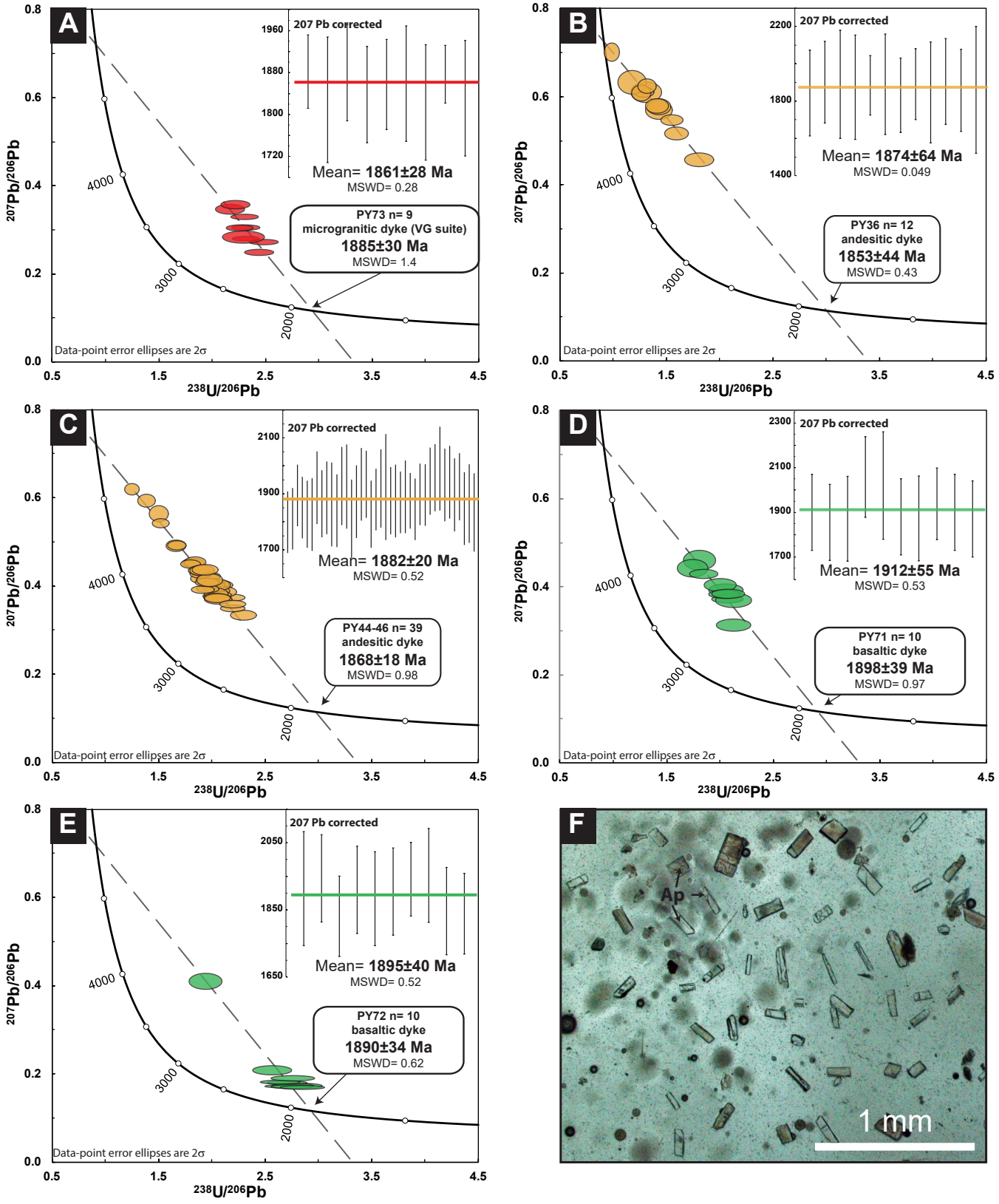
A
207 Pb corrected
Mean= 1861±28 Ma
MSWD= 0.28
PY73 n= 9
microgranitic dyke (VG suite)
1885±30 Ma
MSWD= 1.4
Data-point error ellipses are 2σ
B
207 Pb corrected
Mean= 1874±64 Ma
MSWD= 0.049
PY36 n= 12
andesitic dyke
1853±44 Ma
MSWD= 0.43
Data-point error ellipses are 2σ
C
207 Pb corrected
Mean= 1882±20 Ma
MSWD= 0.52
PY44-46 n= 39
andesitic dyke
1868±18 Ma
MSWD= 0.98
Data-point error ellipses are 2σ
D
207 Pb corrected
Mean= 1912±55 Ma
MSWD= 0.53
PY71 n= 10
basaltic dyke
1898±39 Ma
MSWD= 0.97
Data-point error ellipses are 2σ
E
207 Pb corrected
Mean= 1895±40 Ma
MSWD= 0.52
PY72 n= 10
basaltic dyke
1890±34 Ma
MSWD= 0.62
Data-point error ellipses are 2σ
F
Ap
1 mm
207Pb/206Pb
238U/206Pb
4000
3000
2000

Figure 4

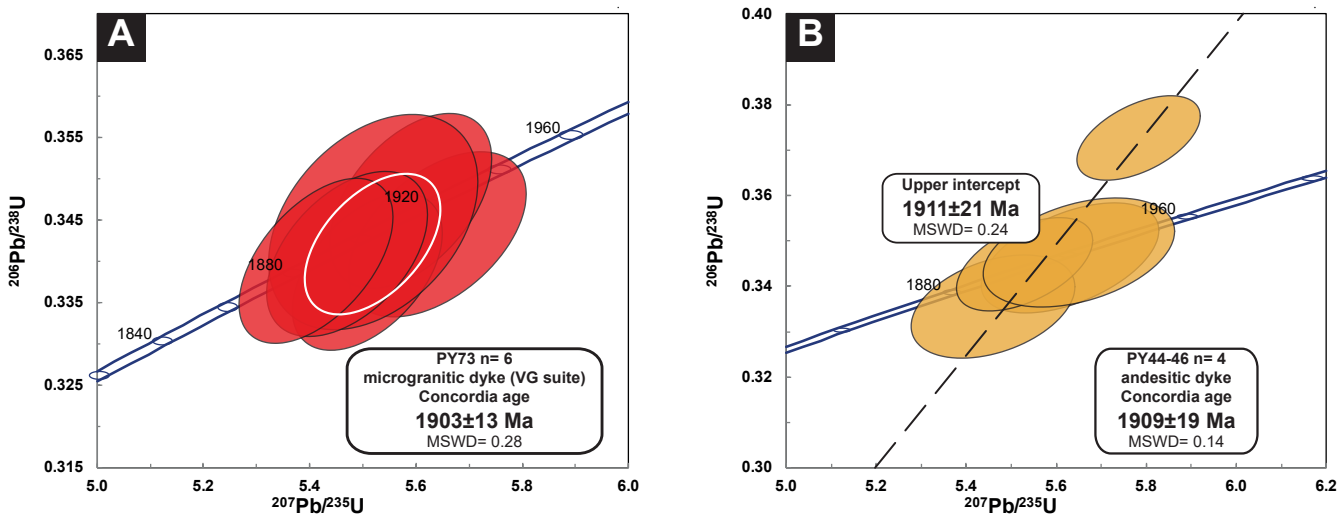
A
0.365
0.355
0.345
0.335
0.325
0.315
206Pb/238U
5.0
5.2
5.4
5.6
5.8
6.0
207Pb/235U
1960
1920
1880
1840
PY73 n= 6
microgranitic dyke (VG suite)
Concordia age
1903±13 Ma
MSWD= 0.28
B
0.40
0.38
0.36
0.34
0.32
0.30
206Pb/238U
5.0
5.2
5.4
5.6
5.8
6.0
6.2
207Pb/235U
Upper intercept
1911±21 Ma
MSWD= 0.24
1960
1880
PY44-46 n= 4
andesitic dyke
Concordia age
1909±19 Ma
MSWD= 0.14

Figure 5

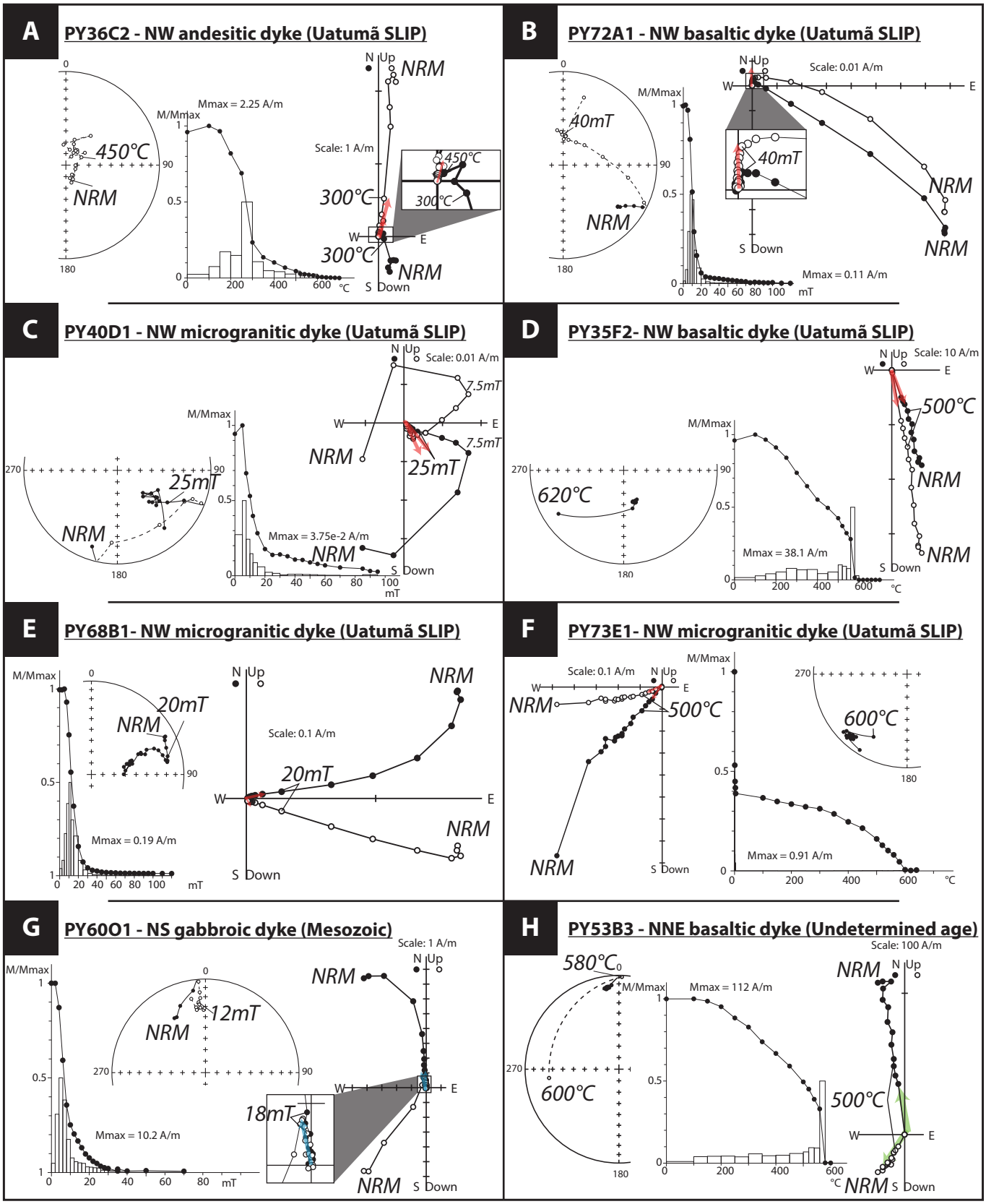
A
PY36C2 - NW andesitic dyke (Uatumã SLIP)
450°C
NRM
Mmax = 2.25 A/m
M/Mmax
Scale: 1 A/m
N Up
NRM
300°C
300°C
S Down
B
PY72A1 - NW basaltic dyke (Uatumã SLIP)
40mT
NRM
Scale: 0.01 A/m
N Up
W
E
40mT
NRM
NRM
S Down
Mmax = 0.11 A/m
mT
C
PY40D1 - NW microgranitic dyke (Uatumã SLIP)
25mT
NRM
Scale: 0.01 A/m
N Up
7.5mT
7.5mT
25mT
NRM
Mmax = 3.75e-2 A/m
NRM
S Down
mT
D
PY35F2- NW basaltic dyke (Uatumã SLIP)
620°C
Scale: 10 A/m
N Up
500°C
NRM
NRM
Mmax = 38.1 A/m
S Down
°C
E
PY68B1- NW microgranitic dyke (Uatumã SLIP)
20mT
NRM
Mmax = 0.19 A/m
mT
N Up
NRM
Scale: 0.1 A/m
20mT
NRM
S Down
F
PY73E1- NW microgranitic dyke (Uatumã SLIP)
Scale: 0.1 A/m
N Up
NRM
500°C
NRM
S Down
600°C
Mmax = 0.91 A/m
°C
G
PY60O1 - NS gabbroic dyke (Mesozoic)
Scale: 1 A/m
N Up
12mT
NRM
NRM
18mT
Mmax = 10.2 A/m
mT
NRM
S Down
H
PY53B3 - NNE basaltic dyke (Undetermined age)
Scale: 100 A/m
580°C
600°C
Mmax = 112 A/m
NRM
N Up
500°C
NRM
S Down
°C

Figure 6

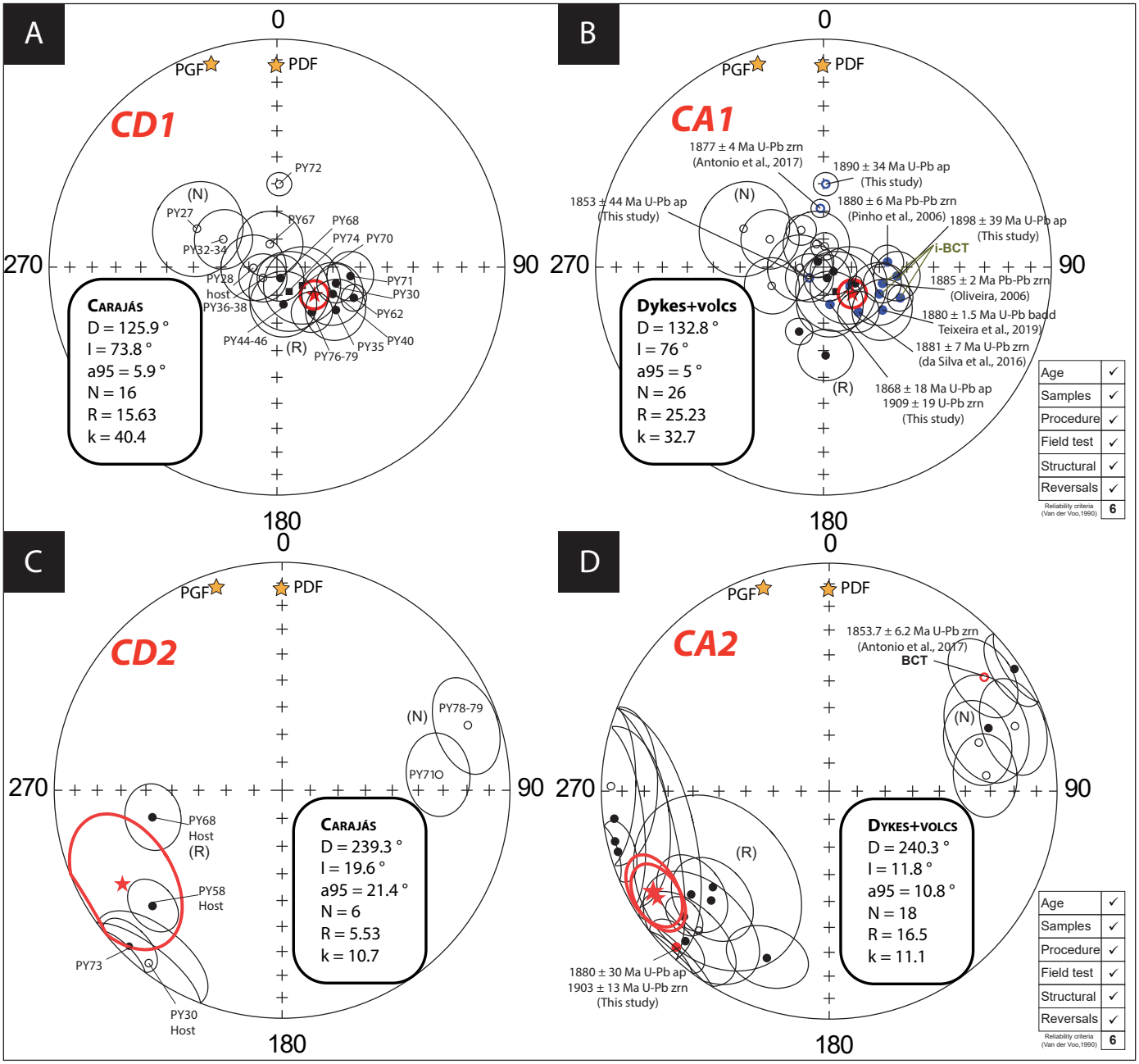
A
CD1
PGF
PDF
0
90
180
270
PY72
(N)
PY27
PY67
PY68
PY32-34
PY74
PY70
PY28
host
PY36-38
PY71
PY30
PY62
PY44-46
(R)
PY76-79
PY35
PY40
Carajás
D = 125.9 °
I = 73.8 °
a95 = 5.9 °
N = 16
R = 15.63
k = 40.4
B
CA1
1877 ± 4 Ma U-Pb zrn
(Antonio et al., 2017)
1890 ± 34 Ma U-Pb ap
(This study)
1853 ± 44 Ma U-Pb ap
(This study)
1880 ± 6 Ma Pb-Pb zrn
(Pinho et al., 2006)
1898 ± 39 Ma U-Pb ap
(This study)
I-BCT
1885 ± 2 Ma Pb-Pb zrn
(Oliveira, 2006)
1880 ± 1.5 Ma U-Pb badd
Teixeira et al., 2019)
1881 ± 7 Ma U-Pb zrn
(da Silva et al., 2016)
1868 ± 18 Ma U-Pb ap
1909 ± 19 U-Pb zrn
(This study)
Dykes+volcs
D = 132.8 °
I = 76 °
a95 = 5 °
N = 26
R = 25.23
k = 32.7
Age
Samples
Procedure
Field test
Structural
Reversals
Reliability criteria
(Van der Voo,1990)
6
C
CD2
PY78-79
PY71
PY68
Host
PY58
Host
PY73
PY30
Host
Carajás
D = 239.3 °
I = 19.6 °
a95 = 21.4 °
N = 6
R = 5.53
k = 10.7
D
CA2
1853.7 ± 6.2 Ma U-Pb zrn
(Antonio et al., 2017)
BCT
1880 ± 30 Ma U-Pb ap
1903 ± 13 Ma U-Pb zrn
(This study)
Dykes+volcs
D = 240.3 °
I = 11.8 °
a95 = 10.8 °
N = 18
R = 16.5
k = 11.1

Figure 7

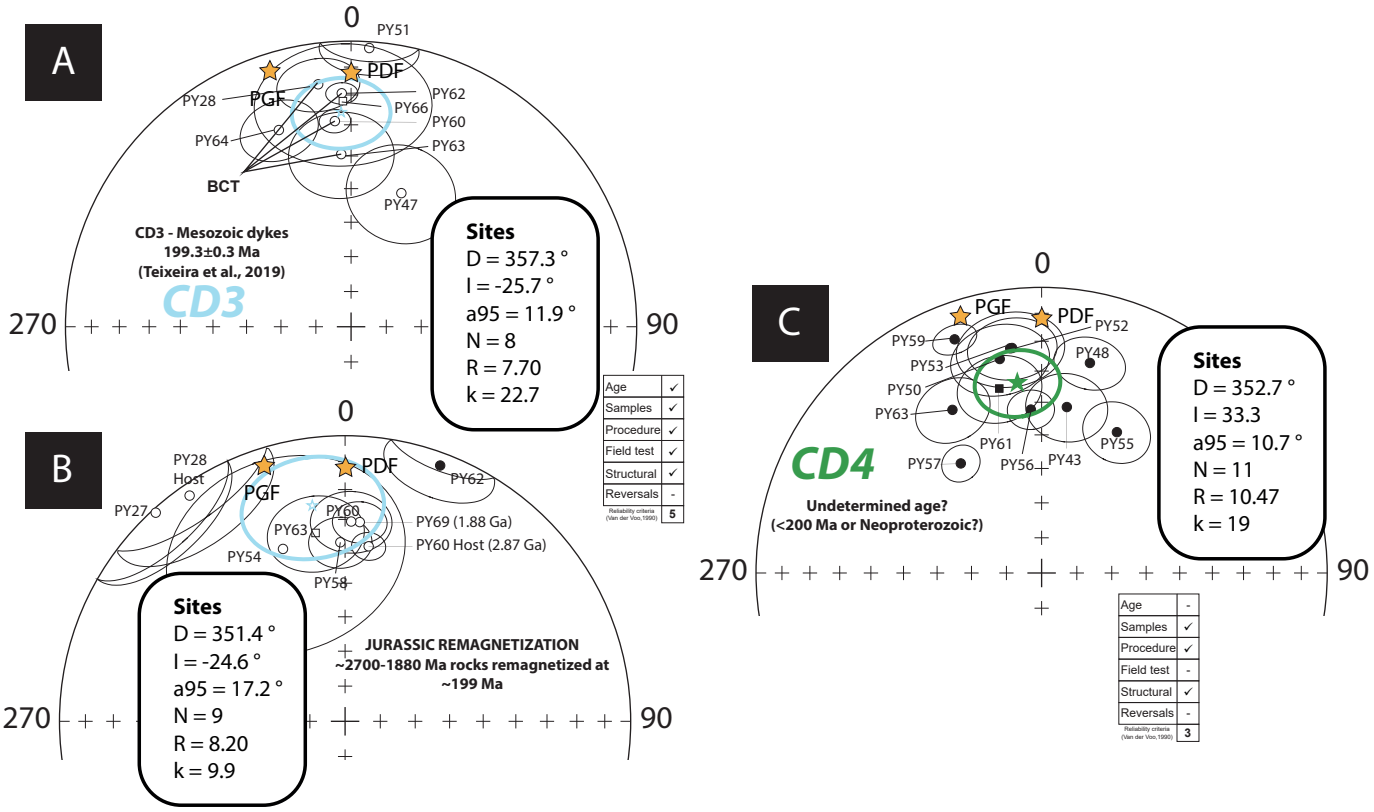
A
0
PY51
PDF
PGF
PY28
PY62
PY66
PY60
PY64
PY63
BCT
PY47
CD3 - Mesozoic dykes
199.3±0.3 Ma
(Teixeira et al., 2019)
CD3
270
90
Sites
D = 357.3 °
I = -25.7 °
a95 = 11.9 °
N = 8
R = 7.70
k = 22.7
Age ✓
Samples ✓
Procedure ✓
Field test ✓
Structural ✓
Reversals -
5
B
0
PY28
Host
PDF
PY62
PGF
PY27
PY60
PY63
PY69 (1.88 Ga)
PY60 Host (2.87 Ga)
PY54
PY58
Sites
D = 351.4 °
I = -24.6 °
a95 = 17.2 °
N = 9
R = 8.20
k = 9.9
JURASSIC REMAGNETIZATION
~2700-1880 Ma rocks remagnetized at
~199 Ma
270
90
C
0
PGF
PDF
PY52
PY59
PY48
PY53
PY50
PY63
PY61
PY55
CD4
PY57
PY56
PY43
Undetermined age?
(<200 Ma or Neoproterozoic?)
Sites
D = 352.7 °
I = 33.3
a95 = 10.7 °
N = 11
R = 10.47
k = 19
270
90
Age -
Samples ✓
Procedure ✓
Field test -
Structural ✓
Reversals -
3

Figure 8

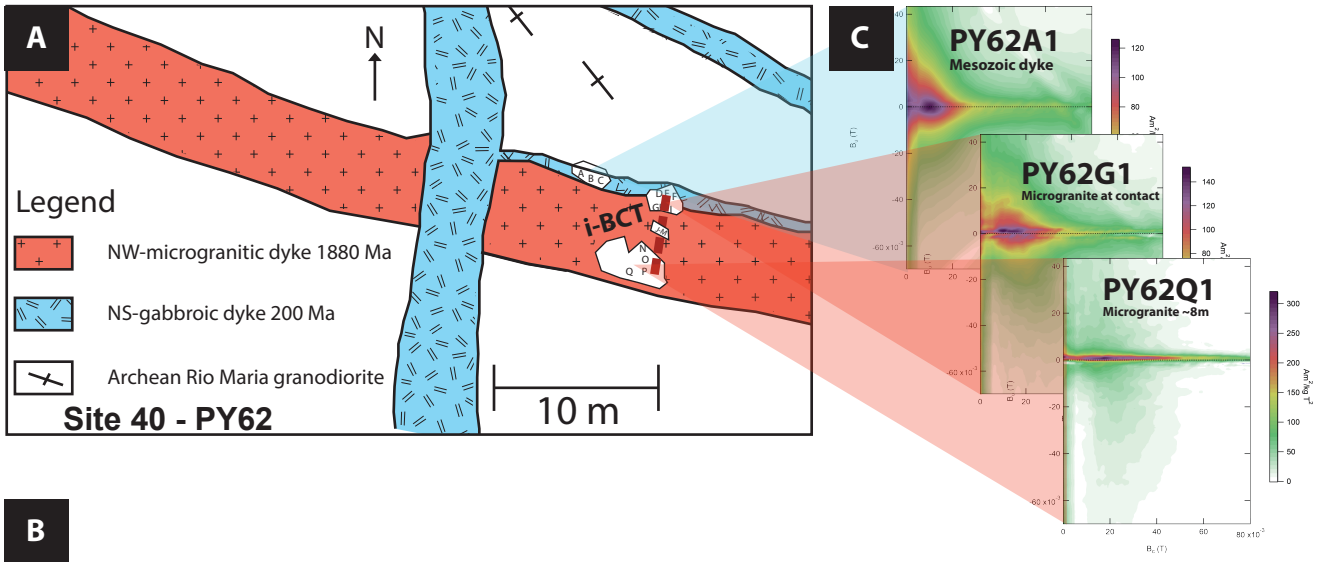

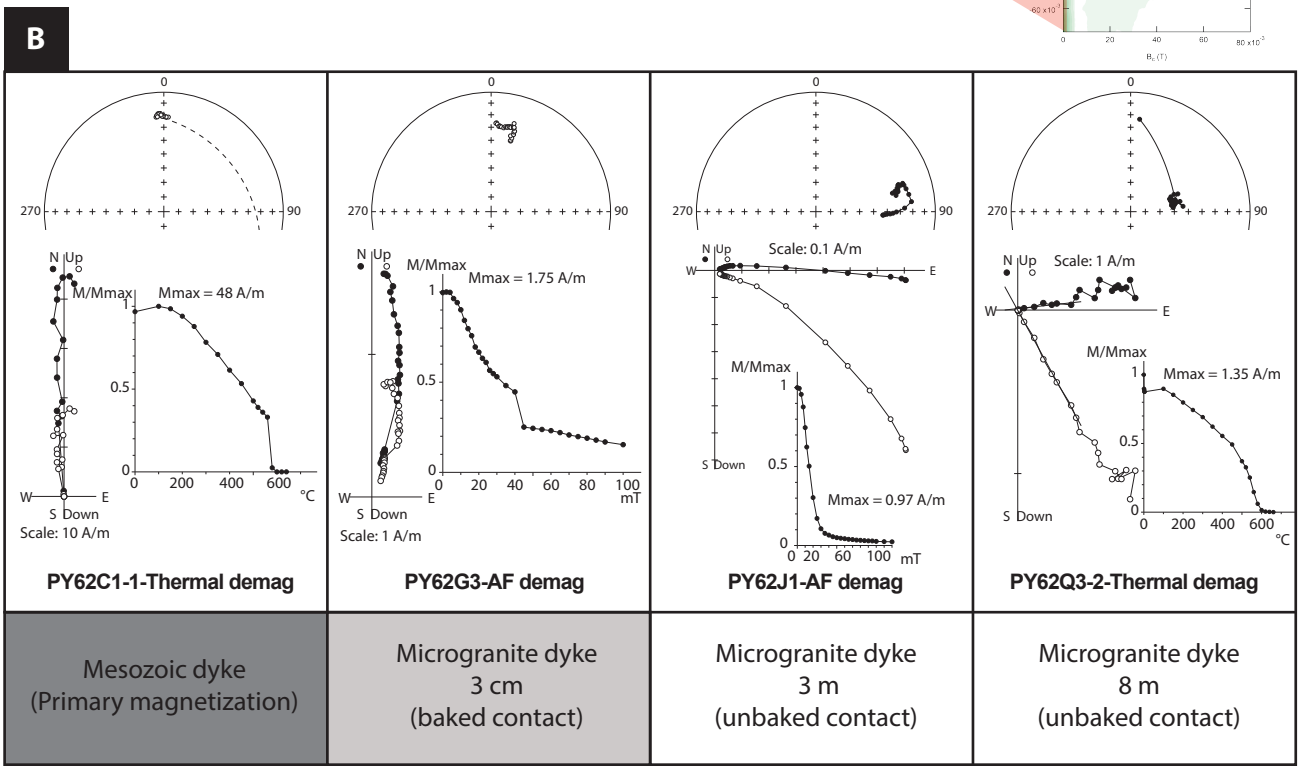

Mesozoic dyke (Primary magnetization)	Microgranite dyke 3 cm (baked contact)	Microgranite dyke 3 m (unbaked contact)	Microgranite dyke 8 m (unbaked contact)

Figure 9

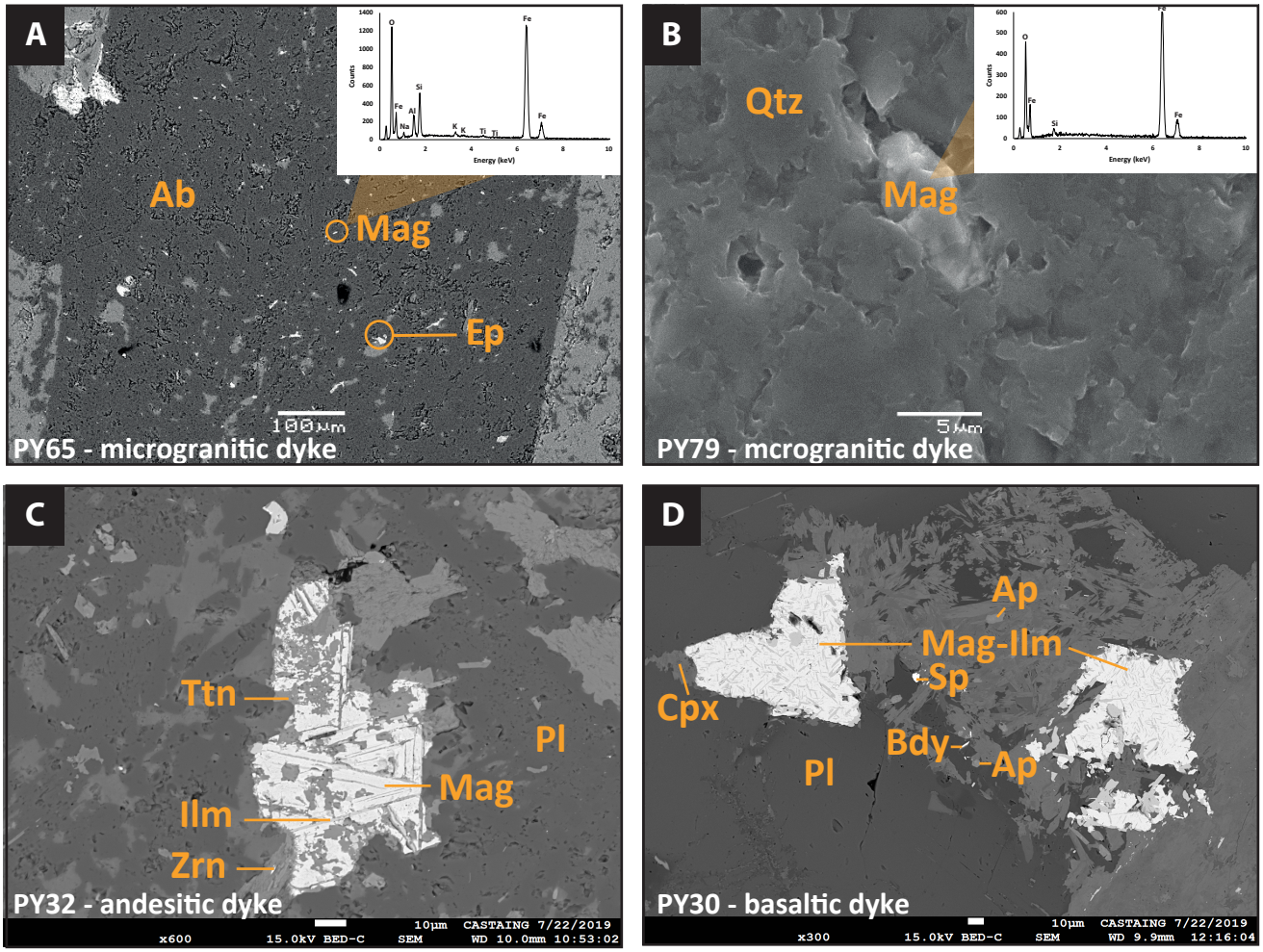
A
Ab
Mag
Ep
100µm
PY65 - microgranitic dyke
B
Qtz
Mag
5µm
PY79 - mcrogranitic dyke
C
Ttn
Pl
Mag
Ilm
Zrn
PY32 - andesitic dyke
x600 15.0kV BED-C SEM 10µm CASTAING 7/22/2019 WD 10.0mm 10:53:02
D
Ap
Mag-Ilm
Sp
Cpx
Bdy
Ap
Pl
PY30 - basaltic dyke
x300 15.0kV BED-C SEM 10µm CASTAING 7/22/2019 WD 9.9mm 12:16:04

Figure 10

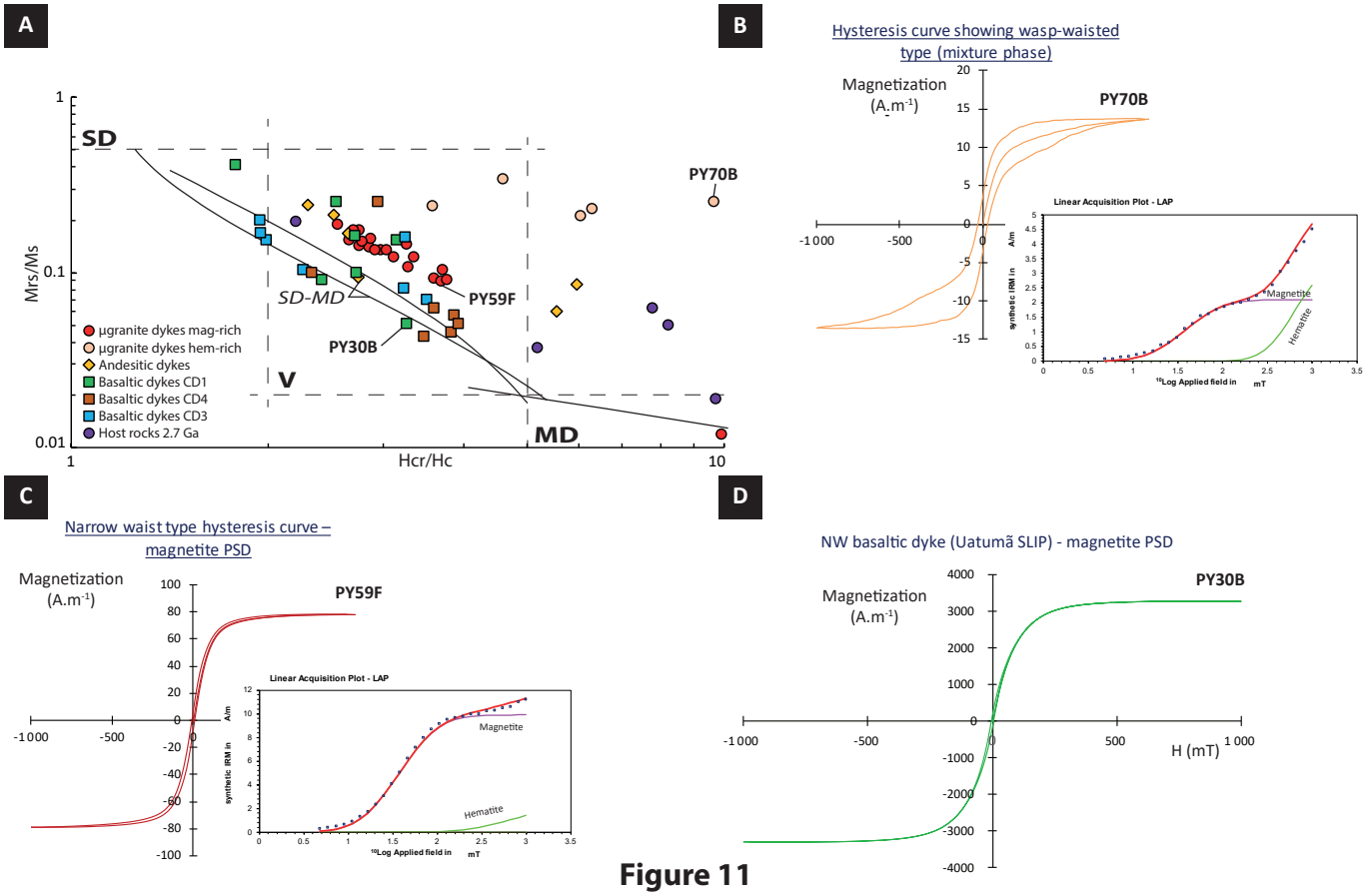
A
B
C
D
SD
SD-MD
V
MD
PY70B
PY59F
PY30B
Mrs/Ms
Hcr/Hc
µgranite dykes mag-rich
µgranite dykes hem-rich
Andesitic dykes
Basaltic dykes CD1
Basaltic dykes CD4
Basaltic dykes CD3
Host rocks 2.7 Ga
Hysteresis curve showing wasp-waisted type (mixture phase)
Magnetization (A.m-1)
Linear Acquisition Plot - LAP
Magnetite
Hematite
Narrow waist type hysteresis curve – magnetite PSD
NW basaltic dyke (Uatumã SLIP) - magnetite PSD
H (mT)

Figure 11

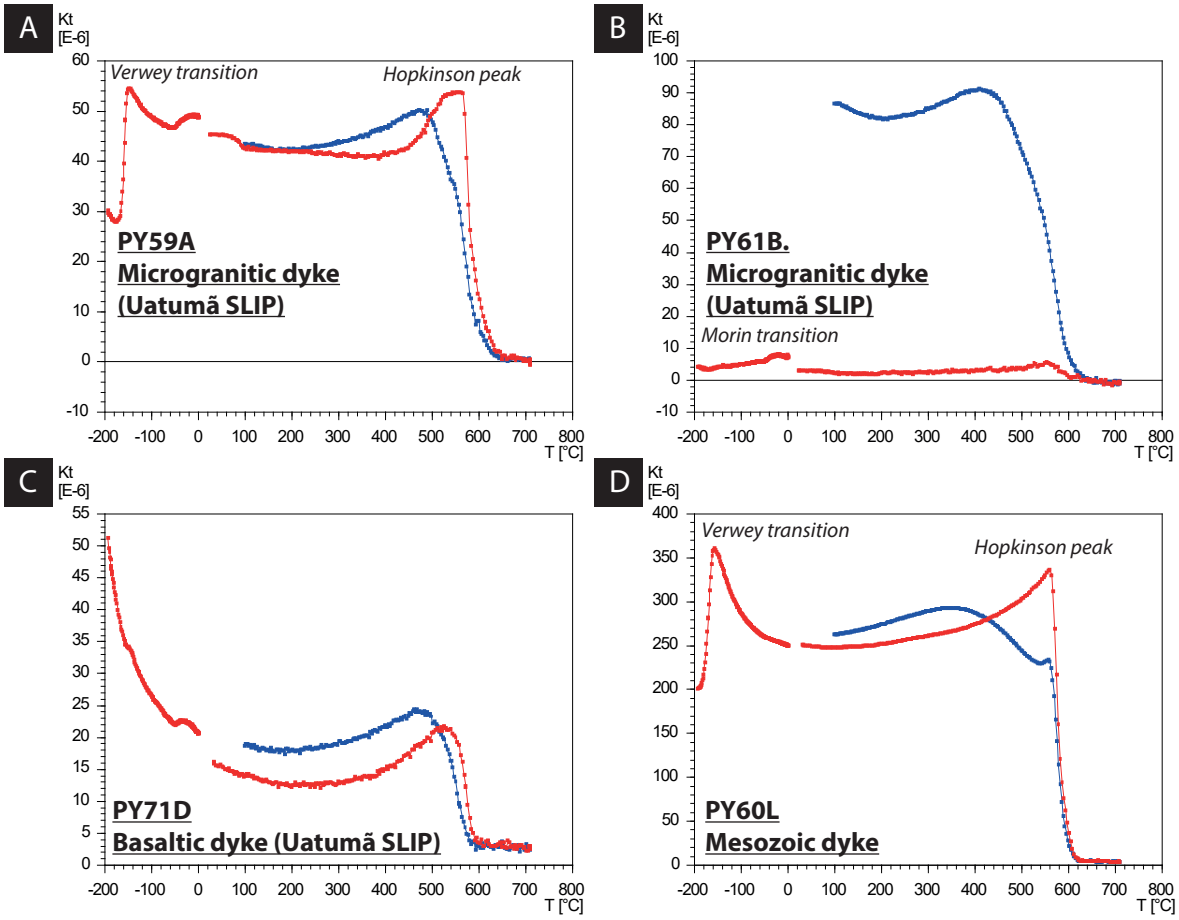
A
Kt
[E-6]
Verwey transition
Hopkinson peak
PY59A
Micrograniticdyke
(Uatumã SLIP)
T [°C]
B
Kt
[E-6]
PY61B.
Micrograniticdyke
(Uatumã SLIP)
Morin transition
T [°C]
C
Kt
[E-6]
PY71D
Basaltic dyke (Uatumã SLIP)
T [°C]
D
Kt
[E-6]
Verwey transition
Hopkinson peak
PY60L
Mesozoic dyke
T [°C]

Figure 12

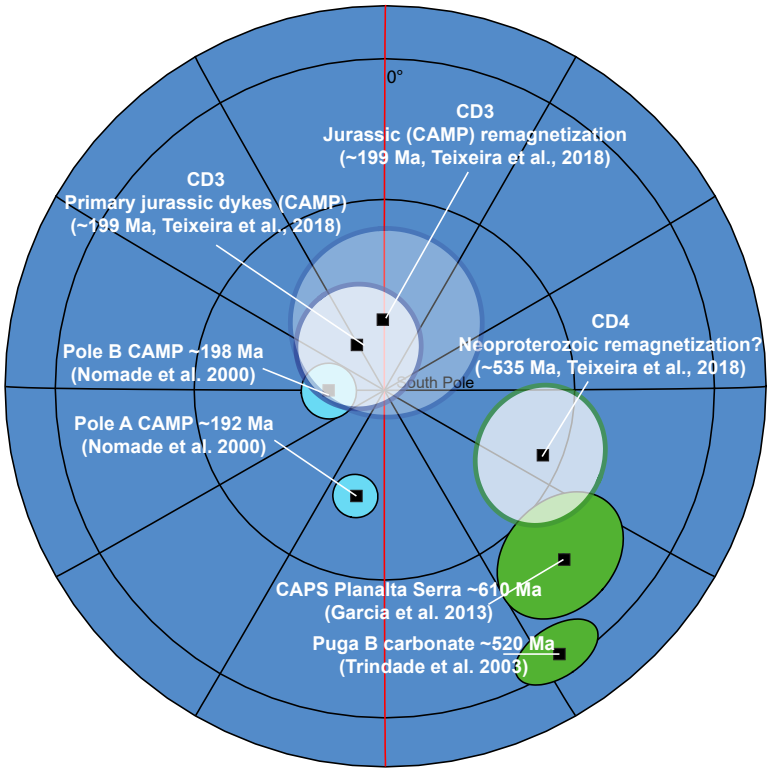
0°
CD3
Jurassic (CAMP) remagnetization
(~199 Ma, Teixeira et al., 2018)
CD3
Primary jurassic dykes (CAMP)
(~199 Ma, Teixeira et al., 2018)
CD4
Neoproterozoic remagnetization?
(~535 Ma, Teixeira et al., 2018)
Pole B CAMP ~198 Ma
(Nomade et al. 2000)
South Pole
Pole A CAMP ~192 Ma
(Nomade et al. 2000)
CAPS Planalta Serra ~610 Ma
(Garcia et al. 2013)
Puga B carbonate ~520 Ma
(Trindade et al. 2003)

Figure 13

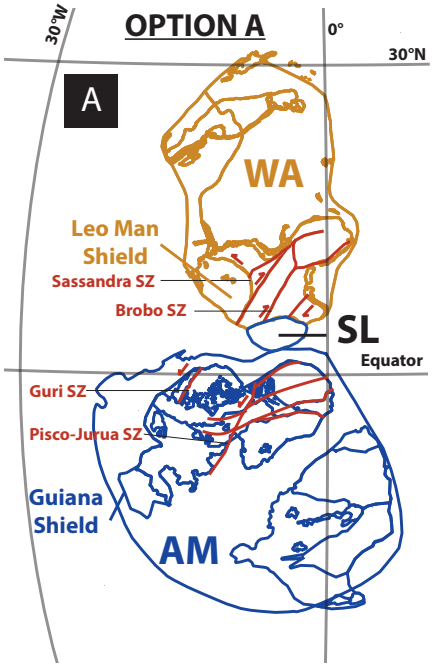

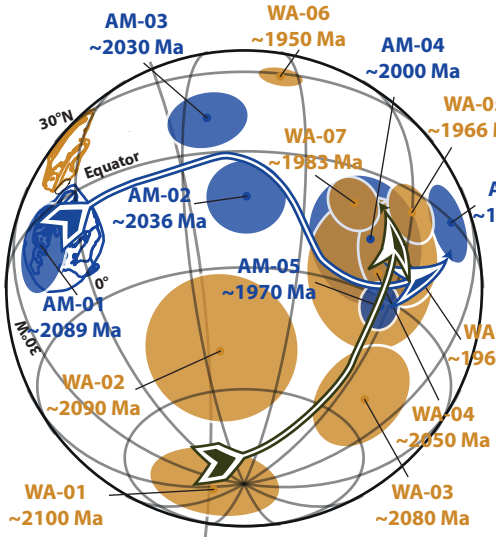

~2100-1960 Ma
APW paths for option A

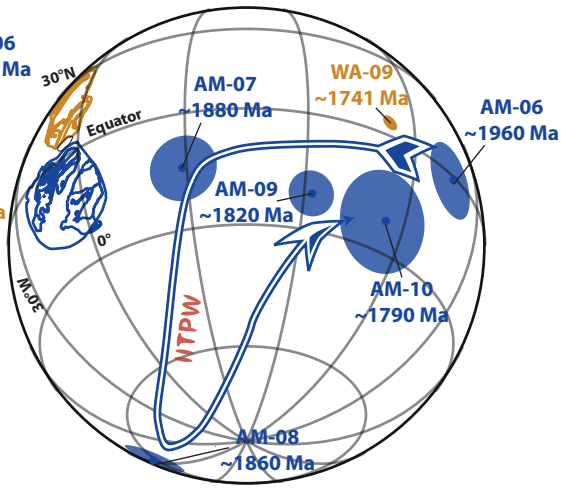

~1960-1790 Ma
APW paths for option A

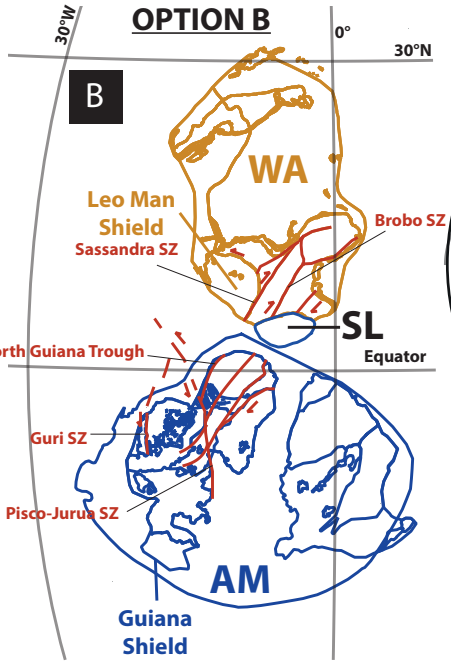

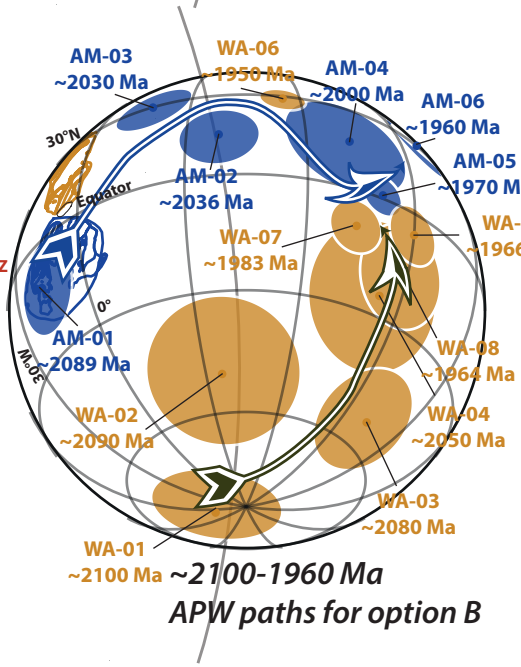

~2100-1960 Ma
APW paths for option B

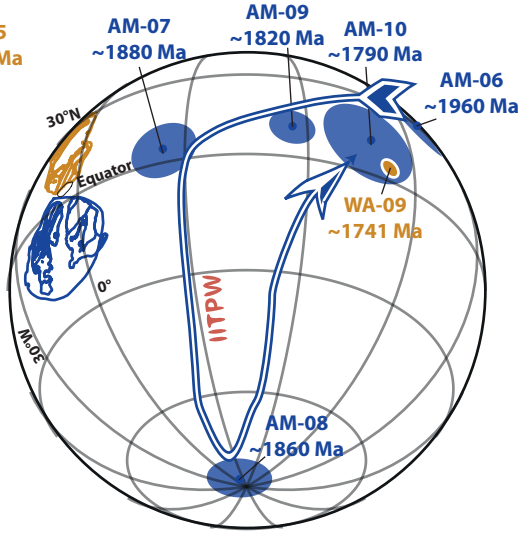

~1960-1790 Ma
APW paths for option B

Figure 14

Sample	U (ppm)	Pb (ppm)	$^{238}U/^{206}Pb$	Error (2σ)	$^{207}Pb/^{206}Pb$	Error (2σ)	Final ^{207}Age	Error (2σ)
PY36 andesitic dyke (Forced intercept at 0.990 - 1853 ± 44 Ma U-Pb ap)								
ApatBatch25a_14	1.1	3.9	1.314	8.9	0.6100	3.1	1843	230
ApatBatch25a_15	1.0	2.9	1.432	7.2	0.5690	3.0	1901	220
ApatBatch25a_16	1.9	7.0	1.288	6.0	0.6100	1.5	1890	290
ApatBatch25a_18	1.1	3.2	1.428	6.4	0.5770	2.6	1874	280
ApatBatch25a_23	1.7	5.2	1.808	6.2	0.4570	2.8	1884	160
ApatBatch25a_24	0.9	3.5	1.179	9.0	0.6330	3.5	1890	270
ApatBatch25a_26	1.5	4.8	1.551	5.5	0.5470	1.8	1831	200
ApatBatch25a_27	0.8	3.0	1.264	5.9	0.6080	2.5	1891	190
ApatBatch25a_28	0.8	2.9	1.318	5.5	0.6240	2.2	1846	270
ApatBatch25a_29	1.2	3.6	1.593	5.7	0.5170	2.3	1905	230
ApatBatch25a_32	0.9	2.7	1.413	6.2	0.5790	2.4	1858	220
ApatBatch25a_33	1.0	4.7	0.988	5.9	0.7010	2.4	1860	340
PY44-46 andesitic dyke (Forced intercept at 0.990 - 1868 ± 18 Ma U-Pb ap)								
Apat250618b_1	3.3	4.2	2.193	4.4	0.3735	1.7	1799	110
Apat250618b_2	3.0	4.2	2.082	4.5	0.4025	2.1	1811	110
Apat250618b_3	2.9	4.9	1.826	4.7	0.4518	2.0	1894	110
Apat250618b_4	2.7	4.0	1.969	4.7	0.4212	1.9	1851	110
Apat250618b_5	2.7	3.6	2.113	4.6	0.3860	2.6	1827	120
Apat250618b_6	3.1	4.2	2.05	4.5	0.4036	1.9	1826	130
Apat250618b_7	2.2	4.4	1.661	4.6	0.4910	2.2	1922	130
Apat250618b_8	3.4	5.1	2.008	4.6	0.4070	2.0	1864	120
Apat250618b_9	2.5	3.6	2.022	4.4	0.3948	2.2	1886	130
Apat250618b_10	2.4	4.0	1.843	4.6	0.4540	2.2	1862	150
Apat250618b_11	2.1	5.5	1.389	4.9	0.5930	2.0	1840	130
Apat250618b_12	2.5	4.2	1.801	4.3	0.4487	1.7	1928	140
Apat250618b_13	2.1	4.0	1.672	4.3	0.4913	1.8	1926	150
Apat250618b_14	1.8	4.4	1.503	4.8	0.5640	2.7	1811	140
Apat250618b_15	2.7	3.9	2.017	4.4	0.4008	2.0	1872	130
Apat250618b_16	2.6	4.0	1.905	4.4	0.4165	2.1	1934	130
Apat250618b_17	2.8	3.9	2.027	4.4	0.3767	1.9	1934	120
Apat250618b_18	4.0	4.9	2.297	4.3	0.3339	2.8	1827	120
Apat250618b_20	2.8	3.9	1.965	4.4	0.4150	2.9	1879	110
Apat250618b_21	2.6	3.9	1.894	4.3	0.4270	2.0	1919	140
Apat250618b_22	1.7	5.0	1.248	4.4	0.6190	1.8	1924	190
Apat250618b_23	2.8	4.3	1.88	4.5	0.4347	1.8	1876	120
Apat250618b_24	2.6	4.2	1.908	4.9	0.4352	2.3	1874	130
Apat250618b_25	3.1	4.2	2.056	4.3	0.3888	2.1	1869	110
Apat250618b_26	2.7	6.1	1.519	4.4	0.5421	1.7	1889	130
Apat250618b_27	3.6	4.5	2.195	4.3	0.3490	1.9	1875	100
Apat250618b_29	2.9	4.2	2.04	5.3	0.4020	2.7	1845	110
Apat250618b_30	2.9	3.9	2.071	4.5	0.3790	1.9	1898	110
Apat250618b_32	2.8	3.7	2.04	4.5	0.3820	2.6	1896	110
Apat250618b_33	2.8	4.0	1.964	4.3	0.3937	1.8	1945	120
Apat250618b_34	3.1	4.2	2.029	4.4	0.3743	2.0	1958	120

Apat250618c_1	2.9	4.1	1.917	4.6	0.3915	1.9	1990	150
Apat250618c_2	3.3	4.4	2.051	4.7	0.3711	1.7	1932	130
Apat250618c_4	3.2	4.3	2.06	5.1	0.3690	2.5	1941	130
Apat250618c_5	2.6	3.8	1.954	4.7	0.4073	1.9	1896	130
Apat250618c_6	3.0	4.0	2.052	4.9	0.3728	2.2	1925	120
Apat250618c_10	3.6	4.7	2.197	4.6	0.3587	1.9	1847	130
Apat250618c_11	2.8	4.2	1.98	5.1	0.4130	2.9	1865	140
Apat250618c_12	2.8	4.4	1.937	5.0	0.4361	2.3	1833	140
PY71 basaltic dyke (Forced intercept at 0.990 - 1898 ± 39 Ma U-Pb ap)								
Apat260618a_1	3.0	4.3	2.074	5.8	0.3721	1.9	1900	170
Apat260618a_2	3.3	4.8	2.059	6.4	0.3930	2.8	1855	170
Apat260618a_3	2.5	4.4	1.809	6.8	0.4600	3.9	1872	190
Apat260618a_4	1.0	1.1	2.129	6.1	0.3130	3.5	2058	180
Apat260618a_5	1.3	2.1	1.747	6.7	0.4420	3.6	2020	240
Apat260618a_6	3.1	4.5	2.005	6.2	0.4030	3.0	1880	170
Apat260618a_7	3.6	4.8	2.127	6.5	0.3690	3.5	1873	190
Apat260618a_9	2.4	3.7	1.849	5.9	0.4292	2.0	1938	160
Apat260618a_10	3.3	4.3	2.042	5.9	0.3832	1.9	1900	170
Apat260618a_11	3.2	4.2	2.079	6.0	0.3837	2.4	1871	170
PY72 basaltic dyke (Forced intercept at 0.990 - 1890 ± 34 Ma U-Pb ap)								
Apat260618a_14	2.9	4.3	1.939	6.5	0.4090	3.7	1913	170
Apat260618a_16	8.3	11.1	2.679	5.6	0.1716	1.6	1944	130
Apat260618a_17	7.5	9.6	2.833	5.9	0.1726	2.8	1831	120
Apat260618a_18	6.7	9.5	2.706	5.7	0.1790	1.8	1910	130
Apat260618a_19	6.5	8.1	2.76	5.8	0.1728	2.9	1883	140
Apat260618a_20	7.1	9.2	2.746	5.7	0.1709	1.9	1905	130
Apat260618a_21	6.8	9.8	2.564	5.9	0.2085	4.1	1941	110
Apat260618a_22	5.7	7.4	2.642	5.8	0.1813	2.2	1953	140
Apat260618a_23	7.1	9.6	2.763	6.1	0.1900	2.5	1847	130
Apat260618a_24	10.0	13.9	2.85	6.0	0.1687	2.1	1839	120
PY73 microgranitic Velho Guilherme dyke (Forced intercept at 0.990 - 1885 ± 30 Ma)								
Apat250618c_13	7.6	10.8	2.168	5.1	0.3470	2.7	1882	70
Apat250618c_14	6.2	8.1	2.216	5.1	0.3565	2.2	1828	120
Apat250618c_15	11.3	23.4	2.317	4.6	0.3058	1.6	1880	92
Apat250618c_16	15.5	32.3	2.484	4.5	0.2723	1.7	1838	92
Apat250618c_18	14.4	30.7	2.443	4.6	0.2484	2.1	1857	86
Apat250618c_19	7.3	9.4	2.317	4.4	0.2799	1.5	1859	110
Apat250618c_20	7.2	12.8	2.26	4.5	0.3045	1.8	1823	110
Apat250618c_21	6.8	9.3	2.292	7.1	0.2830	3.9	1877	55
Apat250618c_25	6.8	8.9	2.306	4.6	0.3290	1.6	1831	110

Table 1 : LA-ICP-MS apatite dating results

Sample	¦206 (%)	U (mg.g^{-1})	2s	Th (mg.g^{-1})	2s	Pb (mg.g^{-1})	2s	Th/U	$^{206}Pb/^{204}Pb$	Measured ratios $^{207}Pb/^{235}U$	1s	1s %	$^{206}Pb/^{238}U$	1s	1s %	Rho	Ages (Ma) $^{207}Pb/^{206}Pb$	2s	$^{206}Pb/^{238}U$	2s	$^{207}Pb/^{235}U$	2s	% conc[2]
Microgranitic Velho Guilherme dyke																							
ELD73_4	0.14	70	2	52	1	55	2	0.74	13060	5.640	0.110	2.0	0.3433	0.0066	1.9	0.49	1922	21	1892	31	1914	16	98
ELD73_7	0.15	70	3	66	2	69	3	0.95	12420	5.590	0.100	1.8	0.3473	0.0070	2.0	0.48	1885	22	1919	33	1915	15	102
ELD73_11	0.11	98	4	90	4	92	5	0.92	16650	5.509	0.093	1.7	0.3388	0.0063	1.9	0.49	1901	19	1876	30	1898	15	99
ELD73_13	0.14	79	3	76	2	79	4	0.96	13210	5.520	0.130	2.4	0.3448	0.0086	2.5	0.37	1922	28	1904	41	1902	19	99
ELD73_15	0.09	129	8	120	7	115	8	0.93	21450	5.470	0.100	1.8	0.3409	0.0066	1.9	0.47	1905	20	1888	32	1896	16	99
ELD73_17	0.08	146	7	130	7	123	7	0.89	24200	5.412	0.096	1.8	0.3401	0.0066	1.9	0.53	1921	18	1880	32	1882	15	98
Andesitic dyke																							
ELD46_2	0.05	191	12	92	6	82	5	0.48	39450	5.783	0.090	1.6	0.3727	0.0061	1.6	0.52	1883	15	2038	29	1938	13	108
ELD46_3	0.25	38	1	33	2	35	2	0.86	7385	5.630	0.130	2.3	0.3463	0.0080	2.3	0.50	1931	24	1912	38	1909	20	99
ELD46_4	0.17	57	3	70	4	67	4	1.23	11200	5.460	0.120	2.2	0.3356	0.0075	2.2	0.38	1941	26	1861	36	1883	19	96
ELD46_5	0.08	116	5	145	5	144	6	1.25	23450	5.530	0.100	1.8	0.3448	0.0068	2.0	0.51	1899	20	1905	32	1906	16	100
ELD46_6	0.27	37	2	35	1	38	2	0.95	7025	5.650	0.140	2.5	0.3475	0.0079	2.3	0.39	1958	26	1918	37	1919	21	98

Table 2 : LA-ICP-MS zircon dating results

Site	Sample	Lithology	S.Lat	S.Long	Characteristic remanent magnetization (ChRM)						VGP	
					n/N	Dec (°)	Inc (°)	R	k	α95 (°)	P. Lat (°N)	P. Long (°E)
CD1												
Normal polarity												
12*	PY25-26	*NW - Microgranitic dyke*	-7.45	-49.87	8/11	92.2	-67.5	7.78	32.5	9.9	-3.8	271.1
17*	PY31	*NW- Andesitic dyke*	-7.4	-50.14	7/7	298.6	-38.5	6.66	17.4	15	-28	16.7
18	PY32-33-34	*NW- Andesitic dyke*	-7.4	-50.14	9/12	297.4	-68.4	8.72	28.8	10.5	-22.6	346.6
20	PY36-37-38	*NW- Andesitic dyke*	-7.4	-50.14	8/15	232.5	-83.7	7.84	42.9	8.6	0.3	319.8
13	PY27 A-E	*NW - Basaltic dyke*	-7.44	-50.02	6/9	295.6	-58.1	5.73	18.6	16.5	-24.5	0.6
14	PY28 F-L	*Archean basement*	-7.43	-50.03	6/10	268.3	-81.6	5.88	42	11.7	-6.6	326.6
17*	PY31 A-C - H	*Archean basement*	-7.4	-50.14	3/5	289.1	-29.8	2.9	20.8	27.8	-20.3	25.5
45	PY67 A-G	*NW - Microgranitic dyke*	-6.8	308.66	7/12	342.7	-81.4	6.8	29.5	11.9	22.8	134.1
50	PY72 A-F	*NW - Basaltic dyke*	-6.82	308.6	12/14	1.6	-60.2	11.9	106	4.3	55.6	126.5
MEAN CD1 (N)					***6***	***312.2***	***-75.6***	***5.8***	***24.9***	***13.7***		
								R=5.47	***K=9.5***	***A95=22.9***	***22.8***	***150.1***
Reversed polarity												
22	PY40	*NW - Microgranitic dyke*	-7.41	-50.21	6/8	115.7	67.8	*5.9*	*52.2*	11.1	-21.8	347.7
24	PY44-45-46	*NW- Andesitic dyke*	-7.52	-50.05	8/19	170.1	76.5	7.7	23	11.8	-32.7	315
15*	PY29 A-G	*NW - Basaltic dyke*	-7.52	-50.02	4/10	71.7	55.3	3.63	8.1	34.4	10.1	1.4
16	PY30 A-D/I-L	*NW - Basaltic dyke*	-7.76	-50.05	9/12	105.4	68.1	8.88	66.4	6.9	-15.7	348.8
19	PY35 A-H	*NW - Basaltic dyke*	-7.38	-50.13	6/12	126	63.8	5.88	40.8	10.8	-30	350.9
21*	PY39	*NW- Andesitic dyke*	-7.38	-50.13	6/8	235.9	**57.3**	5.95	108.6	7.7	-31.2	260.1
22*	PY40 F-G - PY41-42	*Archean basement*	-7.41	-50.21	4/5	107.4	81.6	3.76	12.3	28.8	-12	325.8
40	PY62 J-Q	*NW - Microgranitic dyke*	-6.76	308.56	10/24	111.8	60.3	9.93	122.4	4.6	-20.8	356.9
46	PY68 A-F	*NW - Microgranitic dyke*	-6.8	308.66	9/12	162.2	85.9	8.81	42	8.3	-14.6	311.3
48	PY70 A-G	*NW - Microgranitic dyke*	-6.8	308.66	10/13	126.1	78.8	10.77	G.C	13.8	-19	327
52	PY74 A-G	*NW - Microgranitic dyke*	-6.86	308.62	5/11	153.5	80.3	3.39	G.C	14.3	-23.6	317.7
54	PY78 - 79	*NW - Microgranitic dyke*	-6.96	308.75	9/15	142.1	69.7	8.85	54.8	7.3	-34.3	335.1
49	PY71 A-G	*NW - Basaltic dyke*	-6.77	308.66	9/12	97	63.4	8.8	40.5	8.5	-9.7	354.2
MEAN CD1 (R)					***10***	***122.9***	***72.6***	***9.84***	***55.5***	***6.5***		
								R=9.55	***K=20.1***	***A95=11.1***	***-23.1***	***336.7***
MEAN POLE CD1 DYKE (N+R)					***16***	***125.9***	***73.8***	***15.63***	***40.4***	***5.9***		
								R=15.01	***K=15.2***	***A95=9.8***	***-23***	***334.3***
CD2												
Normal polarity												
49	PY71 A-G	*NW - Basaltic dyke*	-6.77	308.66	7/12	*84.1*	*-31.3*	*6.7*	*22.5*	*13*	*7*	*55.3*
54	PY78 - 79	*NW - Microgranitic dyke*	-6.96	308.75	5/15	70.7	-14.7	4.88	34.7	14.1	19.9	44.2
Reversed polarity												
51	PY73 A-H	*NW - Microgranitic dyke*	-6.84	308.58	10/13	224.5	4.7	9.7	30.5	8.9	-45.4	215
16	PY30 E-H	*Archean basement*	-7.76	-50.05	7/7	217.7	-4.7	6.54	13.1	17.3	-51	206.4

36	PY58 G-K	*Archean host*	-6.76	308.56	9/11	228.3	24.8	8.76	34	9	-42.1	230
46	PY68 G-K	*Archean host*	-6.8	308.66	7/7	258.2	41.5	6.81	31.7	10.9	-13.5	241.7
MEAN POLE CD2 DYKE (N+R)					***6***	***239.3***	***19.6***	***5.53***	***10.7***	***21.4***		
								R=5.65	***K=14.6***	***A95=18.2***	***-30.4***	***227***

CD3 – Jurassic component

Primary dyke

14	PY28 A-E	*NNE - Basaltic dyke*	-7.43	-50.03	7/11	*352.3*	*-15.4*	*6.87*	*45.4*	*9.5*	*82.4*	*216.2*
25	PY47 A-C	*NW - Basaltic dyke*	-7.43	-50.04	4/7	*20.6*	*-48.6*	*3.94*	*52.9*	*14.8*	*60.6*	*91.5*
29	PY51 A-M	*NNE - Basaltic dyke*	-6.9	-49.65	8/13	*3.7*	*-2.5*	*7.8*	*35.2*	*10.3*	*83.3*	*343.7*
40	PY62 A-F	*NS - Gabbro dyke*	-6.76	308.56	8/8	357.7	-19.3	7.97	244.9	3.7	86.1	164.4
42	PY64 A-H	*NW - Basaltic dyke*	-6.8	308.63	6/8	339.8	-27.5	5.93	67	9.8	68.7	195.5
44	PY66 A-G	*NW - Basaltic dyke*	-6.8	308.64	4/5	357.9	-22	4.58	G.C	21	-3.4	213.8
38	PY60 I-Q	*NS - Gabbro dyke*	-6.76	308.56	14/15	355.5	-28.6	13.89	112.9	3.9	80.5	155.8
41	PY63 A-G	*NS - Gabbro dyke*	-6.76	308.56	8/8	356.7	-39.3	*7.68*	*21.6*	13.6	74.2	139.9
MEAN POLE CD3 ONLY PRIMARY DYKE					***8***	***357.3***	***-25.7***	***7.7***	***22.7***	***11.9***		
								R=7.8	***K=35***	***A95=9.5***	***82.3***	***145.6***
											-82.3	***325.6***

Remagnetized sites

CD3

32	PY54 A-H	*NNE - Basaltic dyke*	-6.92	-50.26	4/4	*356.7*	*-35.9*	*3.88*	*24.9*	*21.7*	*76.6*	*143.2*
27	PY49 A-F	*NW - Basaltic dyke*	-6.84	-50.19	5/11	*317.8*	*-1.5*	*5.66*	*14.8*	*18*	*47.5*	*226.1*
38	PY60 A-H	*NW - Basaltic dyke*	-6.76	308.56	6/7	1.8	-30.7	5.92	62.8	10.1	80.1	118.5
36	PY58 A-F	*NW - Microgranitic dyke*	-6.76	308.56	6/14	358.5	-37.4	5.94	97.4	8.1	75.8	134.3
40	PY62 G-F	*NW - Microgranitic dyke*	-6.76	308.56	5/6	20.4	-5	4.9	40.6	12.2	-67.6	194.7
41	PY63 H-J	*NW - Microgranitic dyke*	-6.76	308.56	4/6	351.1	-33.7	1.41	G.C	12.2	75.5	164.4
47	PY69 A-H	*NW - Microgranitic dyke*	-6.81	308.68	6/12	4.2	-30.7	5.95	107.6	6.8	79.4	106.2
14	PY28 F-L	*Archean basement*	-7.43	-50.03	3/10	325.4	-4.5	2.95	42.2	19.2	*55.2*	*226.7*
38	PY60 R-Z	*Archean host*	-6.76	308.56	7/9	7.7	-38.2	6.97	219.5	4.4	73.5	102.5
MEAN POLE CD3 REMAGNETIZATION					***9***	***351.4***	***-24.6***	***8.2***	***9.9***	***17.2***		
								R=8.4	***K=13.3***	***A95=14.6***	***79.8***	***179.4***
											-79.8	***359.4***

CD4 - Younger undetermined component (or Neoproterozoic?)

23	PY43 A-D	*NW - Basaltic dyke*	-7.38	-50.13	6/7	*8.6*	*40.9*	*5.89*	*46.5*	*10.6*	*58.1*	*324.9*
26	PY48 A-F	*NNE - Basaltic dyke*	-6.86	-50.19	8/9	*12.9*	*25.6*	*7.84*	*43.9*	*8.7*	*65.9*	*342.2*
28	PY50 A-F	*NNE - Basaltic dyke*	-6.84	-50.19	8/10	*348.9*	*24.7*	*7.71*	*24.4*	*11.9*	*67.4*	*280.6*
30	PY52 A-H	*NNE - Basaltic dyke*	-6.91	-49.66	8/12	*352.5*	*21.6*	*7.76*	*29.3*	*10.6*	*70.4*	*287.8*
31	PY53 A-H	*NW - Basaltic dyke*	-6.91	-50.26	5/5	*352*	*21.7*	*4.9*	*41.8*	*12.8*	*70.2*	*286*
35	PY57 A-D	*NW - Basaltic dyke*	-6.73	308.51	4/6	323.6	50.6	3.99	298.4	5.3	38.5	268.1
33	PY55 A-E	*NW - Microgranitic dyke*	-6.75	308.5	9/12	28.1	43.4	10.63	27.1	9.1	47.8	347.9
34	PY56 A-H	*NW - Microgranitic dyke*	-6.73	308.51	9/15	356.2	42.2	8.9	78.1	6.1	58.7	301.8
37	PY59 A-F	*NW - Microgranitic dyke*	-6.77	308.56	13/14	339.6	13.8	12.83	70.3	5.1	65.4	252.4

39	PY61 A-E	*NW - Microgranitic dyke*	-6.8	308.63	5/10	347.1	34.1	6.94	G.C	10.7	61.5	282.3
41	PY63 K	*NW - Microgranitic dyke*	-6.76	308.56	2/2	331.3	35.2	1.99	647.2	9.8	51.4	262
MEAN POLE CD4					***11***	***352.7***	***33.3***	***10.47***	***19***	***10.7***		
								R=10.47	***K=18.7***	***A95=10.8***	***63.4***	***293.7***
											-63.4	***113.7***

Grand mean poles		Site mean directions						Paleomagnetic poles					
Name	***Polarity***	N	D_m (°)	I_m (°)	R	k	α95 (°)	Lat	Long	K	R	S	A95 (°)
CA1	Normal	10	315.6	-76.9	9.7	29.9	9	23.1	146.7	10.7	9.16	14.9/25	15.5
CA1	Reversed	16	131.2	75.4	15.54	32.4	6.6	-23.4	330	11.6	14.71	14.3/24	11.3
CA1	**Combined**	**26**	**132.8**	**76**	**25.23**	**32.7**	**5**	**-23.3**	**328.7**	**11.7**	**23.87**	**14.2/23.9**	**8.7**
CA2	Normal	6	67.1	-11.4	5.55	11.2	20.9	23	41.8	25.2	5.8	16.1	13.5
CA2	Reversed	12	236.9	12	10.98	10.7	13.9	-34	221	14.1	11.22	21.8	12
CA2	**Combined**	**18**	**240.3**	**11.8**	**16.5**	**11.1**	**10.8**	**-30.2**	**221.3**	**16.2**	**16.95**	**20.3**	**8.8**

Code	Name	A_{95}	Plat (°N)	Plong (°E)	Nominal Age (Ma)	Confidence	References
WEST AFRICA							
WA-01	IC1 Ivory Coast intrusions	16.1	-82	292	2100	strat.	1
WA-02	PL1 Obuasi greenstone	19	-50	36	2090	U-z	2
WA-03	PL2 Abouasi-Obuasi Dolerite intrusions	14	-53	102	2080	strat.	2
WA-04	IC2 Ferke batholith -Ivory coast	18.9	-25	83	2050	Pb-Pb APWP	1
WA-05	GAF Aftout granite	7.8	-6	90	1966	strat. U-z	2, 3, 4
WA-06	SL Aftout gabbro	5.7	28.8	55.1	1950	strat. Rb-Sr, U-z	3, 4
WA-07	AH Harper amphibolite	7	-10	73	1983	A-h	5
WA-08	OD Liberia Granulite	13	-17.5	89	1964	Rb-Sr	6
WA-09	Iguerda Inlier dikes	2.5	-4	262.1	1741	U-z	7
AMAZONIA							
AM-01	Mean GF1 (Approuague granite)	11.2	1.8	292.5	2089	U-z, i-BCT	8, 10
AM-02	OYA Oyapok tonalite and meta-ultrabasite	9.9	-28	346	2036	U-z	9
AM-03	ARMO, Armontabo River tonalite	10.1	-2.7	346.3	2030	i-BCT	10
AM-04	Mean CA1 (Imataca-Encrucijada)	16.5	-42.9	21.9	2000		11
AM-05	Mean GF2 Coastal late monzogranite	5.8	-58.5	30.2	1970		8
AM-06	Surumu volcanics	10.1	-27.4	54.8	1960	U-z, i-BCT	11
AM-07	**POLE CA1**	8.7	-23.3	328.7	1880	U-a, U-z, i-BCT	**This study**
AM-08	**POLE CA2**	8.8	-30.2	221.3	1860	U-a, U-z, BCT	**This study**
AM-09	ARO Guaniamo dikes (Comp II)	6	-42	0	1820	A-bi	12
AM-10	Avanavero sills	13	-48.4	27.9	1789	U-b, i-BCT	13